NASA Contractor Report 195477

High-Power Ion Thruster Technology

J.R. Beattie and J.N. Matossian
Hughes Research Laboratories
3011 Malibu Canyon Road
Malibu, California 90265

June 1996

Prepared for
Lewis Research Center
Under Contract NAS 3-25553

National Aeronautics and
Space Administration

CONTENTS

ILLUSTRATIONS

ILLUSTRATIONS (Continued)

ILLUSTRATIONS (Continued)

ILLUSTRATIONS (Continued)

TABLES

Section 1
SUMMARY

Work under this second phase of the contract emphasized performance-documentation and beam-diagnostic measurements of the NASA/Hughes common thruster S/N 2 at power levels ranging from 0.6 to 4.6 kW. The performance of this thruster had been evaluated at NASA - LeRC before it was shipped to Hughes. Subsequent testing at Hughes resulted in performance data that were in reasonable agreement with the NASA test results.

We demonstrated the feasibility of starting and operating the ring-cusp thruster without the use of a cathode-keeper electrode. In this new discharge-chamber arrangement, the discharge cathode is coupled directly to the anode, without the use of an intermediate keeper electrode. The cathode-ignition voltage was shown to be less than 90 V when operating in this mode, and the thruster could tolerate high-voltage recycles in which the discharge current was cut back to nearly zero.

We measured the tip temperature and internal pressure of the discharge cathode used in the NASA/Hughes common thruster as a function of cathode-emission current and discharge voltage. Cathode performance was observed to be highly repeatable, and tip temperatures were $\leq$1150°C for emission currents $\leq$30 A.

We demonstrated laser-induced fluorescence as a potential diagnostic for assessing the rate of mass loss from an accelerator grid due to ion sputtering. We demonstrated the feasibility of obtaining relative wear rates of the accel grid of an operating thruster, and our investigation suggests that absolute wear rates could be obtained by calibrating the LIF signal with measured wear rates.

Using argon, krypton, and xenon as the sputtering ions, we demonstrated that laminar thin film (LTF) erosion badges yield erosion rates that are consistent with similar results obtained using a direct-measurement technique such as surface profilometry. The NASA/Hughes common thruster S/N 2 was operated at the same conditions as the NASA 900-h lifetest with LTF badges placed on the accel grid. Results obtained from the LTF tests were in fair agreement with those obtained from the lifetest.

Using the improved pumping speed of the Hughes vacuum chamber, we investigated the effects of background pressure on measured accelerator current. Results obtained at low background pressures suggest that the ratio of accel current to beam current can approach 0.2 to 0.3% with xenon thrusters, consistent with earlier results obtained for mercury propellant.

Section 2
NASA/HUGHES COMMON THRUSTER

2.1 THRUSTER DESCRIPTION

Figure 1 is a sketch showing the prominent features of the discharge chamber in the NASA/Hughes common thruster. We refer to this device as the "common" thruster because identical units were fabricated at LeRC for performance evaluations both at NASA and Hughes. The discharge chamber uses a ring-cusp magnet configuration, with three rings of Sm_2Co_{17} magnets positioned along the cylindrical sidewall and circular endwall as indicated. Note that the common thruster does not employ a keeper electrode for the discharge cathode; the discharge is struck directly between the cathode and anode. (Work that led to this "keeperless" design is described in Section 3.1.) Figure 2 shows the scalar magnetic field measured in the discharge chamber of the common thruster S/N 2. The magnetic-field distribution is similar to those which have been documented for other 25- and 30-cm-diam ring-cusp thrusters, showing that "closure" of the 50-Gauss contour line[1] has been achieved.

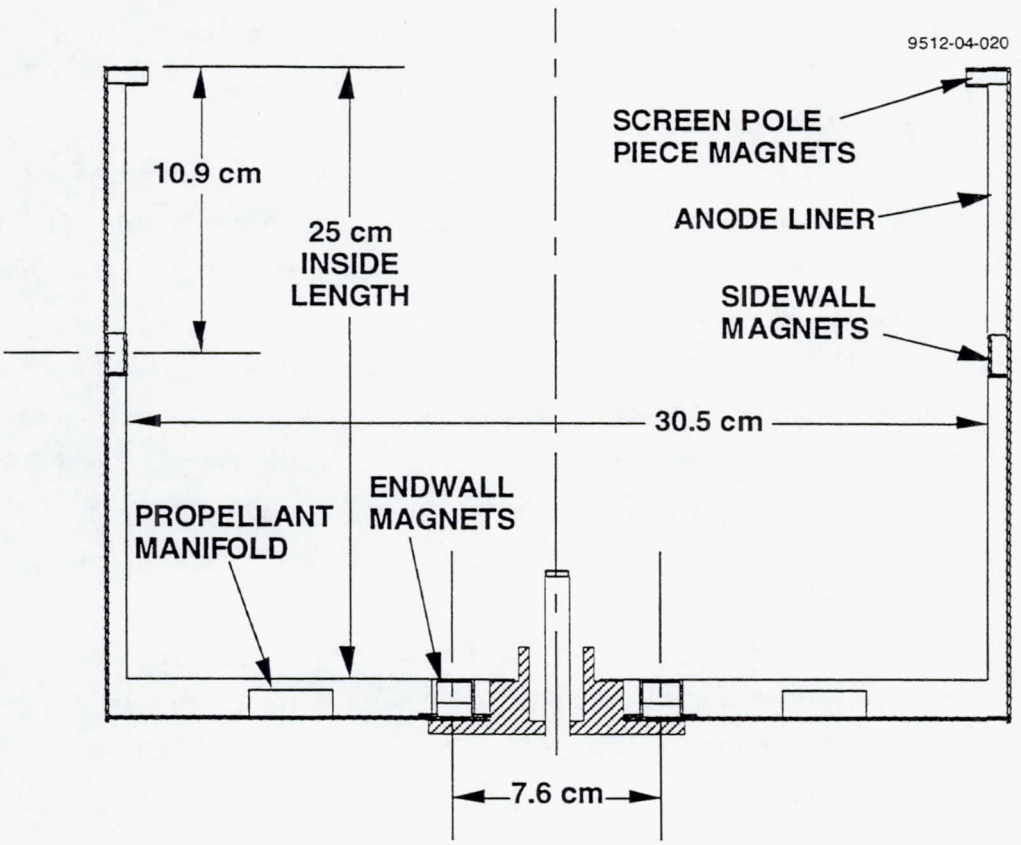

Figure 1. NASA/Hughes common thruster schematic.

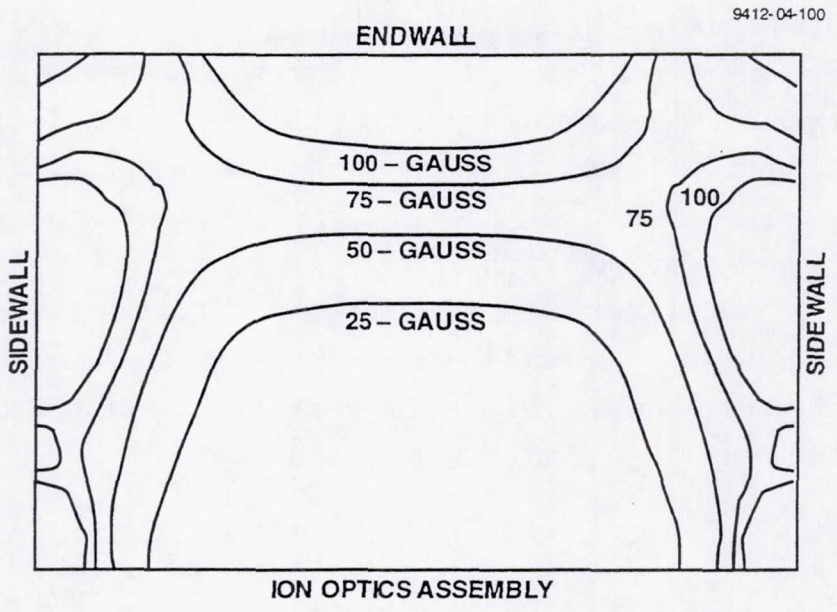

Figure 2. Scalar-magnetic-field contours obtained in NASA/Hughes common thruster S/N 2.

The NASA/Hughes common thruster employs a 1.52-mm orifice in the discharge cathode and a 0.51-mm orifice in the neutralizer cathode. In the testing conducted under this program, the thruster was equipped with ion-optics assembly S/N 907. Geometrical parameters for these optics are listed in Table 1. The nominal grid spacing for testing reported herein was 0.58 mm (23 mil).

Table 1. Summary of S/N 907 Grid Parameters.

Parameter	Screen Grid	Accel Grid
Aperture Diameter, mm	1.91	1.14
Thickness, mm	0.38	0.38
Hole Spacing, mm	2.21	2.21
Open Area, %	67	24
Aperture Geometry	Round	Round

2.2 FACILITY DESCRIPTION

The performance characterizations performed under this program were conducted using two vacuum test facilities. In the sections below, we describe these test facilities and their supporting diagnostic equipment. We also present an electrical schematic of the power-supply and instrumentation arrangement used for thruster-performance documentation.

2.2.1 Vacuum Chambers

Figure 3 shows a schematic diagram of the 3-m-diam vacuum chamber used to evaluate the performance of the 25- and 30-cm-diam thrusters described in Section 2. This chamber employs 0.9- and 1.2-m-diam LN_2-shrouded cryopumps, in combination with a 1-m-diam cryobaffled diffusion pump and LN_2 cryowall, to obtain an ultimate pressure of approximately $5x10^{-6}$ Pa ($4x10^{-8}$ Torr). The pumping speed of this chamber is approximately 47,000 l/s for xenon. The chamber is equipped with a water-cooled collector capable of absorbing well over 10 kW of ion-beam power. Graphite tiles are mounted on the collector to minimize the amount of material that is backsputtered onto the thruster under test. The pressure in the vacuum chamber is measured using an unbaffled ionization gauge mounted above the thruster.

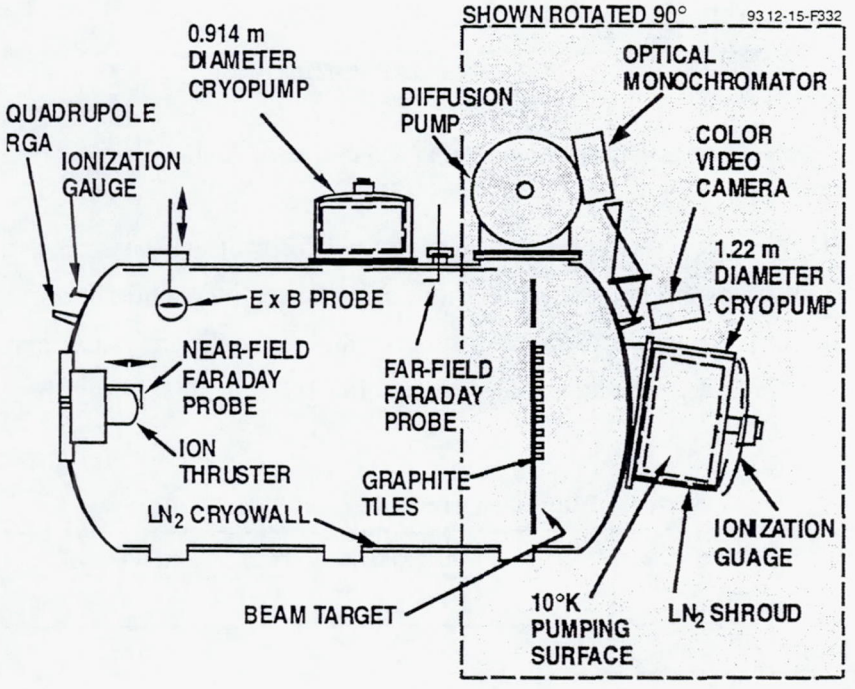

Figure 3. Schematic diagram of 3-m-diam cryopumped vacuum chamber.

The 3-m-diam vacuum chamber is equipped with a variety of diagnostic equipment. A quadrupole residual gas analyzer is used to measure the partial pressures of gases up to a mass number of 200. This analyzer is typically installed in a location (along with the ionization gauge) that enables it to sample essentially the same flux of vacuum-chamber gases arriving at the thruster. A test setup for optical-emission spectroscopy is located at the downstream end of the vacuum chamber and consists of a monochromator equipped with a photomultiplier tube for measuring the line intensities of excited atoms produced in the thruster. A color video camera located near the monochromator can be used to view operation of the thruster, as well as other

components in the vacuum chamber located within its field of view. An articulating **ExB** probe can be swept through the ion beam for determining the angular distribution of singly and doubly charged ions emanating from the thruster under test.

Other diagnostic equipment includes two Faraday probes used for measuring the ion-beam current density, as well as the charge-exchange-ion current density. The near-field Faraday probe can be used to measure the current-density profile at the exit plane of a thruster, as well as at axial locations of up to 50 cm downstream of the exit plane. The far-field Faraday probe is a gridded probe that can be traversed through the ion beam near the axial location of the beam collector. At this location (approximately 8 beam diameters downstream of the exit plane), the thruster appears as a point source of emitted ions. A computerized data-acquisition system, shown in Figure 4, is used for obtaining Langmuir-probe measurements of the plasma properties inside the thruster discharge chamber, as well as within the vacuum chamber itself.

Figure 5 shows a schematic diagram of the 0.6-m-diam vacuum chamber used to conduct component-performance evaluations, such as cathode and discharge-chamber temperatures. This vacuum chamber is cryopumped and has an LN_2-cooled cryowall; its pumping speed is about 2,000 l/s for xenon. The chamber is equipped with a quadrupole residual gas analyzer, and it has a quartz window for viewing discharge-chamber components with a radiation pyrometer.

2.2.2 Thruster Test Console

Figure 6 shows an electrical schematic of the test console used for the performance evaluation of the 25- and 30-cm-diam thrusters. Table 2 provides definitions of the various current and voltage symbols used in Figure 6. Table 2 also provides definitions of thruster-performance variables, including input power, thrust, specific impulse, and thruster efficiency.

2.3 PERFORMANCE EVALUATION

Performance evaluation of the NASA/Hughes common thruster S/N 2 was conducted using the standardized procedure developed under this contract and reported in the final report[2] for Phase 1. This procedure consists of operating the thruster for two hours at high discharge power and then measuring the variation of propellant-utilization efficiency with beam-ion-production cost as the latter is reduced to its minimum value. For each operating point, the cathode and main flow rates are adjusted to maintain the discharge voltage and beam current at their desired values.

Figure 7 shows the performance of the NASA/Hughes common thruster S/N 2 operated at a discharge voltage of $V_D = 28$ V and beam currents of $J_b = 1.45$ A and 3.22 A. These discharge-voltage and beam-current values were used to provide a comparison with the 30-cm-diam lab-model thruster that was evaluated under Phase 1 of this contract. At $J_b = 1.45$ A, the minimum

Figure 4. Computerized data-acquisition system used for performing Langmuir-probe measurements.

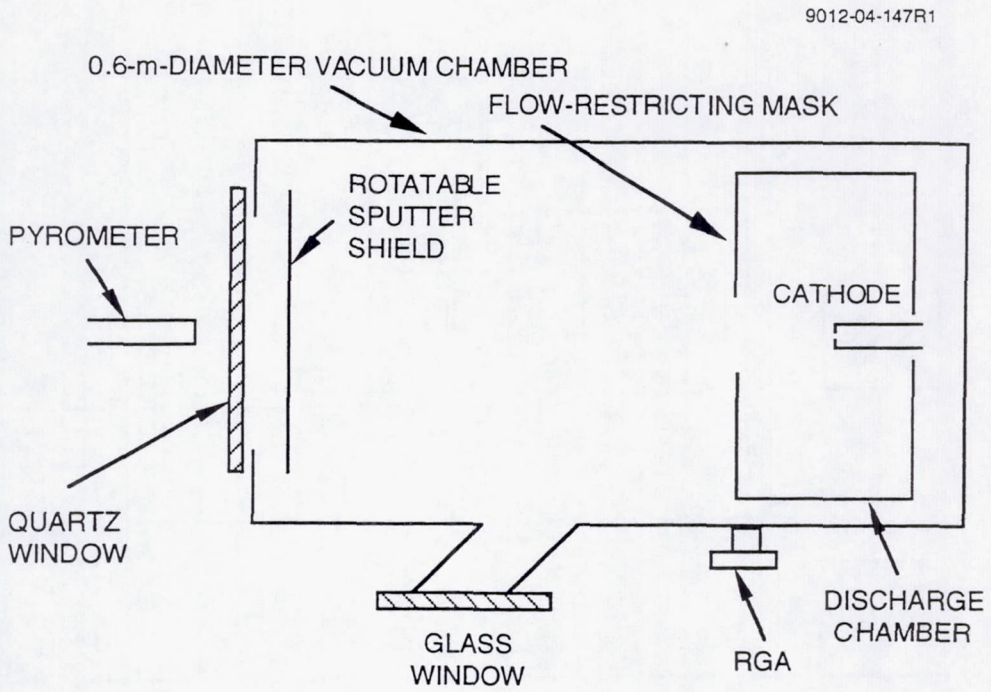

Figure 5. Schematic diagram of 0.6-m-diam cryopumped vacuum chamber.

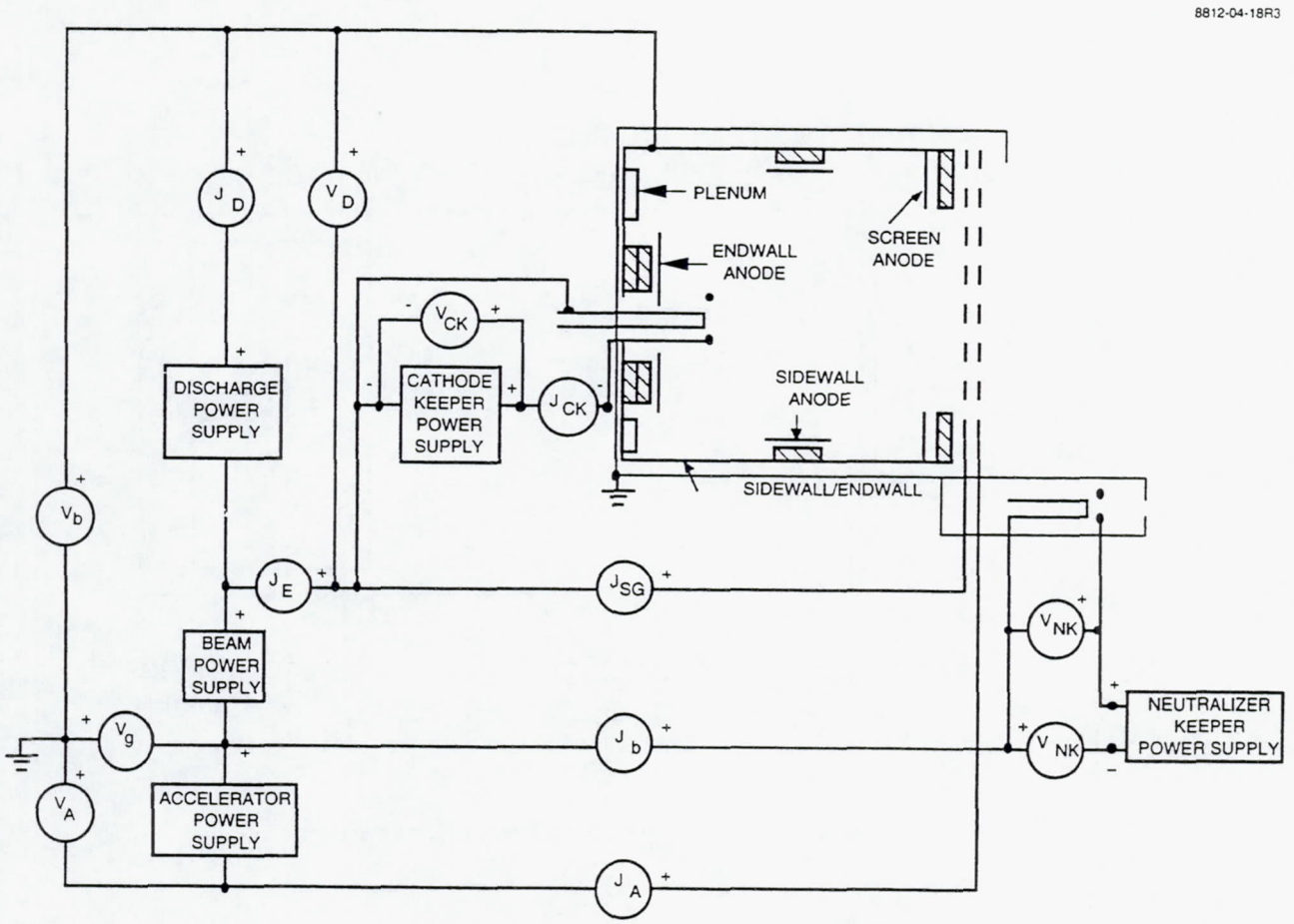

Figure 6. Electrical schematic of thruster test console.

Table 2. Definition of Thruster Performance Variables.

$F = 1.65\gamma J_b\sqrt{V_b}$	Thrust, mN	F_t	Thrust-Loss Correction Factor for Off-axis Vectoring
$I_{SP} = (123.71)\gamma(\eta_m)_{UNC}\sqrt{V_b}$	Specific Impulse, s	α	Thrust-Loss Correction Factor for Doubly Charged Ions
J_A	Accelerator Current, A	$P_{MISC} = J_{CK}V_{CK} + J_{NK}V_{NK} + J_AV_A + J_AV_b$	Misc Power, W
J_b	Beam Current, A	$P_D = J_EV_D$	Discharge Power, W
J_{NK}	Neutralizer Keeper Current, A		
$\dot{m}_c$	Equivalent Cathode Flow Rate, A	J_{CK}	Cathode Keeper Current, A
$\dot{m}_f$	Equivalent Gas-Ingestion Flow Rate (Appendix B), A	$(\eta_{md})_{UNC} = \frac{J_b}{\dot{m}_{md}}$	Discharge Propellant-Utilization Efficiency, % (Uncorrected for Doubly Charged Ions)
$\dot{m}_m$	Equivalent Main Plenum Flow Rate, A	$\eta_e = \frac{P_b}{P_{TOT}}$	Thruster Electrical Efficiency, %
$\dot{m}_{md} = \dot{m}_c + \dot{m}_m + \dot{m}_f$	Discharge-Chamber Propellant Flow Rate, A	$\gamma = F_t\alpha$	Total Thrust-Loss Correction Factor
$\dot{m}_n$	Equivalent Neutralizer Flow Rate, A	$\varepsilon_i = J_EV_D / J_b$	Beam-ion Production Cost, W/A or eV/Ion
$\dot{m}_T = \dot{m}_n + \dot{m}_{md}$	Equivalent Thruster Propellant Flow Rate, A	$P_{TOT} = P_b + P_D + V_gJ_b + P_{MISC}$	Total Thruster Power, W
V_A	Accelerator Voltage, V	V_gJ_b	Neutralizer Coupling Power, W
V_b	Beam Voltage, V	$P_b = J_bV_b$	Beam Power, W
V_{CK}	Cathode Keeper Voltage, V	P	Vacuum Chamber Pressure, Pa
V_D	Discharge Voltage, V	J_E	Cathode-Emission Current, A
V_g	Neutralizer Coupling Voltage, V	β	Discharge Propellant-Utilization Efficiency Correction Factor for Doubly Charged Ions
V_{NK}	Neutralizer Keeper Voltage, V	$\eta_t = \gamma^2\eta_e(\eta_m)_{UNC}$	Total Thruster Efficiency, %
$V_{TOT} = V_b + \lvert V_A\rvert$	Total Accelerating Voltage, V	$\eta_{mt} = \beta J_b / \dot{m}_T$	Total Propellant-Utilization Efficiency, % (Corrected for Doubly Charged Ions)
$\Delta\dot{m}_f$	Change in Gas-ingestion Due to Addition of Xenon to the Vacuum Facility, A	$\Delta(\dot{m}_m + \dot{m}_c)$	Change in Sum of Main Plenum and Cathode Flow Rates, A
$(\eta_m)_{UNC} = \frac{J_b}{\dot{m}_T}$	Total Thruster Propellant-Utilization Efficiency, % (Uncorrected for Doubly Charged Ions)	$\eta_{md} = \beta J_b / \dot{m}_{md}$	Discharge Propellant-Utilization, Efficiency, % (Corrected for Doubly Charged Ions)

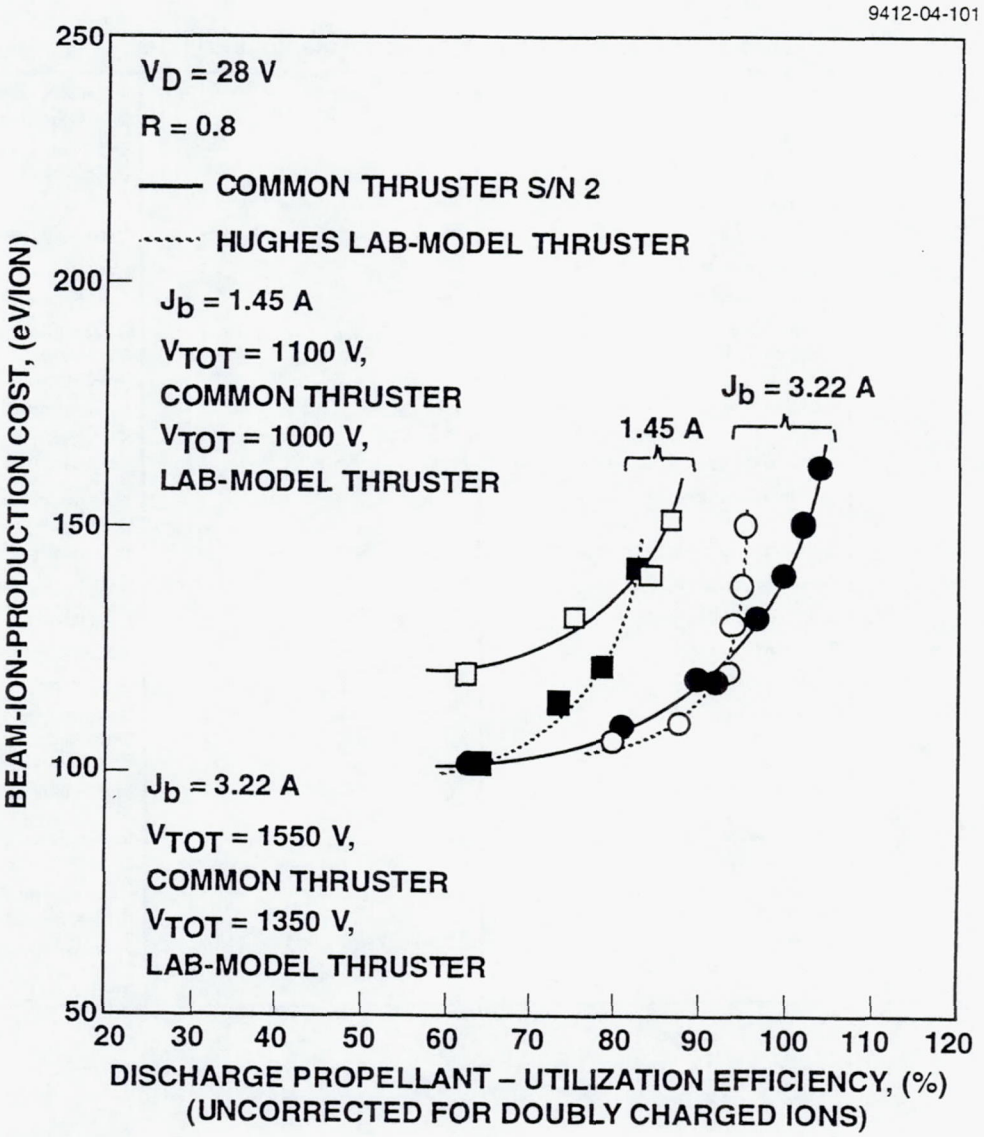

Figure 7. Discharge-chamber performance curve documented for NASA/Hughes common thruster S/N 2 and the Hughes lab-model thruster. (Data corrected for gas ingestion.)

beam-ion-production cost of the NASA/Hughes common thruster is ε_i = 120 eV/ion and the maximum propellant-utilization efficiency (uncorrected for doubly charged ions) is $(\eta_{md})_{unc}$ = 87%. At J_b = 3.22 A, the minimum beam-ion-production cost of this thruster is ε_i = 100 eV/ion and the maximum propellant-utilization efficiency is $(\eta_{md})_{unc}$ =103%. Figure 7 presents similar performance data obtained under Phase I using the Hughes lab-model thruster.

Figure 8 shows the beam profile of thruster S/N 2 measured at the "knee" of the performance curve (ε_i = 150 eV/ion) for a beam current of J_b = 1.45 A. The computed beam-flatness parameter is F = 0.45, which is approximately equal to that which was measured for the 30-cm-diam lab-model thruster under Phase 1 of this contract.

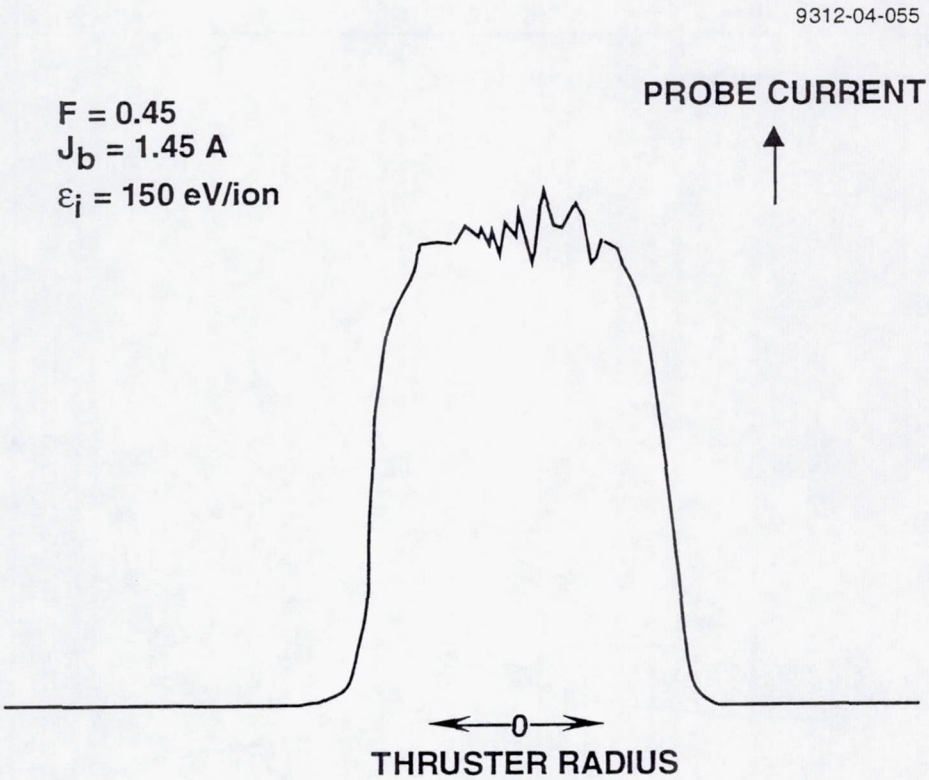

Figure 8. Beam-current-density profile measured in NASA/Hughes common thruster S/N 2.

Figure 9 presents performance data obtained in the HRL test facility for the NASA/Hughes common thruster S/N 2 operated at the conditions specified by NASA - LeRC. Figure 10 and Tables 3(a) and 3(b) compare the performance data presented in Figure 9 with similar results that were obtained with this same thruster in the NASA - LeRC test facility. There is excellent agreement in the baseline beam-ion-production cost for all beam currents. However, there is a noticeable increase in the maximum propellant-utilization efficiency for the performance measurements obtained at Hughes (at least for the higher beam currents). On the basis of the flow-meter calibration results presented in Appendix A, we cannot attribute the observed differences in maximum propellant utilization to any systematic error in the measured flow rates. Repeatability of the performance data obtained at Hughes is shown in Figure 11, and Figure 12 shows corresponding repeatability results obtained by NASA. The repeatability of thruster performance data is within about ±3% in both the Hughes and NASA test facilities.

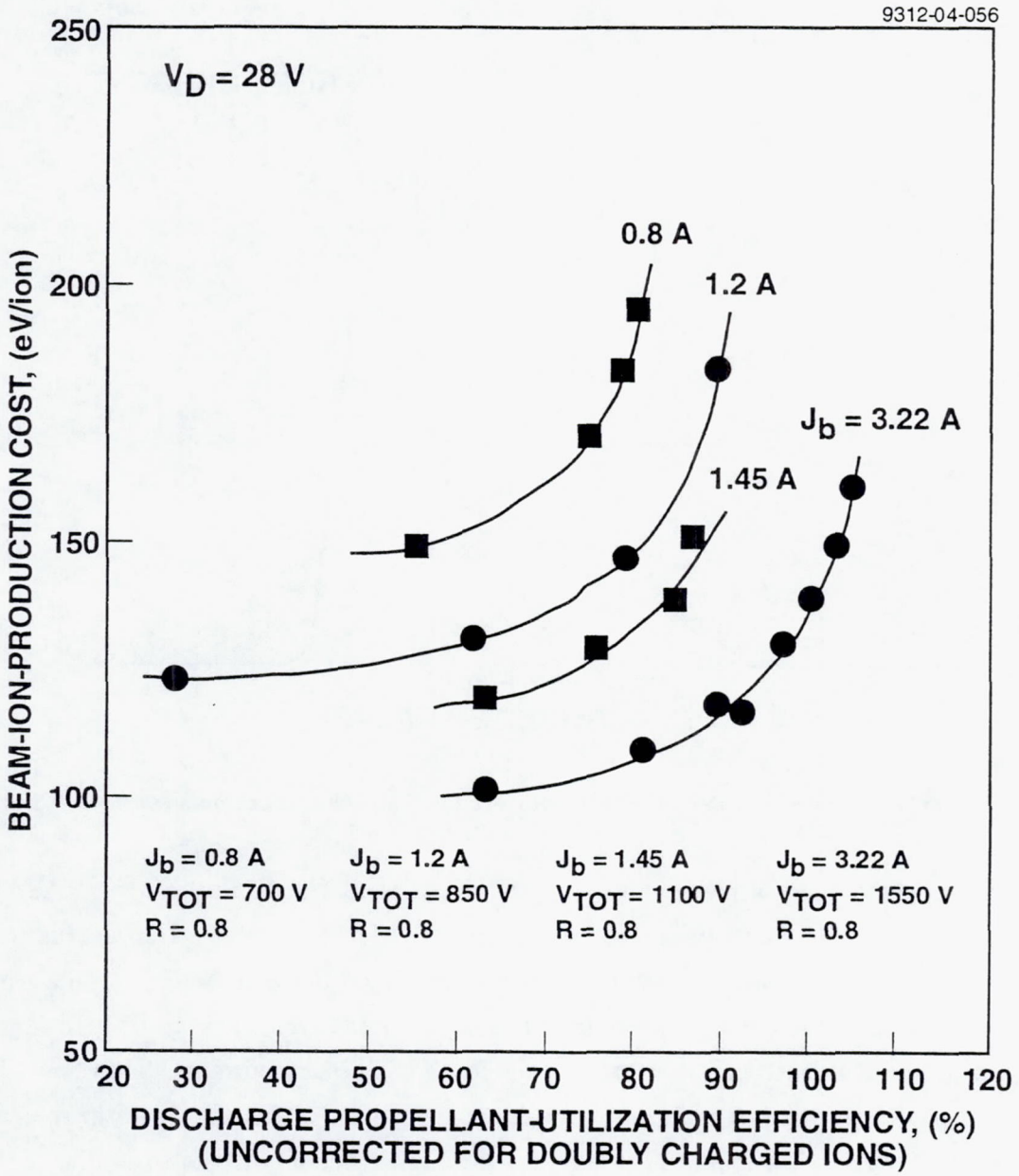

Figure 9. Performance data for the NASA/Hughes common thruster S/N 2 operated at Hughes.

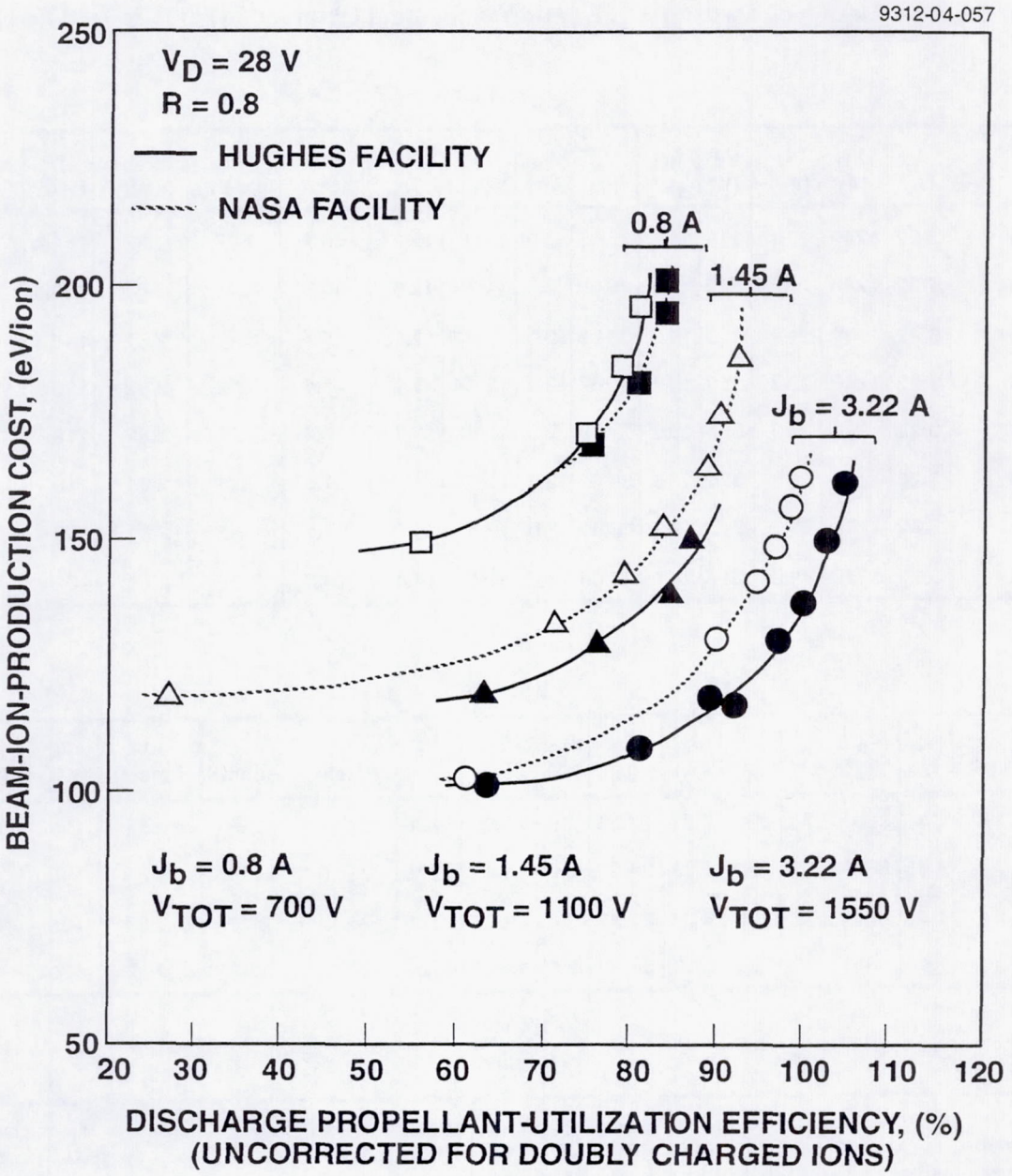

Figure 10. Comparison of performance data obtained at LeRC and Hughes for common thruster S/N 2.

Table 3(a). Listing of Thruster S/N 2 Performance Data Obtained in Hughes Test Facility.

9612-15-016

J_b = 3.22 A

P X 10^{-5} TORR	J_b (A)	V_b (V)	J_A (mA)	V_A (V)	J_D (A)	V_D (V)	J_{NK} (A)	V_{NK} (V)	V_g (V)	$\dot{m}_m$ (sccm)	$\dot{m}_C$ (sccm)	$\dot{m}_n$ (sccm)	ε_i (W/A)	$(\eta_{mD})_{UNC}$ (%)
1.6	3.22	1240	20.3	310	18.6	28.00	2.0	12.0	12.23	43.1	2.75	2.82	161.4	104.8
1.6	3.22	1240	20.94	310	17.3	28.00	2.0	11.75	12.05	44.3	2.42	2.81	150.1	102.4
1.6	3.22	1240	21.94	310	16.0	28.08	2.0	12.43	12.58	45.7	2.14	2.82	140	100
1.6	3.22	1240	23.2	310	15.0	28.07	2.0	12.44	12.97	47.4	1.98	2.82	130	96.9
1.7	3.22	1240	25.3	310	13.5	28.08	2.0	12.8	13.53	50.4	1.70	2.82	118	91.98
1.8	3.22	1240	26.9	310	13.6	28.05	2.0	12.74	14.18	51.6	1.71	2.81	118	9.8
1.9	3.22	1240	31.1	310	12.5	28.03	2.0	12.51	13.40	57.6	1.45	2.81	109	81.1
2.4	3.22	1240	46.2	310	11.7	28.04	2.0	12.5	14.4	74.6	1.18	2.81	102	63.2

9612-15-015

J_b = 1.45 A

P X 10^{-5} TORR	J_b (A)	V_b (V)	J_A (mA)	V_A (V)	J_D (A)	V_D (V)	J_{NK} (A)	V_{NK} (V)	V_g (V)	$\dot{m}_m$ (sccm	$\dot{m}_C$ (sccm)	$\dot{m}_n$ (sccm)	ε_i W/A)	$(\eta_{mD})_{UNC}$ (%)
0.99	1.45	880	8.75	220	7.83	27.96	2.0	14.56	14.46	22.1	2.69	2.81	151	86.84
1.0	1.45	880	8.80	220	7.23	28.00	2.0	14.4	11.76	23.16	2.33	2.81	140	84.46
1.1	1.45	880	9.76	220	6.24	27.95	2.0	12.47	12.69	26.4	2.13	2.81	130	75.47
1.2	1.45	880	12.9	220	6.19	28.03	2.0	13.84	18.8	32.5	1.68	2.81	120	63.0

9612-15-014

J_b = 0.8 A

P X 10^{-5} TORR	J_b (A)	V_b (V)	J_A (mA)	V_A (V)	J_D (A)	V_D (V)	J_{NK} (A)	V_{NK} (V)	V_g (V)	$\dot{m}_m$ (sccm)	$\dot{m}_C$ (sccm)	$\dot{m}_n$ (sccm)	ε_i (W/A)	$(\eta_{mD})_{UNC}$ (%)
1.1	0.8	560	5.39	140	5.60	28.04	2.0	15.46	14.47	9.7	5.0	2.81	196.2	80.34
0.7	0.8	560	4.58	140	5.26	28.00	2.0	15.53	14.6	10.7	4.4	2.81	184.1	78.57
0.7	0.8	560	4.70	140	4.89	28.05	2.0	15.46	14.4	12.7	3.26	2.81	171.4	74.4
0.8	0.8	560	6.43	140	4.26	28.07	2.0	15.65	14.17	19.9	1.65	2.81	149.5	55.14

Table 3(b). Listing of Thruster S/N 2 Performance Data Obtained in LeRC Test Facility.

9612-15-016R1

J_b = 3.22 A

P X 10^{-5} TORR	J_b (A)	V_b (V)	J_A (mA)	V_A (V)	J_D (A)	V_D (V)	J_{NK} (A)	V_{NK} (V)	V_g (V)	$\dot{m}_m$ (sccm)	$\dot{m}_C$ (sccm)	$\dot{m}_n$ (sccm)	ε_i (W/A)	$(\eta_{mD})_{UNC}$ (%)
0.87	3.22	1255	14.0	299	21.8	28	1	12.8	18.3	43.1	4.62	3.34	162	99.2
0.8	3.22	1254	14.0	304	21.2	28	2	13.4	19	45.13	4.06	1.02	156	97.3
0.82	3.22	1259	14.0	303	20.4	28.1	2	13.5	19	46.01	3.57	1.02	150	96.53
0.84	3.22	1260	14.5	304	19.4	28	2	13.2	18.8	47.53	3.10	1.02	141	94.2
0.87	3.22	1263	16.0	303	18.2	28	2	13.0	18.8	50.5	2.58	1.02	130	90.9
1.3	3.20	1259	36.0	301	15.0	28	1	12.0	18.2	77.06	1.07	3.33	103	60.9

9612-15-015R1

J_b = 1.45 A

P X 10^{-5} TORR	J_b (A)	V_b (V)	J_A (mA)	V_A (V)	J_D (A)	V_D (V)	J_{NK} (A)	V_{NK} (V)	V_g (V)	$\dot{m}_m$ (sccm	$\dot{m}_C$ (sccm)	$\dot{m}_n$ (sccm)	ε_i W/A)	$(\eta_{mD})_{UNC}$ (%)
0.48	1.44	893	4.5	217	11	27.9	1	14.0	18.0	20.39	2.97	3.36	185	91.4
0.48	1.45	889	4.5	217	10.5	28.0	1	14.0	18.0	21.53	2.41	3.36	175	89.9
0.5	1.45	892	5.0	218	10.0	28.0	1	14.0	18.0	22.43	1.86	3.36	165	88.6
0.52	1.45	895	5.5	218	9.3	28.0	1	14.0	18.0	24.18	1.49	3.36	152	83.8
0.55	1.45	897	6.0	220	8.89	27.9	1	14.0	18.0	25.69	1.41	3.36	143	79.4
0.61	1.46	896	7.5	215	8.39	28.0	1	14.0	18.0	29.35	1.19	3.35	133	70.9
1.4	1.49	888	35.0	224	7.8	28.0	1	14.0	19.0	84.01	0.42	3.34	119	26.2

9612-15-014R1

J_b = 0.8 A

P X 10^{-5} TORR	J_b (A)	V_b (V)	J_A (mA)	V_A (V)	J_D (A)	V_D (V)	J_{NK} (A)	V_{NK} (V)	V_g (V)	$\dot{m}_m$ (sccm)	$\dot{m}_C$ (sccm)	$\dot{m}_n$ (sccm)	ε_i (W/A)	$(\eta_{mD})_{UNC}$ (%)
0.36	0.8	549	4.0	146	6.6	27.9	1	14.5	20.8	11.93	2.23	1.0	202	83.6
0.36	0.8	546	4.0	147	6.4	28.0	1	19.2	27.0	12.31	1.92	1.02	196	83.2
0.38	0.8	539	4.0	148	6.0	28.0	1	21.0	28.7	13.2	1.60	1.01	182	80.0
0.39	0.79	549	4.5	151	5.6	28.0	1	13.8	21.0	14.46	1.30	1.01	170	74.2

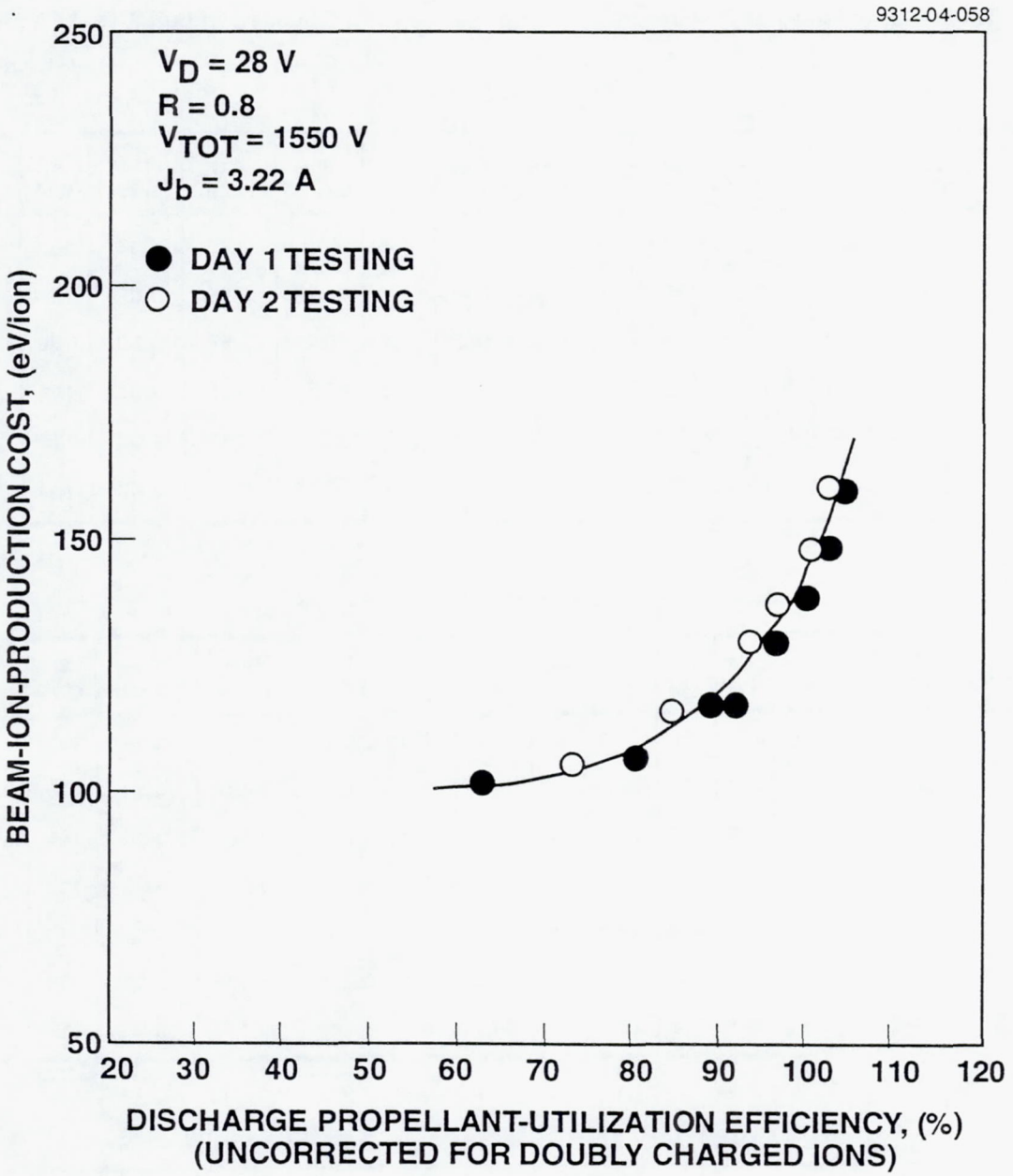

Figure 11. Typical repeatability of performance data for the NASA/Hughes common thruster S/N 2 operated at Hughes.

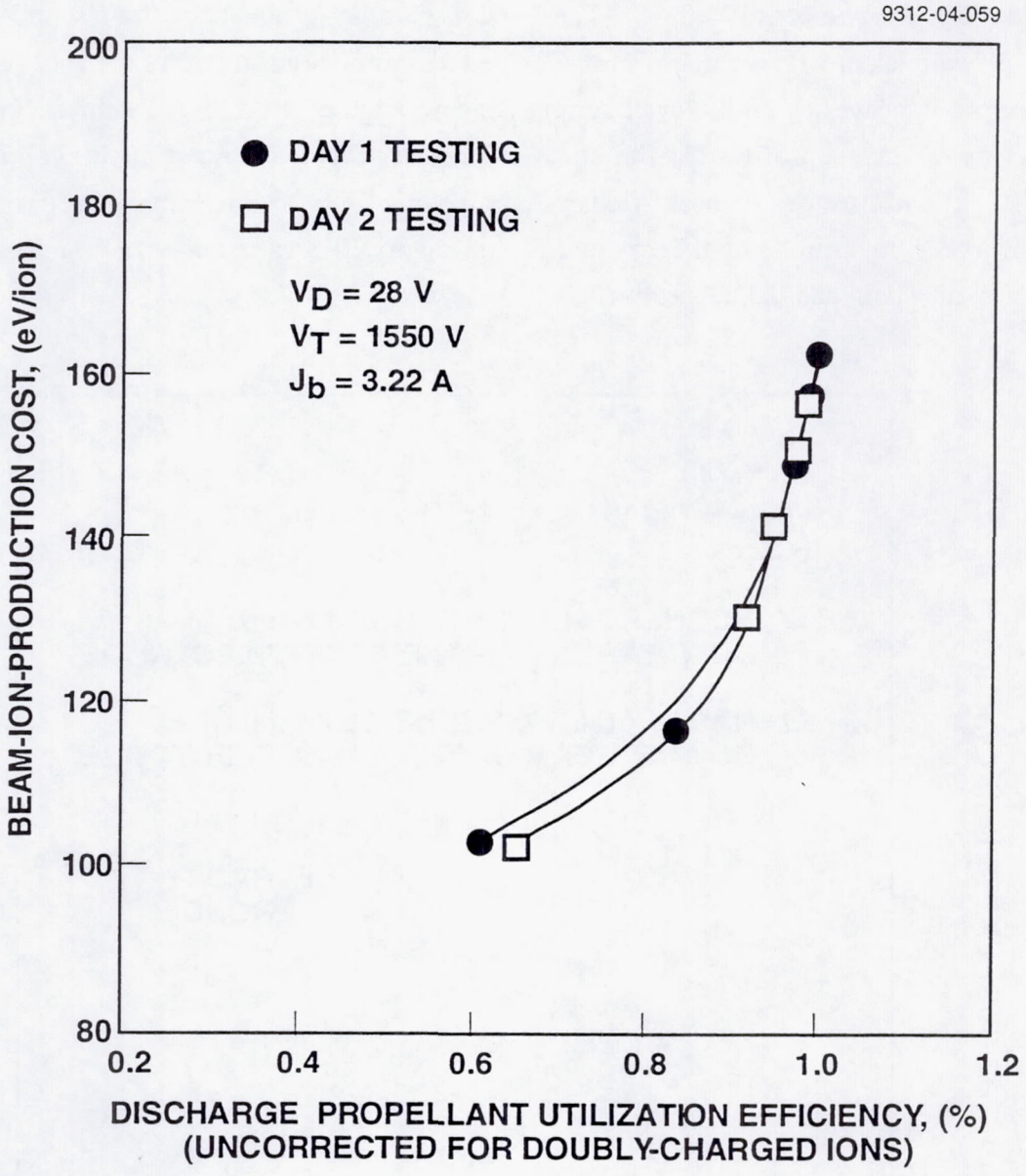

Figure 12. Typical repeatability of performance data for the NASA/Hughes common thruster S/N 2 operated at LeRC.

2.4 BEAM DIAGNOSTICS

Figure 13 compares the beam-current-density profiles measured in the NASA and Hughes test facilities for the common thruster S/N 2 operated at a beam current of J_b = 0.8 A. The Hughes measurements were obtained using a movable Faraday probe located downstream of the accel (negative) electrode. The probe data were recorded on an x-y plotter and then digitized using a tablet digitizer. The integrated beam current is shown to have a value of 0.74 A, which is within 7.5% of the measured value of the beam current (J_b = 0.8 A). The beam-flatness

parameter has a value of F = 0.44. The NASA Faraday-probe data (half-scan shown in Figure 13) were taken with a Faraday probe located 25.4 mm downstream of the accel electrode. and therefore indicates a slightly lower current density. Figure 14 presents a similar comparison of the current-density profiles for the common thruster S/N 2 operated at the conditions of NASA's 5-kW life test.[3] The beam-flatness parameter of F = 0.41 is somewhat less than that which has been measured for the 25- and 30-cm-diam XIPS thrusters at a beam current of J_b = 3.22 A (F = 0.54 and 0.5, respectively).

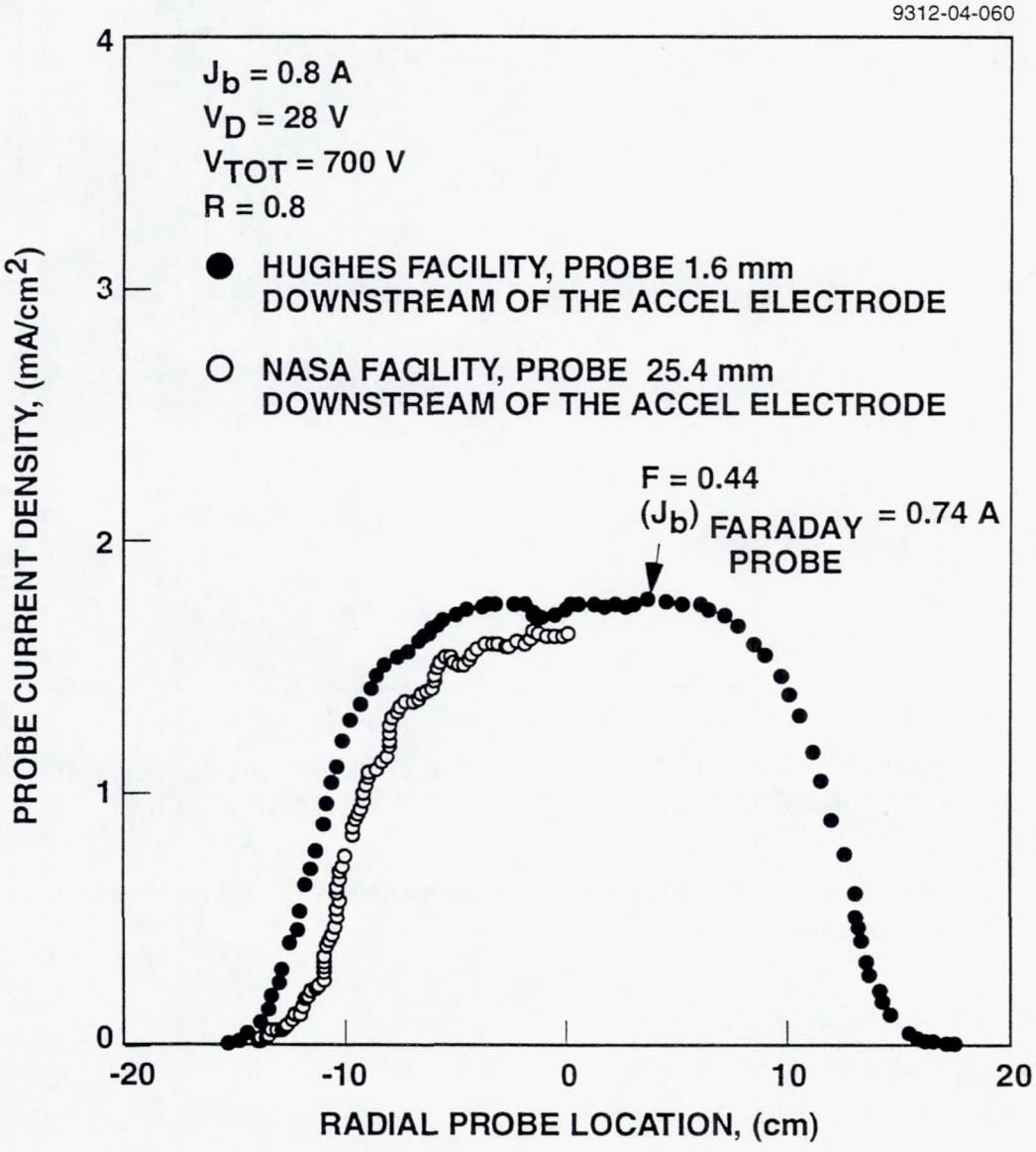

Figure 13. Comparison of beam-current-density profiles obtained at LeRC and Hughes for common thruster S/N 2 operated at a power level of 600 W.

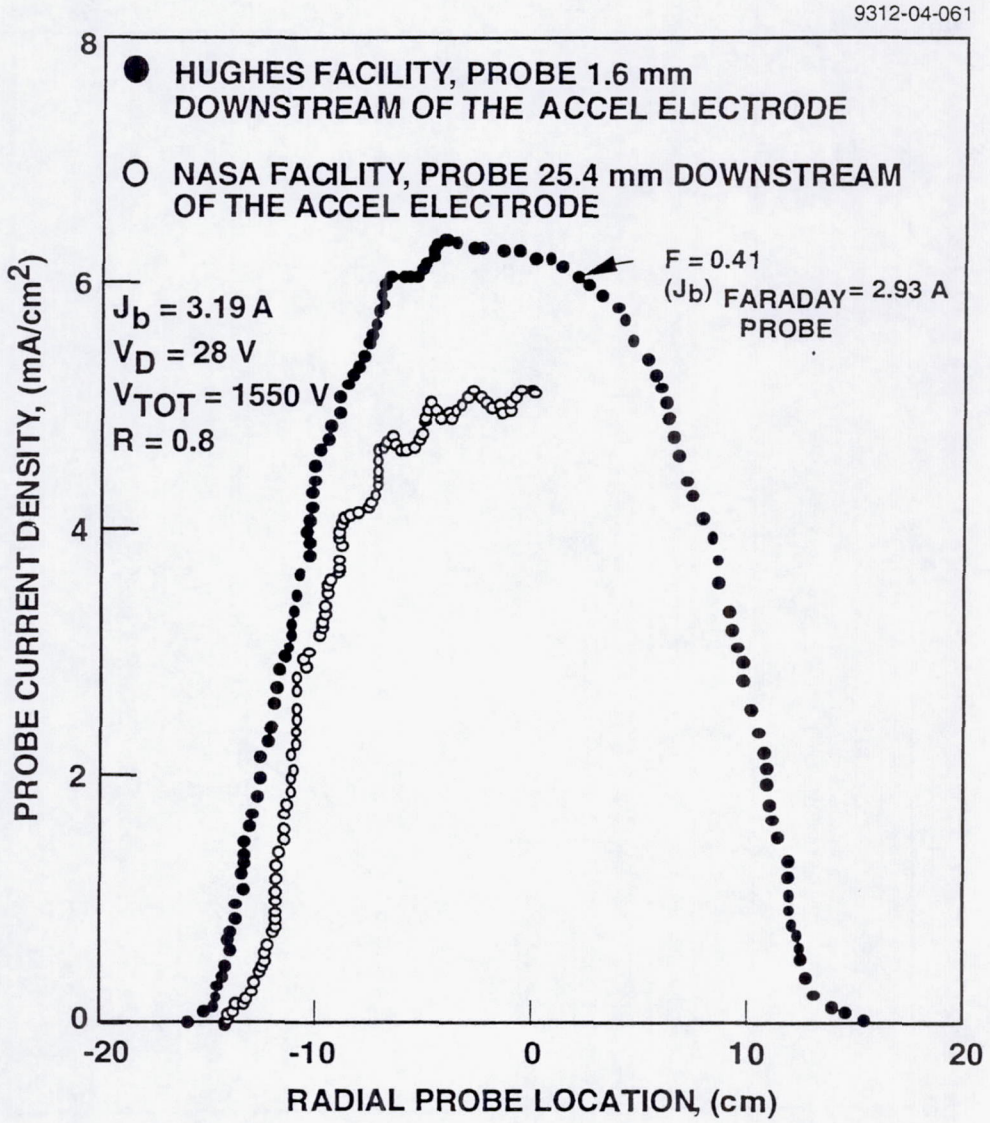

Figure 14. Comparison of beam-current-density profiles obtained at LeRC and Hughes for common thruster S/N 2 operated at a power level of 4.6 kW.

The doubly charged ion fraction of the NASA/Hughes common thruster S/N 2 was measured using an **ExB** probe. Measurements were obtained at an operating condition of $J_b = 3.22$ A, corresponding to the two operating points indicated as solid dots in Figure 15 (propellant-utilization efficiencies of $(\eta_{md})_{unc}$ = 104.1% and 92.6%, respectively). Tables 4 and 5 summarize the thrust-loss parameters obtained from the **ExB**-probe measurements at the two operating points. The doubly charged ion fraction measured at a propellant-utilization efficiency of $(\eta_{md})_{unc}$ = 104% is quite high, having an average value of $J^{++}/J^{+} = 0.27$. Reducing the propellant-utilization efficiency to $(\eta_{md})_{unc} = 92.6\%$ reduces the doubly charged ion fraction to a more-reasonable average value of $J^{++}/J^{+} = 0.15$.

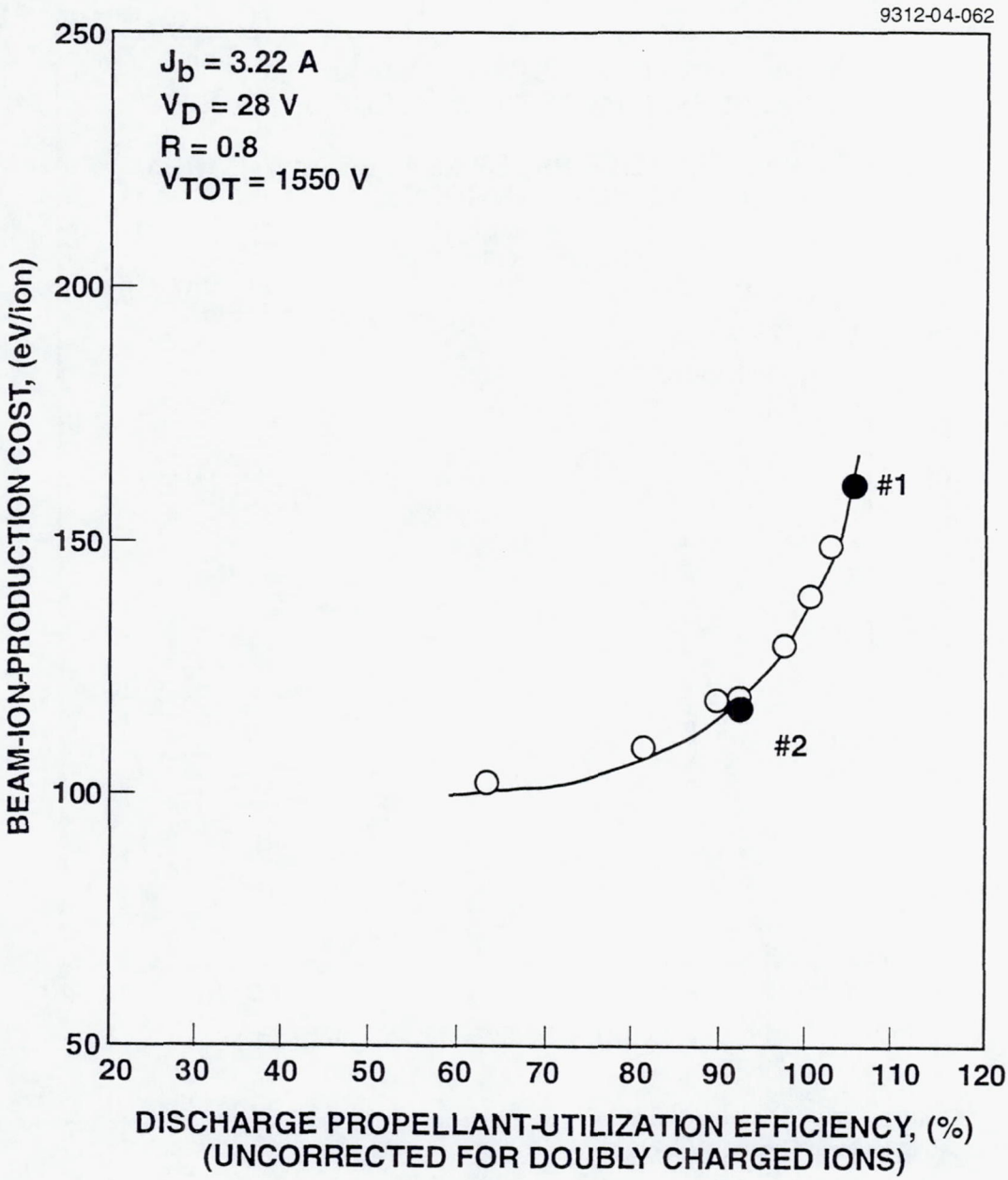

Figure 15. Performance conditions (solid symbols) under which ExB-probe data were obtained for common thruster S/N 2.

Table 4. Summary of ExB Probe Data (Point #1 in Figure 11)

Input Data								
φp	r = 0.75 R		r = 0.50 R		r = 0.25 R		r = 0.00 R	
(deg)	J^+(nA)	J^{++} (nA)	J^+ (nA)	J^{++}(nA)	J^+(nA)	J^{++}(nA)	J^+(nA)	J^{++}(nA)
–25.0	0.0034	0.0017	0.0029	0.0016	0.0020	0.0015	0.0017	0.0015
–20.0	0.0086	0.0030	0.0056	0.0022	0.0036	0.0021	0.0024	0.0017
–15.0	0.0310	0.0055	0.0124	0.0040	0.0065	0.0033	0.0036	0.0023
–10.0	0.0992	0.0115	0.0635	0.0158	0.0273	0.0085	0.0133	0.0043
–5.0	0.1172	0.0149	0.2138	0.0693	0.1124	0.0487	0.0646	0.0279
0.0	0.0485	0.0060	0.1698	0.0467	0.2123	0.1104	0.2019	0.1175
5.0	0.0124	0.0024	0.0428	0.0086	0.0942	0.0402	0.1423	0.0735
10.0	0.0036	0.0015	0.0071	0.0023	0.0252	0.0067	0.0403	0.0146
15.0	0.0020	0.0013	0.0034	0.0019	0.0038	0.0023	0.0115	0.0037

Summary of Thrust Parameters				
	r= 0.75 R	r = 0.50 R	r = 0.25 R	r = 0.00 R
j^+ (mA/cm^2)	7.19	9.6132	9.03	8.20
j^{++} (mA/cm^2)	1.60	2.2937	3.88	3.97
(j^{++}/j^+)	0.22	0.2386	0.42	0.48
φ (deg)	12.4	9.9401	9.85	9.63
α	F_t	$J^+ + J^{++}$	β	J^{++} / J^+
0.937	0.980	5.5	0.892	0.272

Table 5. Summary of ExB Probe Data (Point #2 in Figure 11)

Input Data								
φp	r = 0.75 R		r = 0.50 R		r = 0.25 R		r = 0.00 R	
(deg)	J^+(nA)	J^{++} (nA)	J^+ (nA)	J^{++}(nA)	J^+(nA)	J^{++}(nA)	J^+(nA)	J^{++}(nA)
–25.0000	0.0032	0.0014	0.0028	0.0014	0.0020	0.0013	0.0014	0.0013
–20.0000	0.0082	0.0019	0.0059	0.0018	0.0038	0.0017	0.0025	0.0015
–15.0000	0.0345	0.0044	0.0051	0.0030	0.0072	0.0023	0.0039	0.0018
–10.0000	0.1236	0.0083	0.0095	0.0034	0.0448	0.0074	0.0144	0.0030
–5.0000	0.1544	0.0099	0.2847	0.0443	0.2092	0.0461	0.0939	0.0223
0.0000	0.0614	0.0037	0.0194	0.0288	0.2757	0.0657	0.2730	0.0766
5.0000	0.0154	0.0018	0.0520	0.0055	0.1117	0.0234	0.1945	0.0558
10.0000	0.0039	0.0014	0.0062	0.0019	0.0242	0.0035	0.0426	0.0076

Summary of Thrust Parameters				
	r= 0.75 R	r = 0.50 R	r = 0.25 R	r = 0.00 R
j^+ (mA/cm^2)	8.1909	2.5715	10.5449	9.6943
j^{++} (mA/cm^2)	0.9204	0.6693	2.2960	2.8557
(j^{++}/j^+)	0.1124	0.2603	0.2177	0.2946
φ (deg)	11.3081	5.4447	8.4418	8.7411
α	F_t	$J^+ + J^{++}$	β	J^{++} / J^+
0.96148	0.98414	4.68528	0.93424	0.15143

Table 6 is a summary of the thruster performance parameters (thrust, specific impulse, efficiency, and total power) computed using the tabulated electrical parameters and the thrust-loss correction factors listed in Tables 4 and 5. Note that at the operating condition of J_b = 0.8 A we could not detect the presence of any doubly charged ions. (The detection value of our ExB probe is believed to be ≈1%.

Table 6. Performance Data for NASA/Hughes Common Thruster S/N 2

J_b (A)	V_D (V)	V_b (V)	V_A (V)	J^{++}/J^{+} (%)	ε_i (eV/ion)	P_b (kW)	P_{TOT} (kW)	η_e (%)	$(\eta_{md})_{unc}$ (%)	$(\eta_m)_{unc}$ (%)	γ	F (mN)
3.22	27.9	1240	-310	27.2	161.2	4.0	4.61	86.6	104.1	98.51	.919	172
3.22	27.96	1240	-310	15.1	116.8	4.0	4.48	89.13	92.6	88.0	.946	177
0.8	28.0	560	-140	0	196.0	0.448	0.651	68.8	80.3	67.6	.983*	30.7

*Uses thrust loss correction factor for beam divergence corresponding to J_b = 3.22 A.

Electrical Data for Common Thruster S/N 2

J_A (mA)	V_{NK} (V)	V_g (V)	J_{NK} (A)
21.5	10.87	12.0	2.0
27.2	11.0	13.0	2.0
5.23	15.36	13.95	2.0

Nomenclature:

- J_A = accel current
- J_b = beam current
- J_{NK} = neutralizer keeper current
- V_g = coupling voltage
- V_D = discharge voltage
- V_b = beam voltage
- V_A = accel voltage
- V_{NK} = neutralizer keeper voltage
- J^{++}/J^{+} = ratio of doubly to singly charged ion currents (uncorrected for doubly charged ions)
- $(\eta_{md})_{unc}$ = discharge propellant-utilization efficiency (uncorrected for doubly charged ions)
- $(\eta_m)_{unc}$ = total thruster propellant-utilizationefficiency (uncorrected for doubly charged ions)
- ε_i = beam-ion-production cost
- P_b = beam power
- P_{TOT} = total power
- η_e = electrical efficiency
- γ = thrust loss correction factor
- F = thrust
- I_{sp} = specific impulse

2.5 ION OPTICS PERFORMANCE

The perveance of ion-optics assembly S/N 907 used on the NASA/Hughes common thruster S/N 2 was obtained over a wide range of beam current, using the measurement procedure described in the final report[2] for Phase 1. The beam voltage was swept over a range of about 600 V, and both the beam voltage and accel current were recorded on an x-y plotter. Figure 16

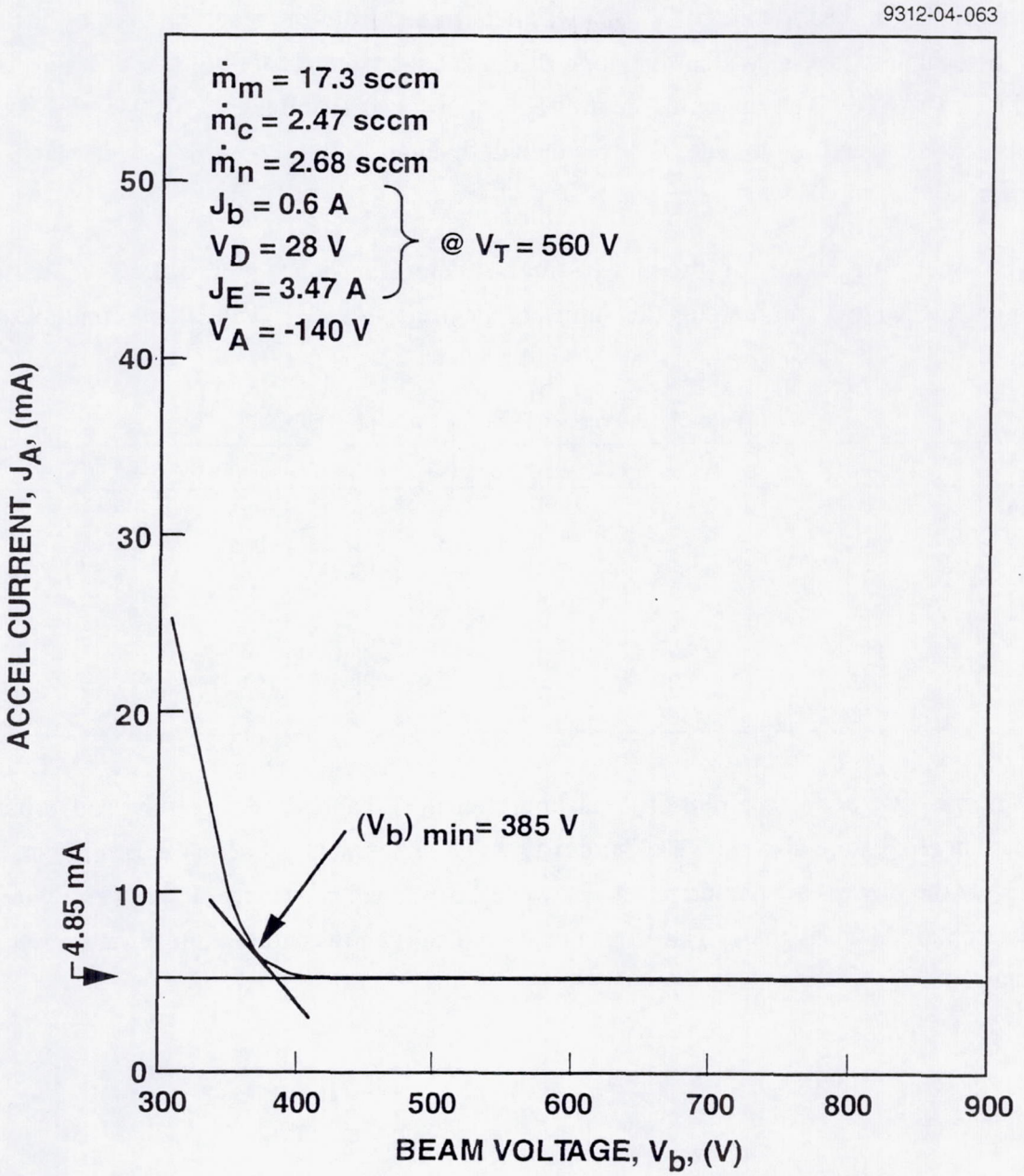

Figure 16. Accel-current/beam-voltage characteristic for ion optics S/N 907 operated on the NASA/Hughes common thruster S/N 2.

shows the resulting variation of accel current with beam voltage for the common thruster S/N 2 operated at a beam current of J_b = 0.6 A. The initial setpoints for the beam current, discharge voltage, cathode-emission current, and accel voltage are shown in the figure.

The minimum beam voltage $(V_b)_{min}$ was determined from the recorder trace by locating the value of beam voltage at which the slope of the accel-current/beam-voltage characteristic was equal to 0.1 mA/V. The operating beam voltage, V_b, was then taken as 200 V above $(V_b)_{min}$. The ion-optics operating voltage, V_T, was then defined as:

$$V_T = (V_b)_{min} + 200 + |V_A| \quad (1)$$

The operating value of the net-to-total accelerating-voltage ratio was calculated as $R = V_b/V_T$. Table 7 summarizes the values of $(V_b)_{min}$, V_A, V_T , and R as a function of beam current.

Table 7. Perveance Data for Ion Optics S/N 907

J_b (A)	$(V_b)_{min}$ (V)	$V_b = (V_b)_{min} + 200$ (V)	V_A (V)	$V_T = (V_b)_{min} + \lvert V_A \rvert + 200$ (V)	R
0.6	385	585	-140	725	0.81
0.8	465	665	-140	805	0.83
1.2	475	675	-220	895	0.75
1.8	660	860	-220	1080	0.80
2.4	685	885	-310	1195	0.74
3.0	820	1020	-310	1330	0.77
3.6	965	1165	-310	1475	0.79

Figure 17 is a perveance plot of the data presented in Table 7. For comparison, similar data obtained at NASA are also shown. There is excellent agreement between the Hughes and NASA results for the power-law parameter, n. However, the actual perveance, P, is slightly greater for the data obtained at Hughes. The Hughes data indicate a lower total voltage requirement of as much as 125 V.

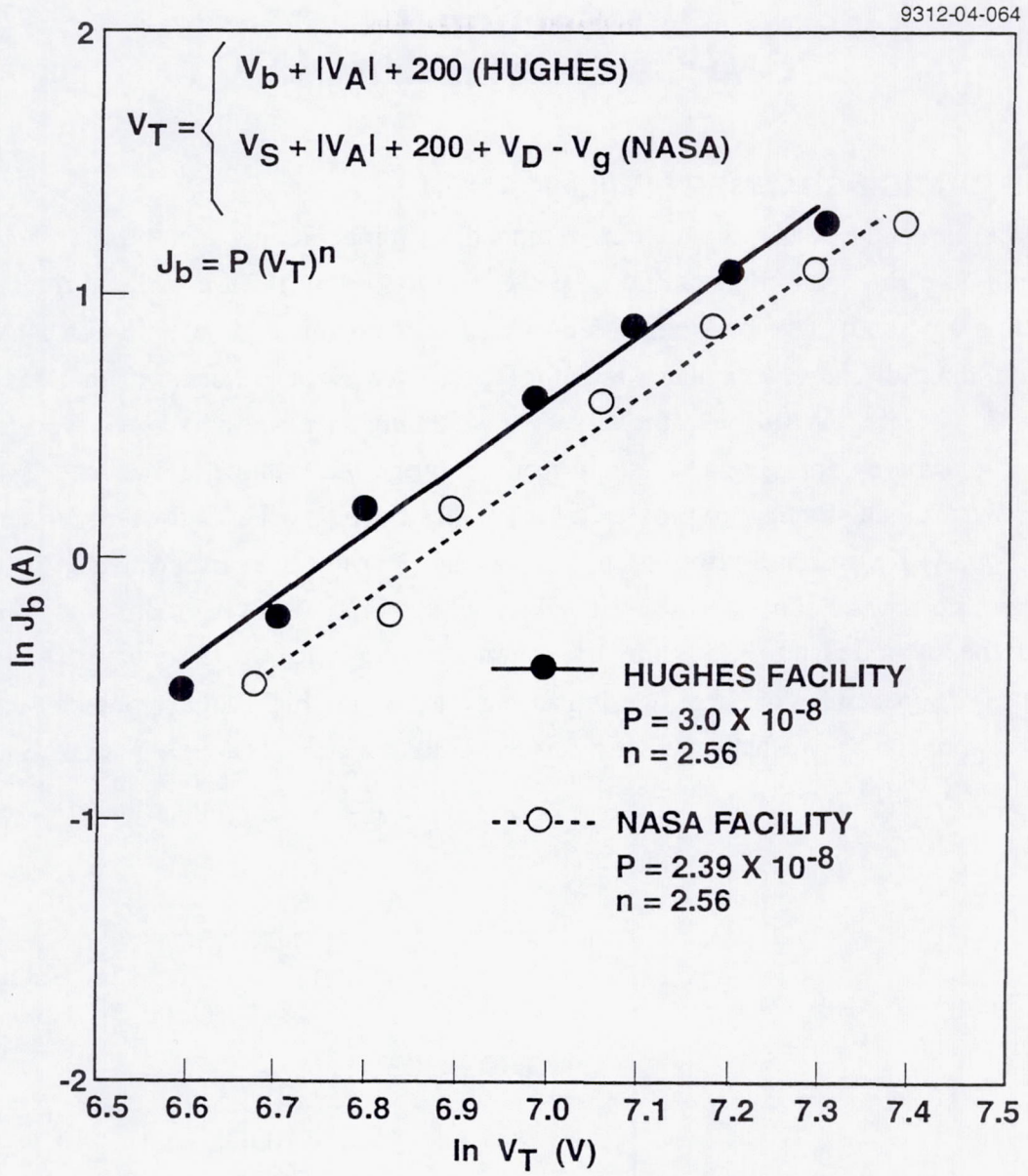

Figure 17. Comparison of perveance data obtained at Hughes and LeRC for ion optics S/N 907 operated on common thruster S/N 2.

Section 3
COMPONENT TECHNOLOGY

3.1 DISCHARGE-CHAMBER SIMPLIFICATION

We explored the feasibility of eliminating the cathode-keeper electrode as a means of simplifying the ring-cusp thruster and its power processor unit (PPU), while at the same time eliminating a potential erosion site[3] within its discharge chamber. Figure 18 is a schematic of the 30-cm-diam discharge-chamber simulator (operated without ion-beam extraction) that was used in these tests. With the cathode-keeper assembly in place as shown, we ignited the discharge plasma by applying a voltage directly between the cathode and anode. Two power supplies were diode-summed to provide a high-voltage boost ($\leq$ 1 kV) for ignition and a high current ($\leq$ 5 A) for sustaining the discharge plasma. During these experiments, the cathode-keeper assembly was electrically isolated and allowed to float. With 0.7 sccm of xenon flowing through the cathode and $\approx$23 sccm of xenon flowing into the discharge chamber, we demonstrated repeatable discharge ignitions using a maximum high-voltage boost of only 90 V. Steady-state operation was achieved at a cathode-emission current of $J_E = 5$ A and a discharge voltage of $V_D = 30$ V.

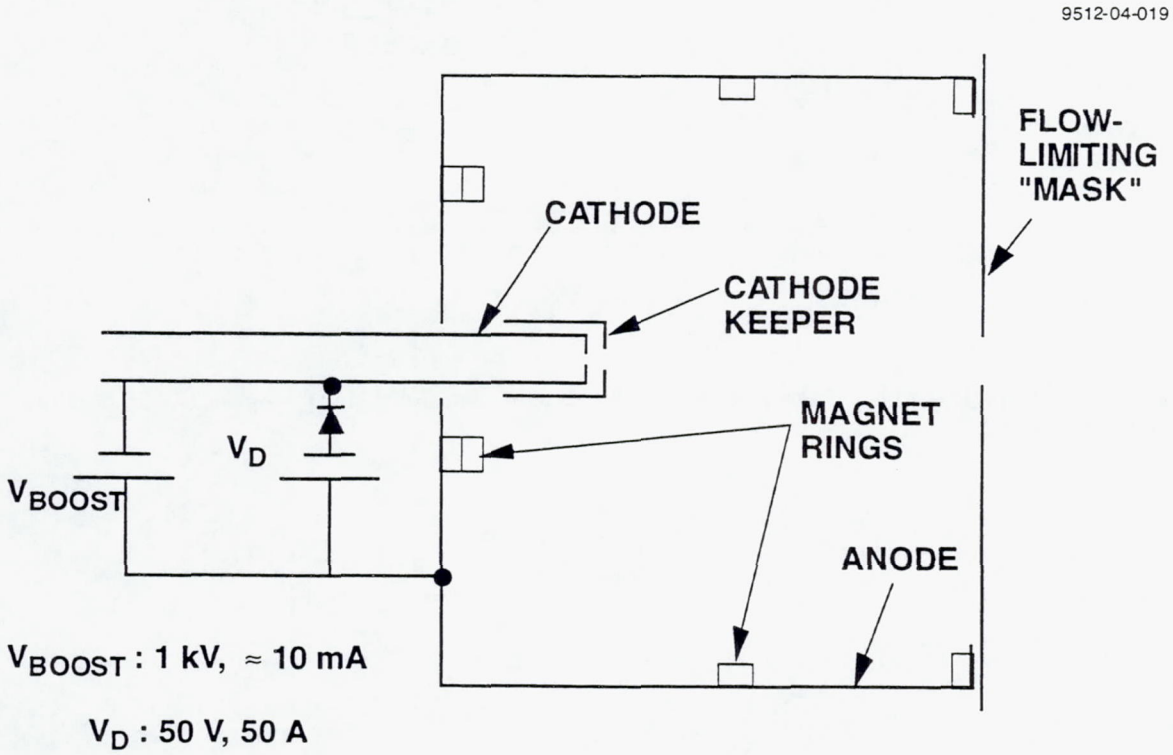

Figure 18. Electrical schematic of discharge-chamber simulator.

Next, we removed the enclosed-type keeper in a 30-cm-diam lab-model thruster, and the keeper supply in our laboratory test console was diode-summed with the discharge supply to provide a high-voltage boost capability. We successfully started and operated the lab-model thruster in this configuration (with ion-beam extraction). The adequacy of our high-voltage-recycle algorithm for this "keeperless" operation was also demonstrated. Although our recycle algorithm cuts the discharge current back to zero while reestablishing the screen and accel voltages, the discharge current provided by the high-voltage starting supply was adequate to keep the cathode from extinguishing during ≈2-sec-duration recycles.

3.2 CATHODE PERFORMANCE

A discharge-cathode assembly provided by NASA was evaluated using the discharge-chamber simulator shown in Figure 18. The evaluation consisted of conditioning the cathode insert according to a procedure specified by NASA, and then measuring the cathode temperature as a function of discharge current and cathode flow rate.

Figure 19 shows a schematic diagram of the cathode assembly that was provided by NASA, consisting of a 6.35-mm-diam hollow cathode equipped with an insert, heater, and radiation shield. The orifice diameter in the NASA-provided cathode was 0.762 mm. An R-type thermocouple (Pt/Pt-13% Rh) was spot welded to the side of the cathode tip, and a Granville-Phillips thermocouple gauge and readout were used to measure the pressure within the cathode. The discharge-chamber simulator was cleaned by grit-blasting its interior and then washing it with acetone and alcohol prior to installation of the NASA-furnished cathode. Plastic gloves were used to handle all cathode and discharge-chamber parts, and the xenon flow lines were baked out using a heat gun.

The cathode evaluation was conducted in the 0.3-m-diam cryopumped vacuum chamber; a schematic of this chamber is shown in Figure 20. The vacuum chamber is equipped with a Dycor Model MA200FG residual gas analyzer for measuring the partial pressures of various gases, including water vapor, nitrogen, and xenon. The typical background (no flow) pressure in this chamber is $\approx 6\times10^{-8}$ Torr.

3.2.1 Cathode Conditioning

Conditioning of the cathode insert was performed using a procedure provided by NASA. Table 8 shows the cathode-heater currents and voltages (I_{ch} and V_{ch}, respectively), as well as the cathode temperatures (T_c) that were measured during the low- and high-power phases of the conditioning sequence. The high-power conditioning temperature of T_c=1044°C was used as the cathode temperature for igniting the discharge in all subsequent testing.

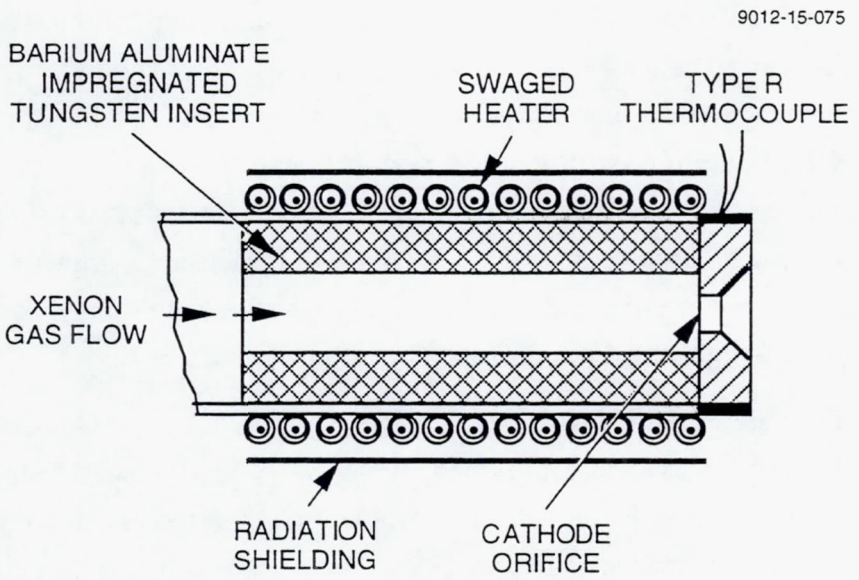

Figure 19. Schematic of discharge cathode in NASA/Hughes common thruster.

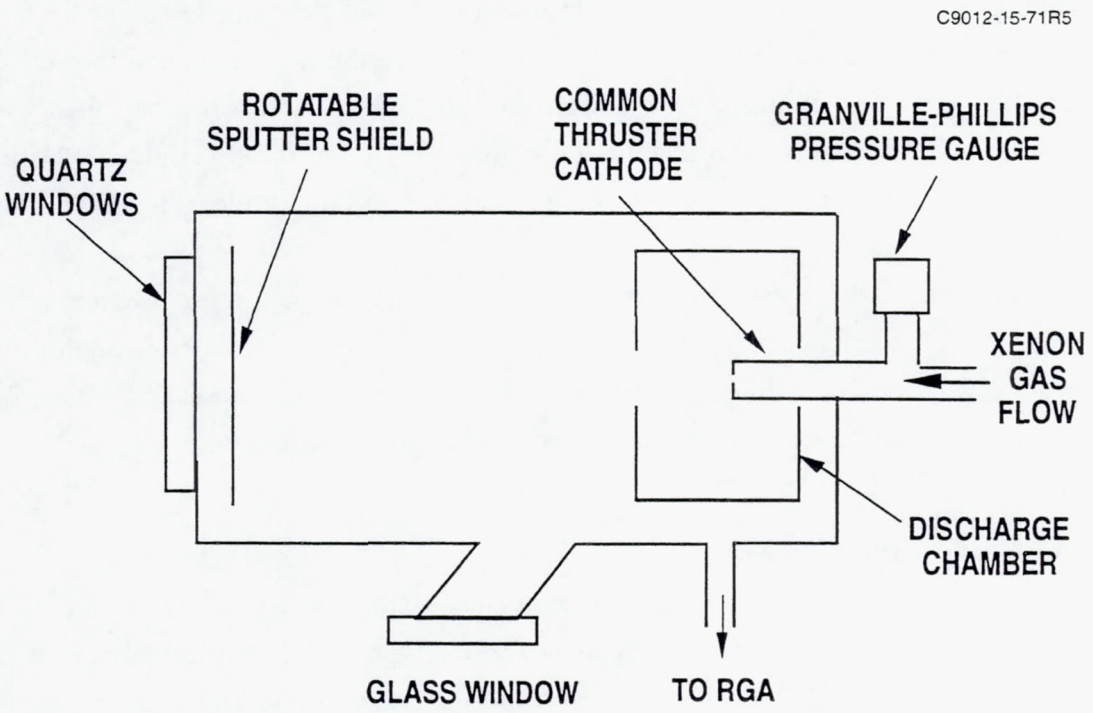

Figure 20. Schematic of 0.3-m-diam vacuum-chamber setup.

Table 8. Cathode Conditioning Log

Cathode Conditioning					
Power Level	I_{ch} (A)	V_{ch} (V)	P_{ch} (W)	T_c (°C)	Δt (h)
Low	4.32	3.4	14.6	532	3
Off	0	0	0	—	0.5
High	7.92	9.14	72.4	1044	1.0

3.2.2 Discharge Ignition

The cathode was evaluated over a five-day period. Each day the discharge was ignited by first applying the heater current specified in Table 8 to achieve a cathode temperature of 1044°C. After a selected flow rate was established, voltage was applied between the cathode and anode to achieve ignition and establish the discharge. This was accomplished by using a high-voltage-boost power supply (1 kV @ ≈10 mA) diode-summed with a low-voltage (50 V), high-current (50 A) power supply, as shown in Figure 18.

Table 9 shows a history of the discharge-ignition characteristics. On the first day of cathode operation, (following the previous day's cathode-conditioning sequence) a high xenon flow rate (i.e., gas burst) was required to initiate the discharge. For all subsequent cathode operation, normal ignitions were achieved at the nominal flow condition (4 sccm or 8 sccm), without the use of the high-voltage-boost power supply.

Table 9. Discharge Ignition Log

Day	Discharge Ignition Conditions		
1	Abnormal Start	Gas Burst	V_{Boost} Required
2	Normal Start	$\dot{m}$ = 4 sccm	V_D Only
3	Normal Start	$\dot{m}$ = 8 sccm	V_D Only
4	Normal Start	$\dot{m}$ = 4 sccm	V_D Only
5	Normal Start	$\dot{m}$ = 4 sccm	V_D Only

3.2.3 Cathode Heater and Thermocouple Behavior

Prior to igniting the discharge each day, the I/V characteristics of the cathode heater, as well as the thermocouple resistance, were measured to determine whether any changes in the thermocouple and heater had occurred. Table 10 shows the measured cathode temperature for the same heater power level.

Table 10. Cathode Heater Power Log

Cathode Heater Power				
Day	I_{CH} (A)	V_{CH} (V)	P_{CH} (W)	$T_{T.C.}$ (°C)
1	8.44	10.06	84.9	1044
2	8.44	10.0	84.4	1038
3	8.44	10.02	84.6	1040
4	8.44	10.04	84.7	1040
5	8.44	10.07	84.9	1039

*All measurements taken from cold start, (i.e., $T_c \approx 25°C$ at t = 0).

3.2.4 Temperature Measurements

Following ignition of the discharge, the variation of cathode temperature with emission current was obtained for two different flow rates. The emission current was set to its maximum value of $J_E = 25$ A, and the temporal behavior of the cathode temperature was recorded to determine when steady state had been reached. By our definition, the steady-state condition was reached when the cathode temperature was observed to change by less than 5°C over a 30-min time period. The emission current was then reduced in 5-A increments (down to a minimum value of $J_E = 5$ A), with the steady-state temperature determined in the manner just described. Figure 21 shows the temporal behavior of the cathode temperature for emission currents of 25, 20, and 15 A at a fixed flow rate of 4 sccm. At this flow rate, the emission current could not be increased above $J_E = 25$ A without the discharge voltage increasing to a value in excess of $V_D = 40$ V. Figure 21 indicates that for an emission current of $J_E = 25$ A, the cathode temperature initially rises to nearly 1280°C, and then decreases to a steady-state value of 1188°C in a 45-min period. For the other two emission currents shown ($J_E = 20$ A and $J_E = 15$ A), the steady-state temperature is achieved within a 15-min period.

Figure 22 shows the variation of the steady-state cathode temperature with emission current recorded over a three-day period. The data indicate good reproducibility of measured temperatures. Figure 23 shows the corresponding discharge voltages. For each of the cathode-temperature measurements shown in Figure 22, the cathode pressure was recorded using a thermocouple gauge (see Figure 20 for location of the pressure gauge). Figure 24 shows good reproducibility of the cathode pressure over the three-day testing period. The data indicate that for fixed flow rate, the cathode pressure increases with emission current (cathode temperature). We explored this behavior further by using the ideal-gas law and the measured pressure (shown in Figure 24) and temperature (shown in Figure 22) to calculate the xenon density in the cathode.

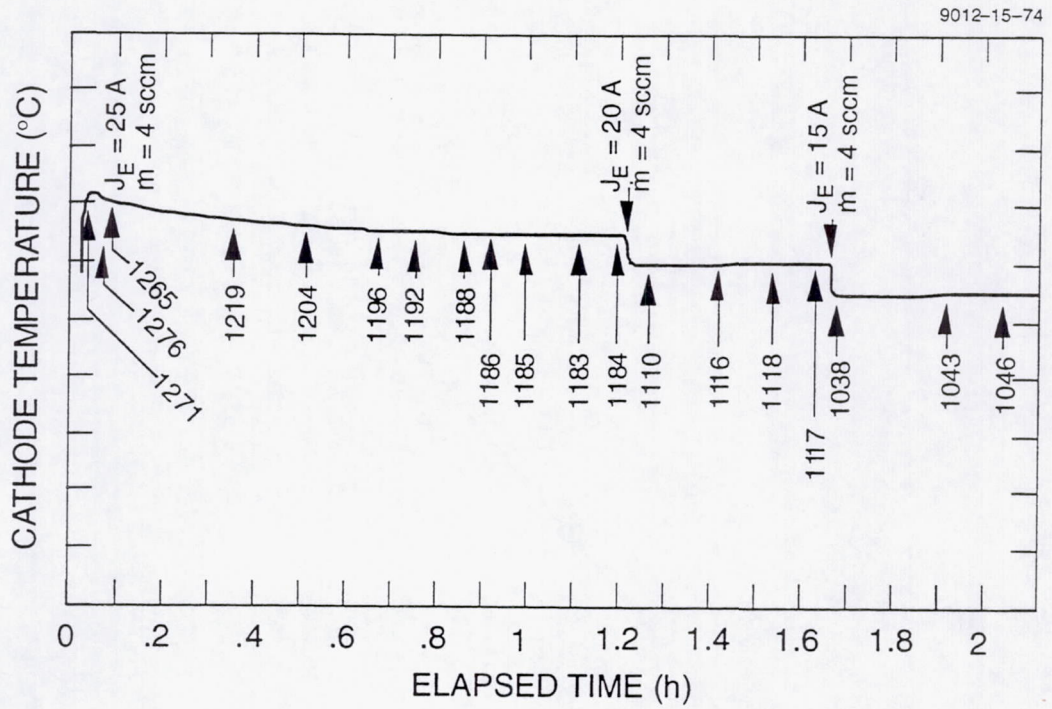

Figure 21. Strip-chart recording of cathode-temperature variation.

(The magnitude of the calculated densities may be in error because the pressure-gauge manufacturer was unable to provide a factor for converting indicated pressures to true xenon pressure). Figure 25 shows that the computed xenon density is approximately constant, as expected, indicating that the observed cathode pressure is a function of temperature only (for constant flow rate). Figures 26-28 contain cathode-evaluation data for the cathode operated at a flow rate of 8 sccm. The data exhibit a behavior similar to that observed at a flow rate of 4 sccm.

Figure 29 shows the temporal variation of cathode temperature for a flow rate of 8 sccm and a discharge current of 30 A. There is a linear decrease in temperature with time during the first 1.5 h, and then the cathode temperature reaches steady-state conditions. The data in Figure 30 show that the measured partial pressures of water vapor, nitrogen, and xenon, remain constant and do not correlate with changes in cathode temperature.

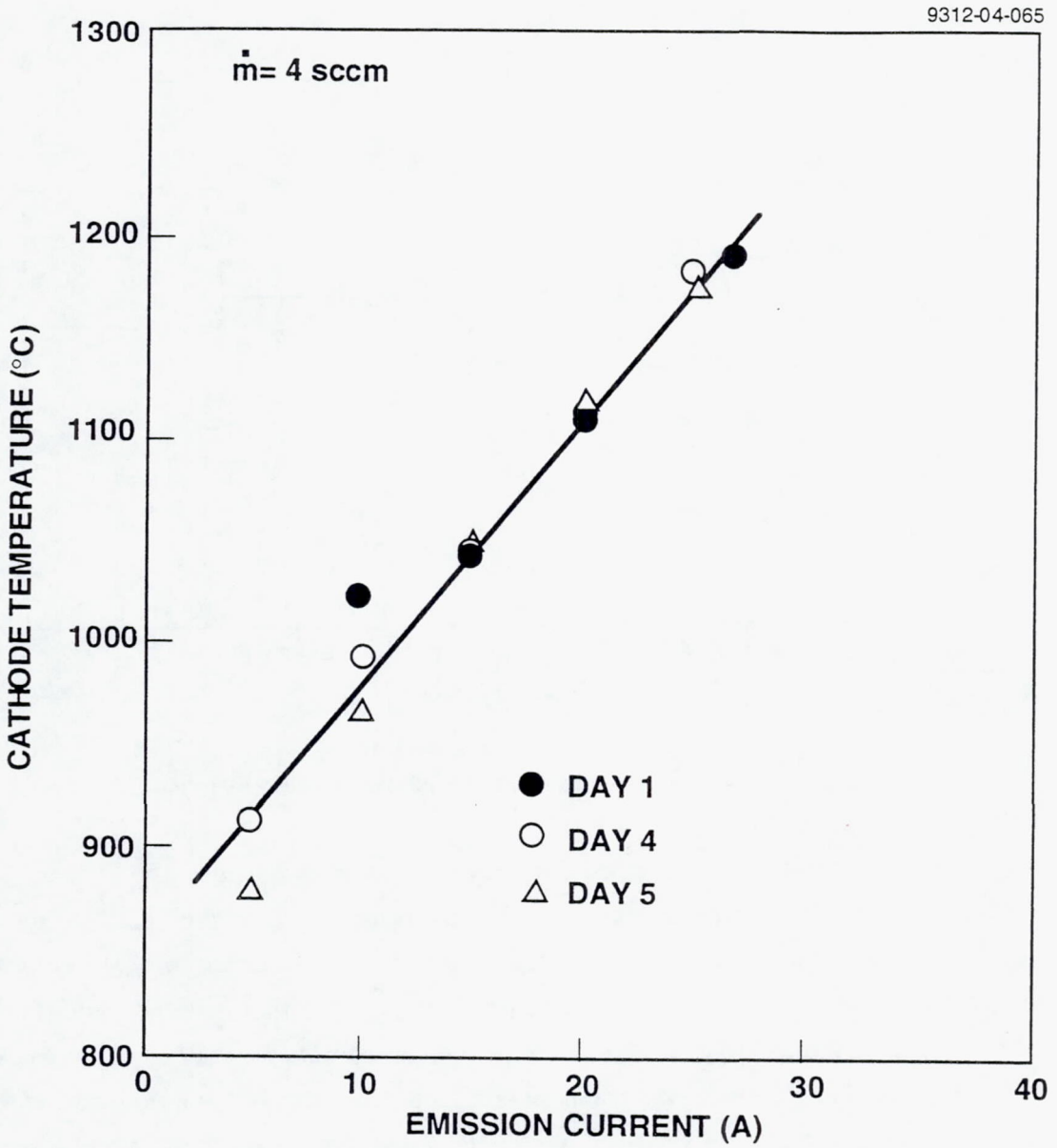

Figure 22. Variation of cathode temperature with emission current (4 sccm flow rate).

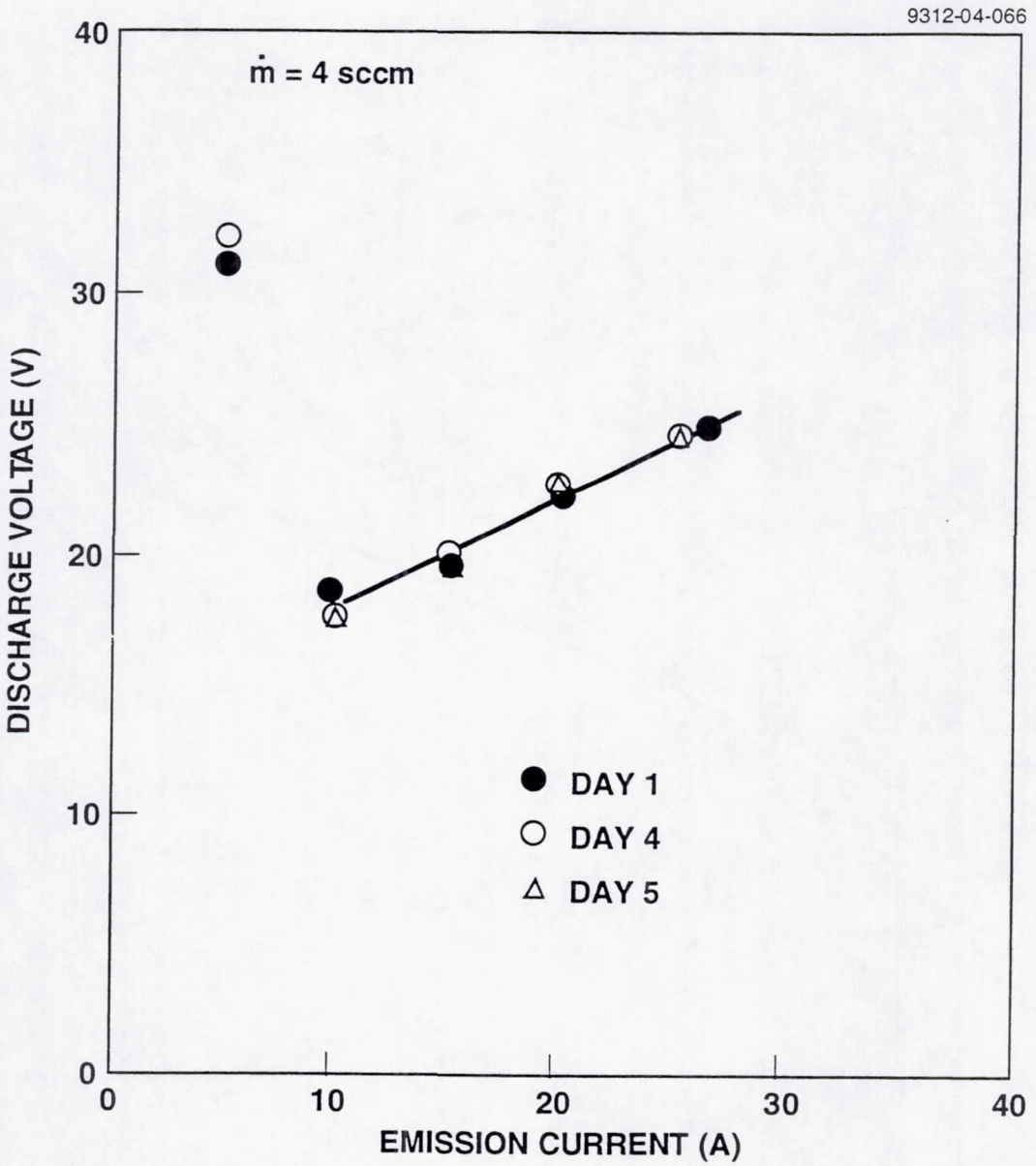

Figure 23. Variation of discharge voltage with cathode-emission current (4 sccm flow rate).

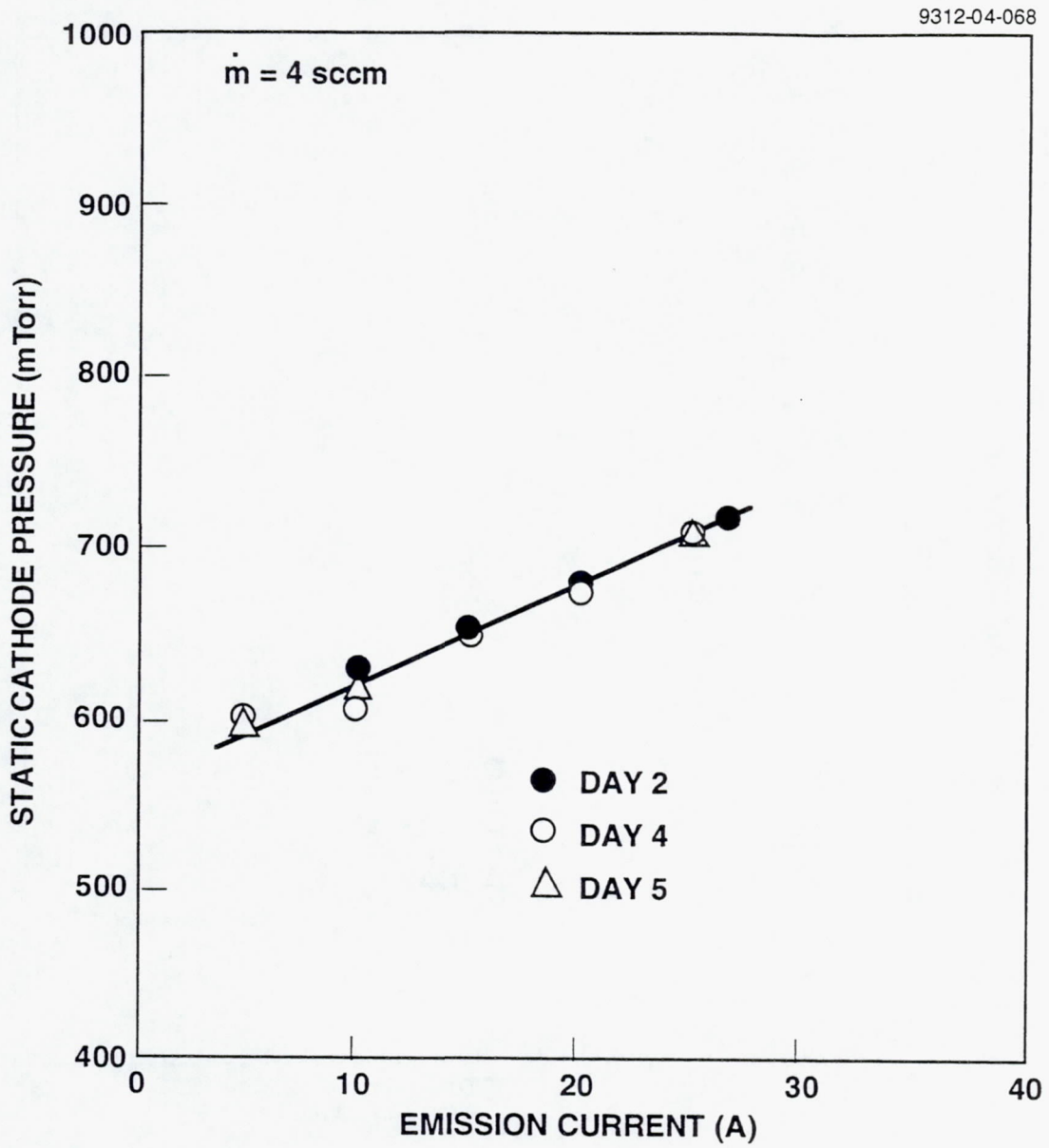

Figure 24. Variation of cathode pressure with emission current (4 sccm flow rate).

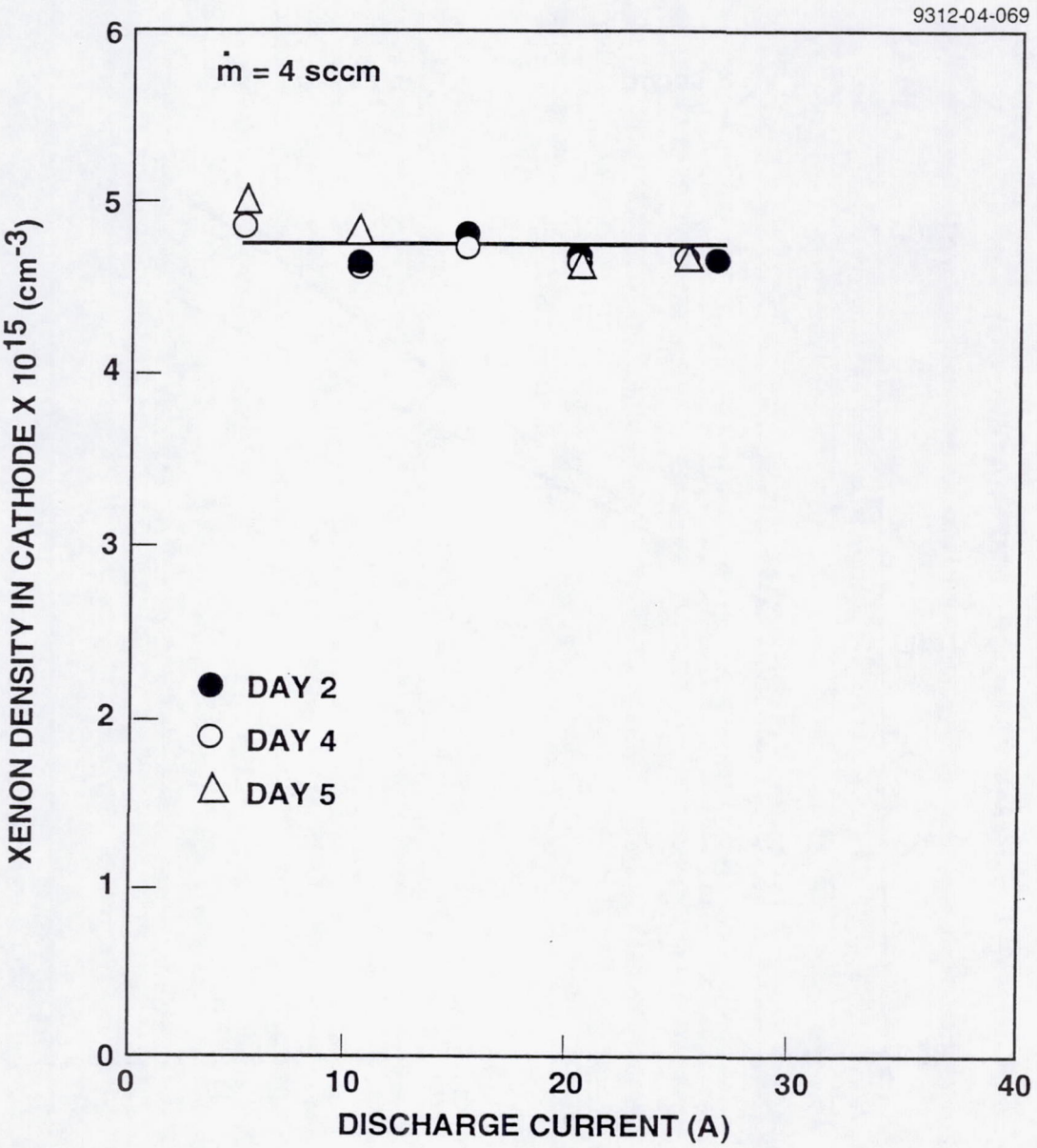

Figure 25. Calculated xenon gas density within discharge cathode (4 sccm flow rate).

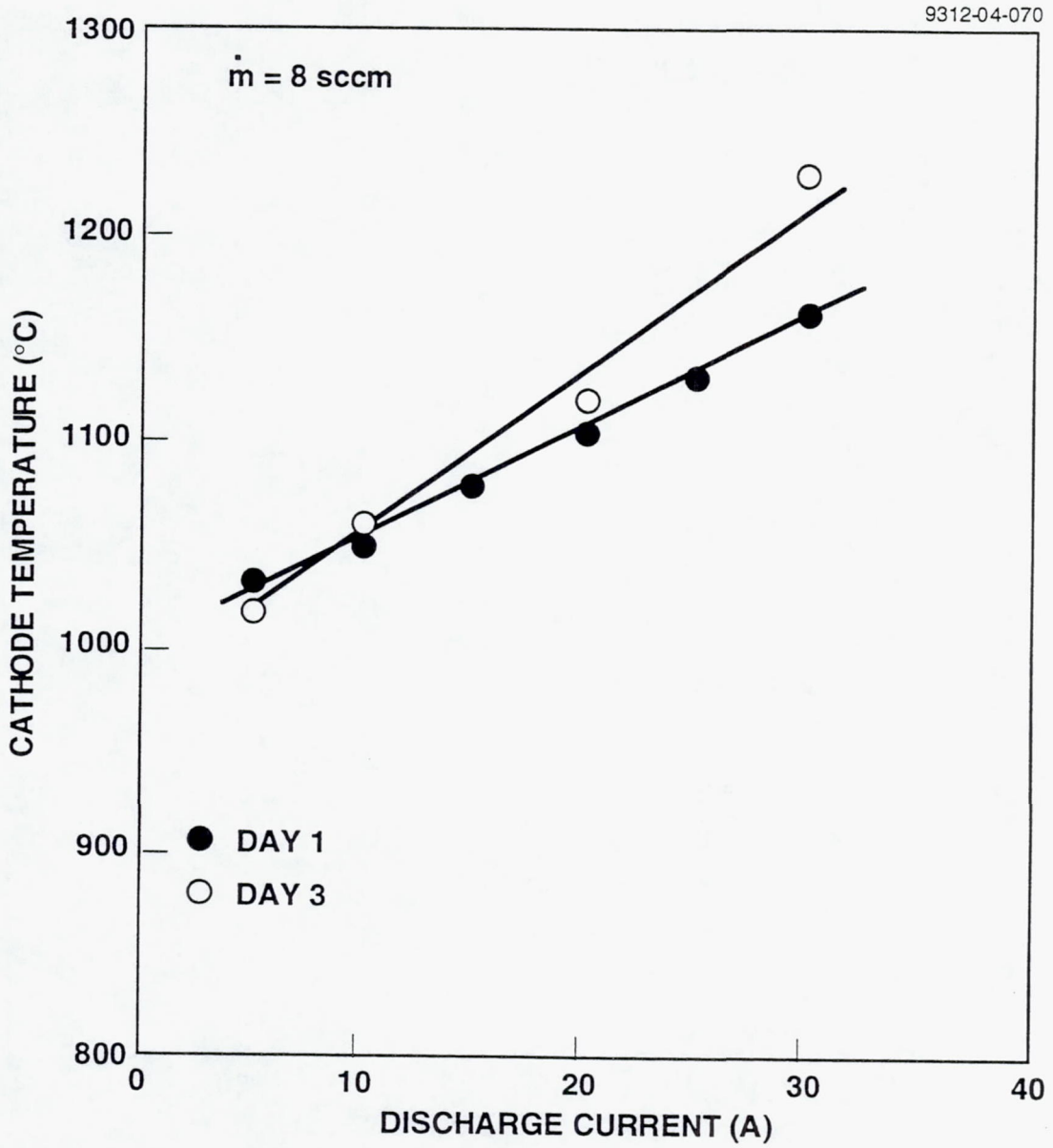

Figure 26. Variation of cathode temperature with emission current (8 sccm flow rate).

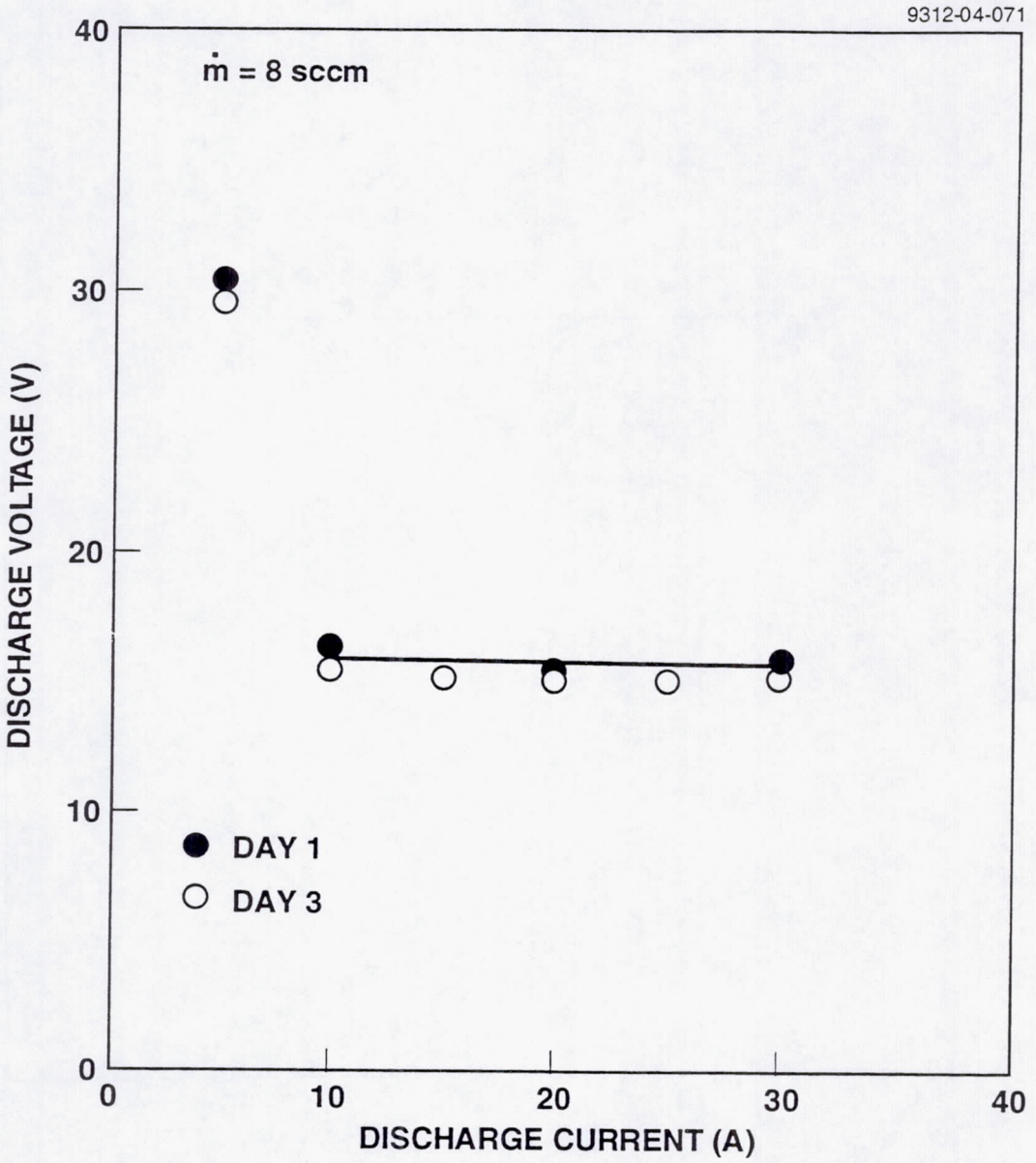

Figure 27. Variation of discharge voltage with cathode-emission current (8 sccm flow rate).

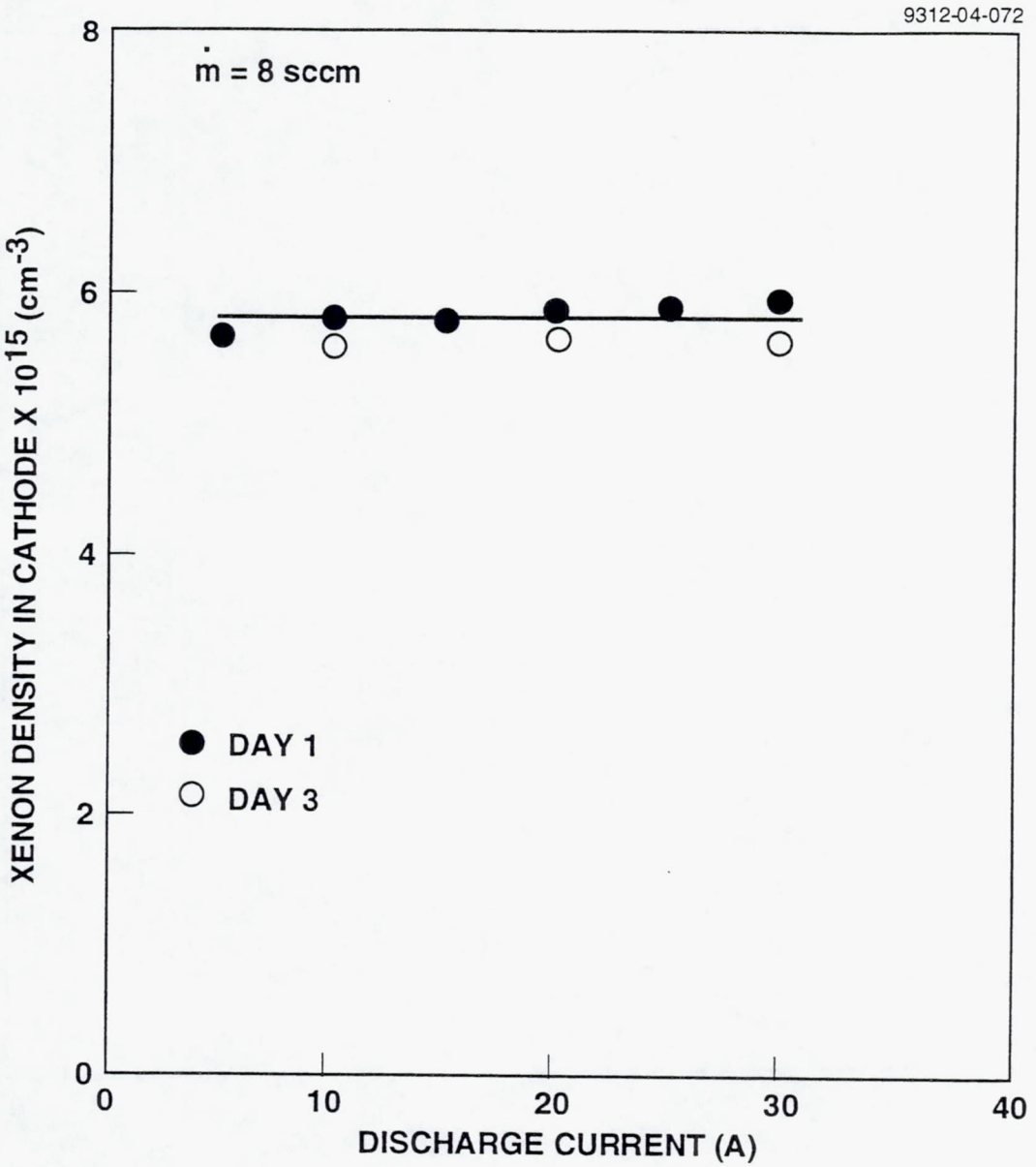

Figure 28. Calculated xenon density within discharge cathode (8 sccm flow rate).

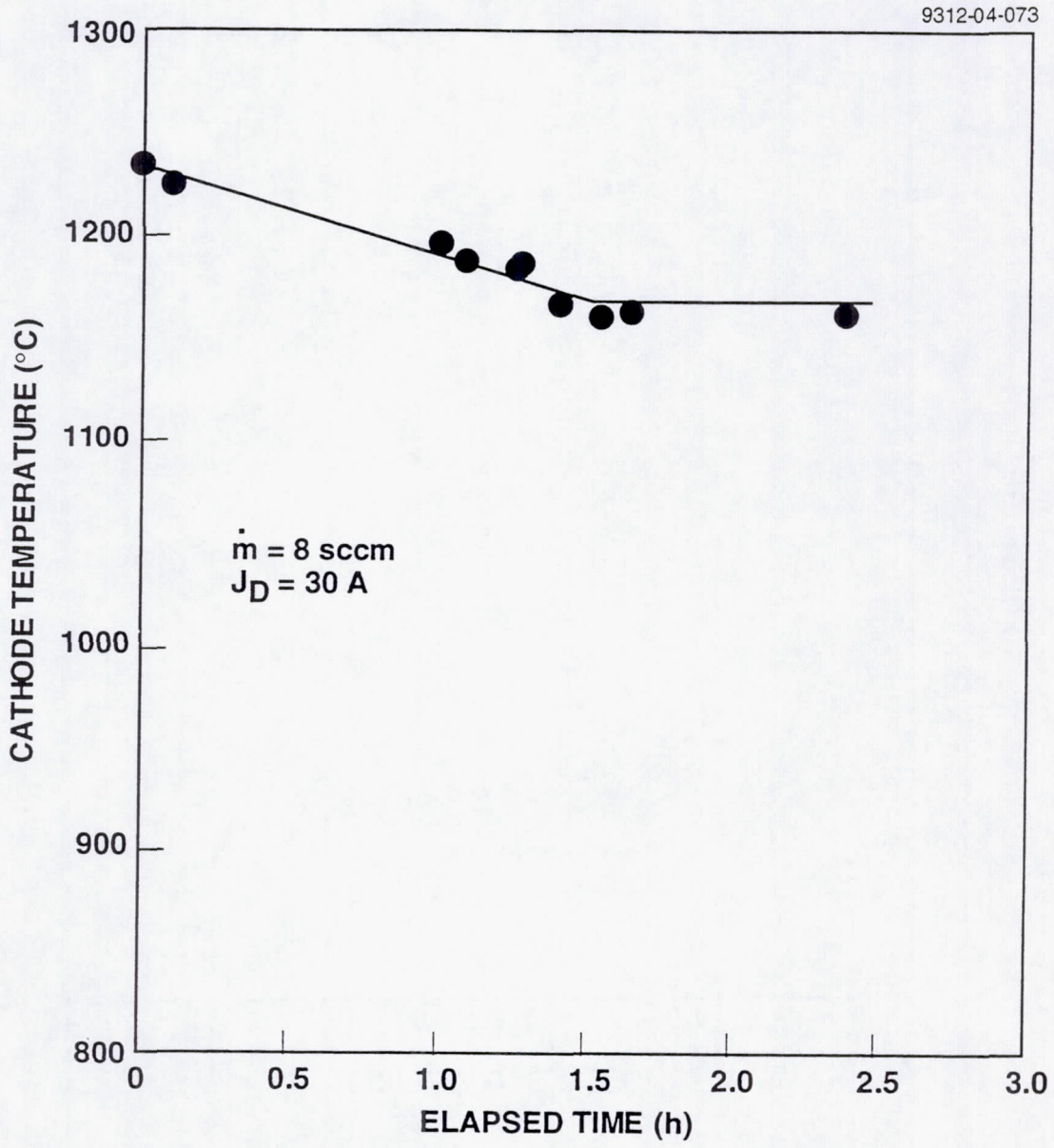

Figure 29. Temporal variation of cathode temperature (8 sccm flow rate).

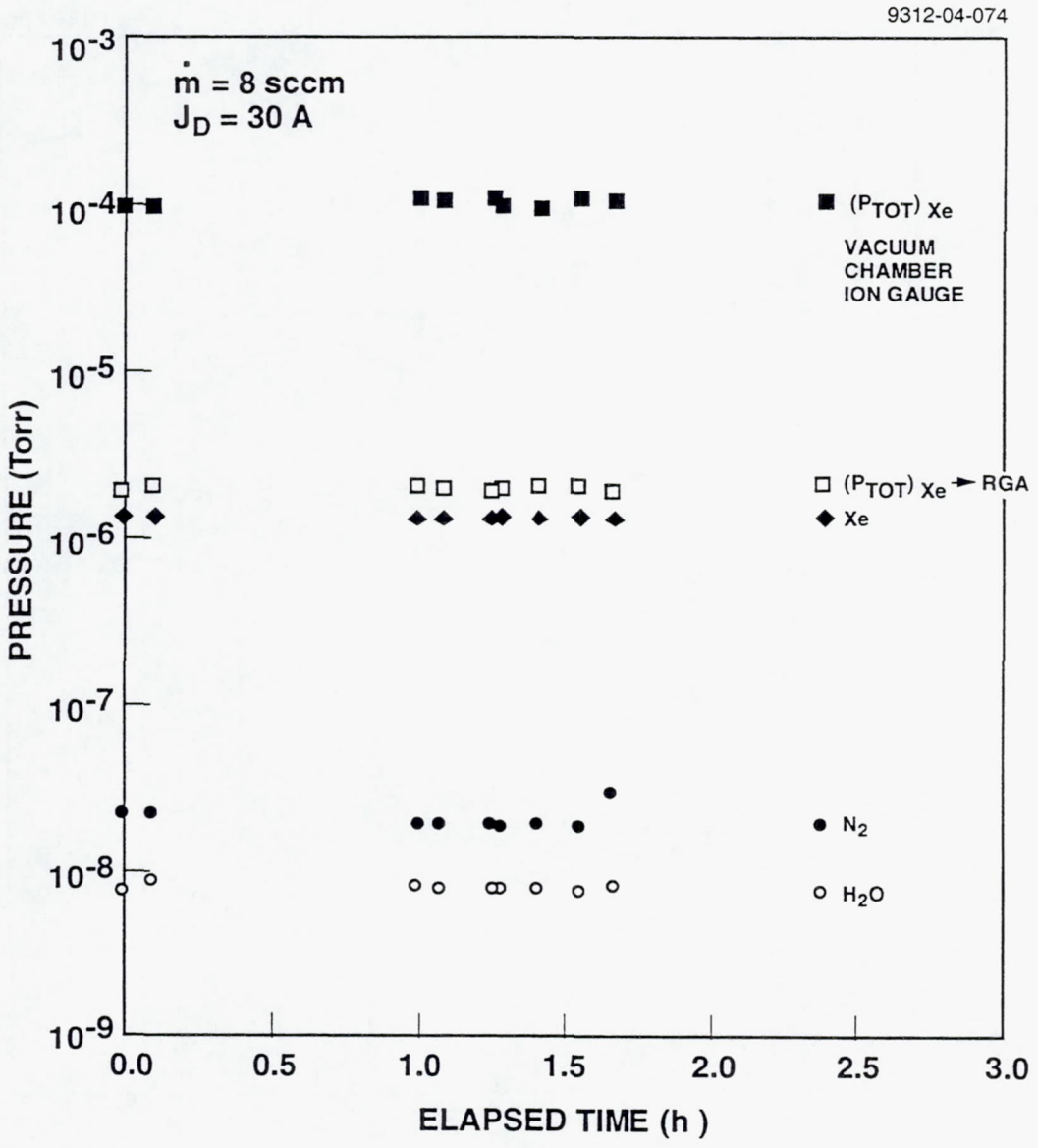

Figure 30. Temporal variation of background partial pressure (8 sccm flow rate).

Section 4
LASER-INDUCED FLUORESCENCE

4.1 FEASIBILITY ANALYSIS

In laser-induced fluorescence, atoms are stimulated by an external resonant laser source, in addition to the inherent stimulation by the electrons in the plasma. The LIF signal is independent of the plasma conditions, provided the plasma does not significantly affect the density of the ground-state atoms. We selected the ground state atomic transition process (λ = 390.2 nm) for molybdenum atoms that provided the largest fluorescence signal for a given laser power.

Plasmas produced in ion thruster discharge chambers are characterized as partially ionized (~10%), low-pressure (~10^{-5}–10^{-4} Torr) plasmas, with an average electron temperature of 2-5 eV and plasma densities on the order of 10^{10}–10^{11}cm^{-3}.[4] For these plasma parameters, less than 1% of the molybdenum atoms sputtered from a surface exposed to the plasma are raised to excited states as a result of collisions with electrons.[4] In order to achieve a high signal-to-noise ratio (large ratio of the laser-induced to collision-induced signals) in the laser-induced fluorescence method, the excitation of molybdenum atoms must be dominated by laser photon absorption. Therefore, we must determine the ratio of laser-induced to collision-induced excitation rates of molybdenum atoms as a function of laser intensity. Note that the following equations employ Gaussian units.

The rate for atomic stimulated excitation, R_{re}, is given in terms of the Einstein A coefficient as[5]

$$R_{re}(i \rightarrow j) = \frac{g_j}{g_i} \frac{\pi \hbar^2 c^2 I A_{ji} g}{2\chi_{ij}^3} \quad , \tag{1}$$

where g_i and g_j are the degeneracies for atomic levels i and j, respectively, I is the intensity of the radiation, A_{ji} is the Einstein A coefficient, and χ_{ij} is the energy difference between levels i and j. The Doppler distribution function g, evaluated at line center of the transition, given by[6]

$$g = \frac{h}{\chi_{ij}} \sqrt{\frac{M_A c^2}{2\pi k T_A}} \quad , \tag{2}$$

where k is Boltzmann's constant, M_A and T_A are the mass and temperature of the molybdenum atom, respectively, and h is Planck's constant. Since the energy distribution of sputtered atoms from a surface subjected to ion bombardment is ~1-2% of the incident ion energy,[7] kT_A~1 eV for the conditions of our experiment.

A semi-empirical formula for the electron-impact (collision-induced) excitation rate between states i and j, $R_p(i \rightarrow j)$, is[8]

$$R_p(i \rightarrow j) = 16\sqrt{\frac{2\pi}{3m_e}}\frac{R_\infty^2}{\sqrt{kT_e\chi_{ij}}}exp\left(-\frac{\chi_{ij}}{kT_e}\right)f_{ij}\bar{g}\pi a_o^2 n_e \quad , \tag{3}$$

where m_e is the electron mass, R_∞ is the Rydberg energy (13.51 eV), T_e is the electron temperature, f_{ij} is the oscillator strength for the transition form level i to level j, $\bar{g}$ is the energy-averaged Gaunt factor (a correction factor), a_O is the Bohr radius, and n_e is the electron density. Under our operating conditions $\bar{g}$ is assumed to be unity.

The use of Eq. (3) assumes that the electron energies can be characterized by a local Maxwellian energy distribution which has been shown to adequately describe the electrons in ion thruster discharge chambers.

Equation (3) can be cast into a form that allows for a more convenient comparison to radiative excitation by relating the oscillator strength to the Einstein A coefficient by[5]

$$f_{ij} = \frac{m_e c^3 \hbar^2 g_j A_{ji}}{2e^2 g_i \chi_{ij}^2} \quad . \tag{4}$$

In terms of fundamental constants and the spontaneous decay from the excited state, the plasma excitation rate is given by

$$R_p(i-j) = 2\sqrt{\frac{2\pi^3 m_e c^2}{3kT_e}}\frac{\hbar^2 c^2 e^2 g_j A_{ji} n_e}{\chi_{ij}^3 g_i}exp\left(-\frac{\chi_{ij}}{kT_e}\right) \quad . \tag{5}$$

Assuming that the decay processes and rates are the same for atoms excited by either plasma electrons or optical photons, the relative intensity of the LIF signal compared to the background (plasma-induced) fluoresecence signal is given by the ratio of the excitation rates for the two processes

$$\frac{R_{re}}{R_p} = \frac{Ig}{e^2 n_e}\sqrt{\frac{3kT_e}{2\pi m_e c^2}}exp\left(\frac{\chi_{ij}}{kT_e}\right) \quad . \tag{6}$$

For operating conditions where the Doppler width is larger thatn the laser linewidth, the appropriate value of g to use is given by Eq. (2). Assuming kT_A=1 eV and $2\pi\hbar c/\chi_{ij}$ = 3902 Å yields g = 1.55×10^{-10} s. In the experiment discussed later, we used an ultraviolet beam from a Coherent 599 dye laser with an intensity of approximately 2 W/cm^2. Equation (6) can then be evaluated using the parameters $n_e = 10^{11}$ cm^{-3}, kT_e=3 eV, and χ_{ij}= 3.18 eV. This gives a value of 650 for the ratio R_{re}/R_p, which is large enought to provide ample signal for determining the molybdenum density.

This calculation applies to the same volume of atoms for both excitation modes (plasma and radiative). In paractice, the geometry of the measurement is very important and it is difficult to

completely isolate the volume of atoms intercepted by the laser beam to avoid fluorescence contributions from other regions where the excitation mechanism is solely collisional. Although shielding was used in the experiment to minimize this additional contribution, a sizeable plasma background signal was present. Therefore, a phase-sensitive detection technique, described in Section 5.2, was employed and achieved a high signal-to-noise ratio. However, it was still necessary to keep the background fluorescence contribution small in order to avoid saturation of the detector.

Commercially available Ti:Sapphire lasers are much easier to maintain than a dye laser system and would probably be selected as the optical source in a practical diagnostic station. Using internal cavity doubling, these lasers can produce 200 mW of output power at 390 nm, which is resonant with the lowest lying dipole-allowed molybdenum ground state transition. If this beam is collimated to a 1 cm^2 spot, the intensity I would be 200 mW/cm^2. This gives a value for R_{re}/R_p of 65 for the Ti:Sapphire laser, which should produce a reasonable signal-to-noise ratio.

4.2 FEASIBILITY DEMONSTRATION

Our initial efforts to implement LIF as a wear-rate diagnostic involved a pulsed laser system, which was chosen because of its availability and relative simplicity. We evaluated the effectiveness of using this laser with a UV dye as the gain medium. However, during the characterization of this optical source we concluded that the lifetime of its dye was so short (about 100 shots) that it could not be used effectively in a long-term diagnostic study. Therefore, we switched to a continuous-wave laser source consisting of a Coherent Model I-18 argon laser operating in the 350- to 360-nm spectral range, and a Coherent Model 599 standing-wave tunable dye laser capable of emitting radiation at the relevant molybdenum resonance (λ = 390.2 nm). In this arrangement (illustrated schematically in Figure 31), the argon laser serves as an optical-pump source for the dye laser.

Coarse frequency tuning of the dye laser was accomplished with an intracavity birefringent tuning element, which serves as a low-loss element (Brewster-angle plate) for a narrow range of frequency (≈200 GHz). The absolute position of this frequency pass band was adjusted by rotation of the tuning element. Etalons within the laser cavity were used to spectrally narrow the laser emission to a single frequency, with a jitter of less than 20 MHz. A beam splitter directed a small portion of the output from the dye laser into a monochromator in order to monitor the wavelength. The fluorescence emerging from the vacuum test chamber passed through a narrow-band filter (≈6-nm full bandwidth) into a solar-blind (unresponsive to wavelengths in the visible region of the spectrum) photomultiplier tube.

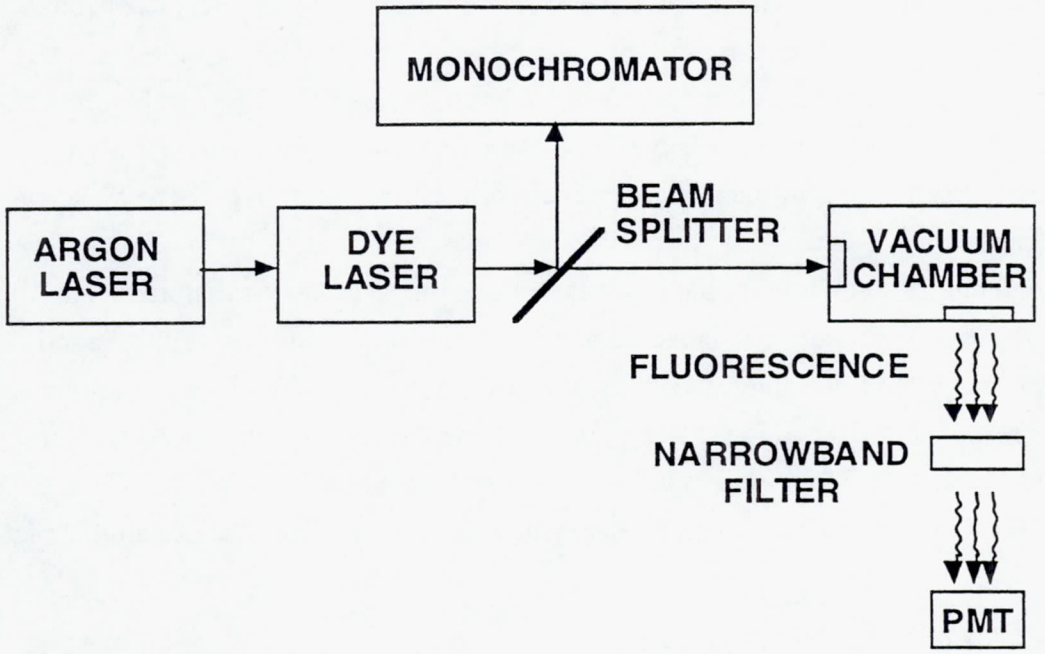

Figure 31. Schematic diagram of off-line setup to demonstrate LIF wear-rate diagnostic.

A photograph of the experimental test setup is shown in Figure 32. (The monochromator is not visible in the photograph.) The output of the argon laser was directed into the dye laser with a pair of turning mirrors. A pair of beam-elevating mirrors then directed the majority of the dye-laser output into the vacuum test chamber. Diagnostic equipment (including a narrow-band filter and photomultiplier tube) was located at the far end of the vacuum chamber. The discharge-chamber simulator used to produce sputtered-molybdenum efflux is shown in Figure 33. The spiral-wound molybdenum ribbon visible on the chamber centerline could be electrically biased to effect a change in the molybdenum sputtering rate.

Figure 34 shows a schematic diagram of the experimental setup. The LIF technique consists of focusing a laser beam into a region containing sputtered molybdenum atoms to induce fluorescence at the laser wavelength, which corresponds to an excited state of the molybdenum atom. The intensity of the laser-induced fluorescence detected by the monochromator is proportional to the density of molybdenum atoms, and, therefore, proportional to the erosion rate of the molybdenum surface from which the atoms are sputtered. By calibrating the LIF intensity with measured erosion rates, the technique can be used to provide a quantitative real-time measure of molybdenum erosion rates.

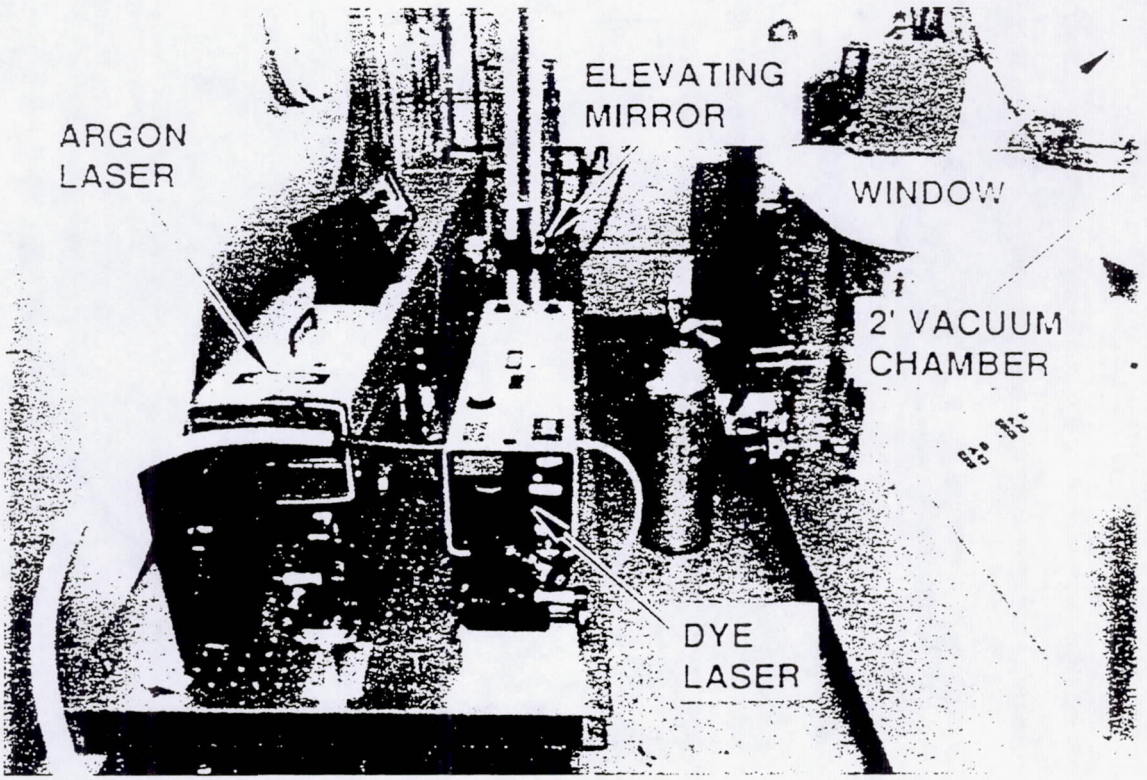

Figure 32. Photograph of experimental setup for investigating LIF wear-rate diagnostic.

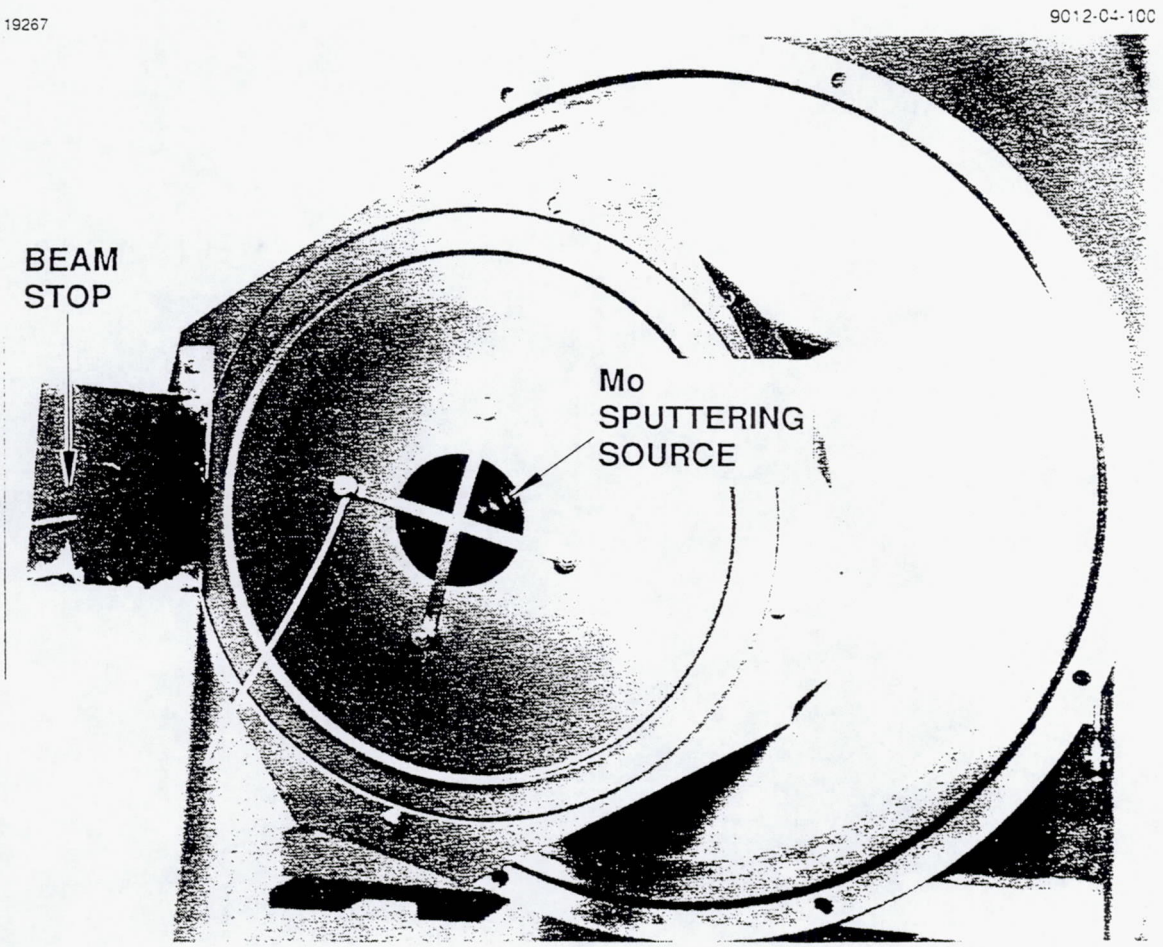

Figure 33. Photograph of discharge-chamber simulator for demonstrating LIF wear-rate diagnostic.

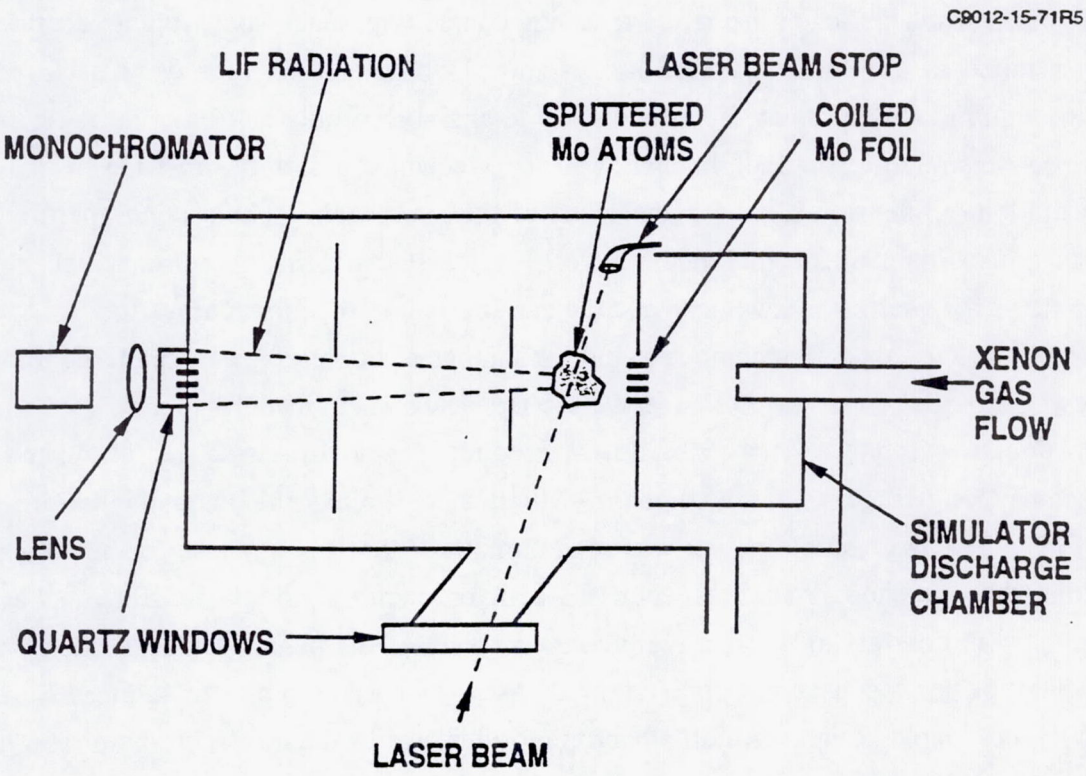

Figure 34. Schematic of LIF test setup.

A 30-cm-diam discharge-chamber simulator was used to provide a source of xenon ions for sputtering. The surface to be sputtered consisted of a spiral-wound coil of thin (0.005-mm) molybdenum foil that was electrically isolated and mounted at the 8-cm-diam exit aperture of the discharge-chamber simulator, as shown in Figure 34. With this arrangement, the sputtering rate of the molybdenum foil could be controlled by biasing it electrically, without affecting the plasma conditions within the discharge chamber.

A Spex Model 1700-II monochromator was used to measure the intensity of the laser-induced-fluorescence radiation, with a wavelength resolution of a few tenths of an Angstrom. A lens with a 60-cm focal length focused the radiation into the monochromator. The focal length of this lens was chosen to provide a close match to the f-number of the monochromator, in order to fill the grating and obtain the best possible resolution for a given setting of the entrance and exit slits. The output of the monochromator was fed into a photomultiplier tube.

The total signal detected by the monochromator consists of laser-induced fluorescence (LIF), plasma-induced fluorescence (PIF), and scattered laser light. Several features were incorporated into the vacuum chamber shown in Figure 34 to reduce the background signal arising from scattered laser light and plasma-induced fluorescence of the molybdenum atoms. An optically

black beam-stop (fabricated from quartz tubing coated with black soot from an acetylene torch) was installed to minimize scattered laser light. Two metal apertures were used to limit the background radiation produced by the discharge-chamber simulator. The first aperture, located 18-cm downstream of the molybdenum coil, is a rectangular slot 18-cm-wide by 1.3-cm-high, with the long dimension placed in the plane of the laser beam. The second aperture, (located 66-cm downstream of the molybdenum foil,) has a 10-cm-diam aperture, which is the same diameter as the quartz window located at the entrance slit of the monochromator.

In order to use the LIF technique to induce and detect fluorescence of sputtered molybdenum atoms, the output from the dye laser was set to a wavelength corresponding to the desired molybdenum resonance (λ = 390.2 nm). Frequency selection was accomplished with an intracavity birefringent tuning element, which also limited the laser bandwidth to about 300 GHz. The laser-output power was approximately 70 mW. The laser beam was amplitude modulated with a chopper at a frequency of 1 kHz, producing a modulated LIF signal at the same frequency (in contrast to the relatively constant level of the plasma-induced background). A lock-in amplifier was used to eliminate the dc background due to plasma-induced fluorescence. Both the dc-coupled output from the photomultiplier tube of the monochromator and the output from the lock-in amplifier were observed simultaneously on a dual-trace oscilloscope.

We demonstrated the LIF technique with the discharge-chamber simulator operated at a discharge voltage of V_D = 27 V and a cathode-emission current of J_E = 18 A. Figure 35 shows the LIF signal (top trace) and the total photomultiplier output (bottom trace) for the case where no bias voltage was applied to the molybdenum foil to enhance its sputtering rate. Note that the dc photomultiplier signal (lower trace) remains essentially zero, while the scattered laser light is observable in the top trace.

Figure 36 shows the effect of increasing the bias voltage of the molybdenum foil to enhance its sputtering rate. Figure 36(a) shows that the LIF signal increases by about a factor of 1.5 times the background level (which is caused by scattered laser light and previously shown in Figure 35) at a bias voltage of V_B = 70 V. As expected, the plasma-induced fluorescence signal increases as well. Figure 36(b) shows that increasing the bias voltage to V_B = 150 V results in an LIF signal that is a factor-of-two greater than the background level.

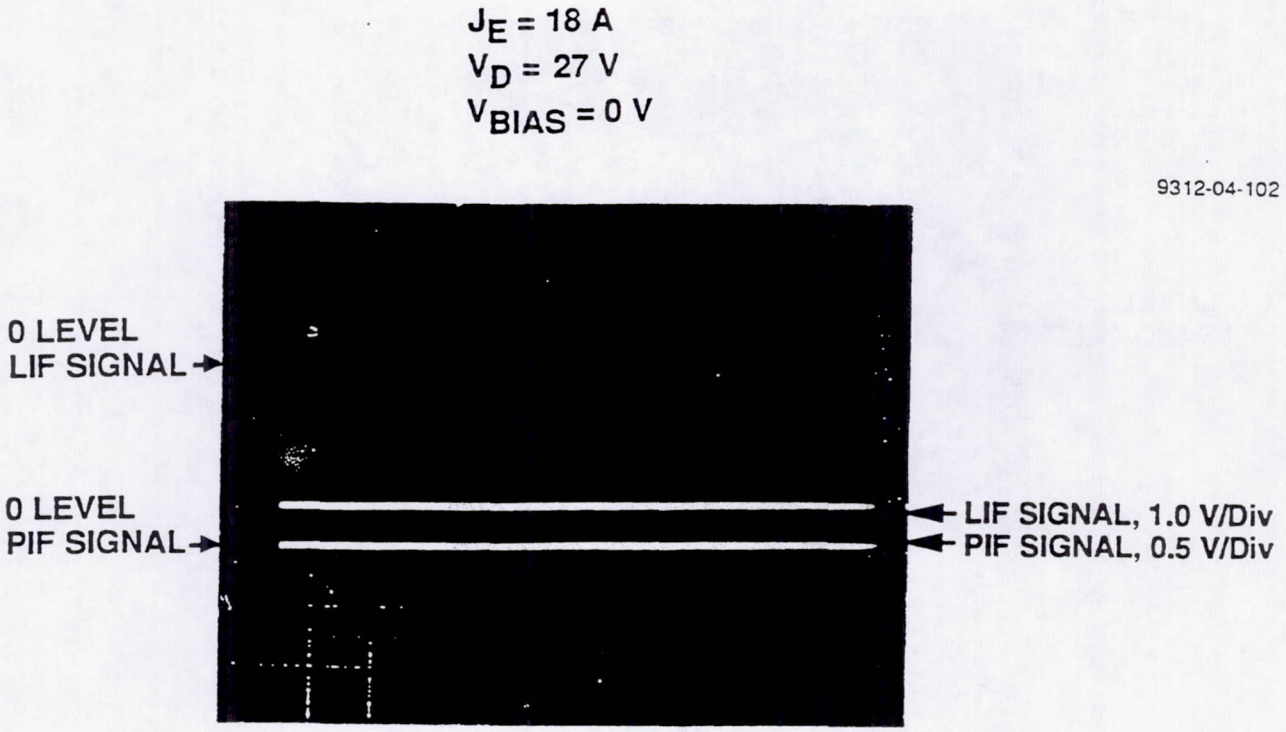

Figure 35. Laser-induced-fluorescence (LIF) and plasma-induced-fluorescence (PIF) signals at λ = 390.2 nm. *Standard plasma conditions and with no bias voltage applied to the Mo foil.*

We varied the plasma conditions by increasing both the discharge voltage (to V_D = 29 V) and cathode-emission current (to J_E = 20 A) to provide a higher flux of higher energy xenon ions for sputtering the molybdenum foil. Figure 37 shows that for a bias voltage of V_B = 150 V, the LIF signal is increased by nearly a factor-of-four over the background signal shown in Figure 32 (the oscilloscope sensitivity was reduced by a factor-of-two in Figure 37).

The results of Figures 35 to 37 demonstrated that the LIF technique can be used to detect sputtered molybdenum. For all of the measurements we obtained, the output level from the lock-in amplifier due to the LIF was on the order of Volts. A high signal-to-noise ratio was confirmed by blocking the laser beam at the entrance to the vacuum chamber and noting that there was no discernible background signal produced by the lock-in amplifier. The frequency jitter of the laser was large enough to cause its output to drift through the molybdenum resonance,

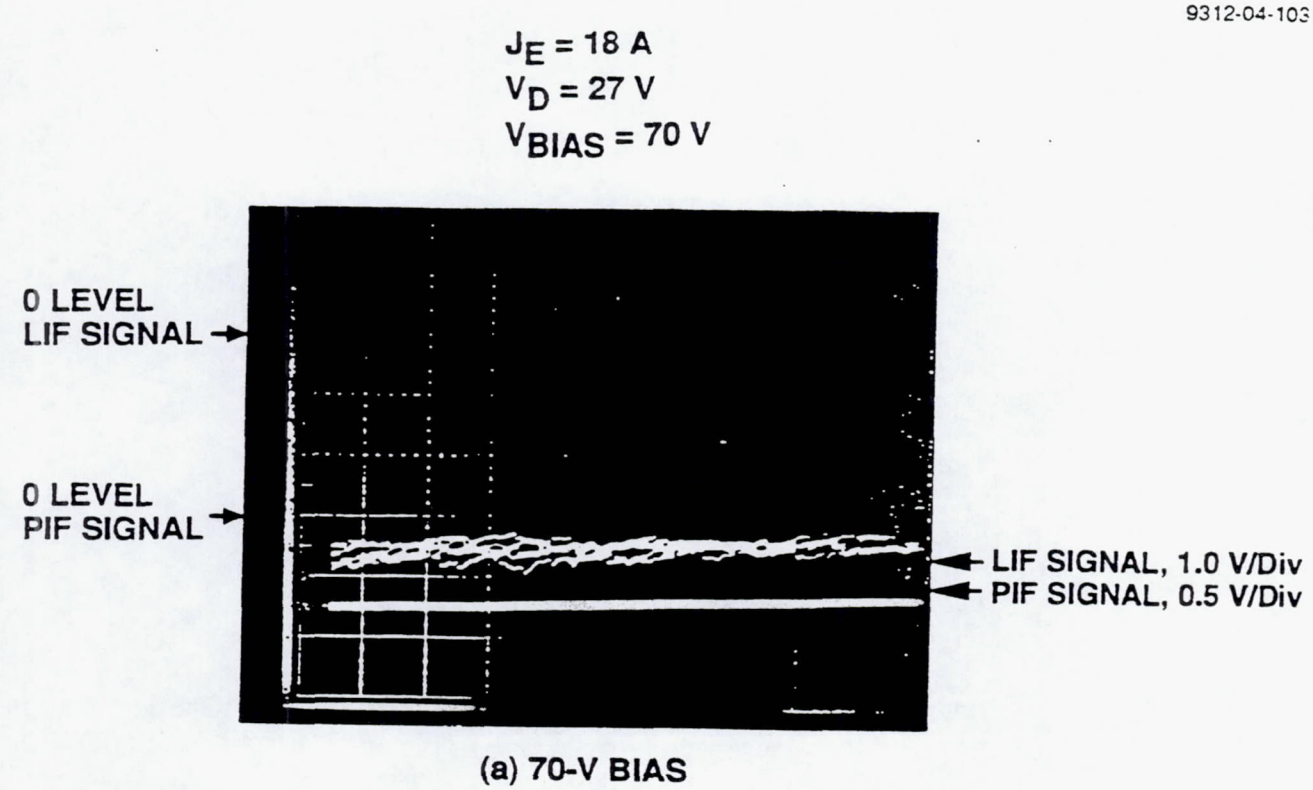

(a) 70-V BIAS

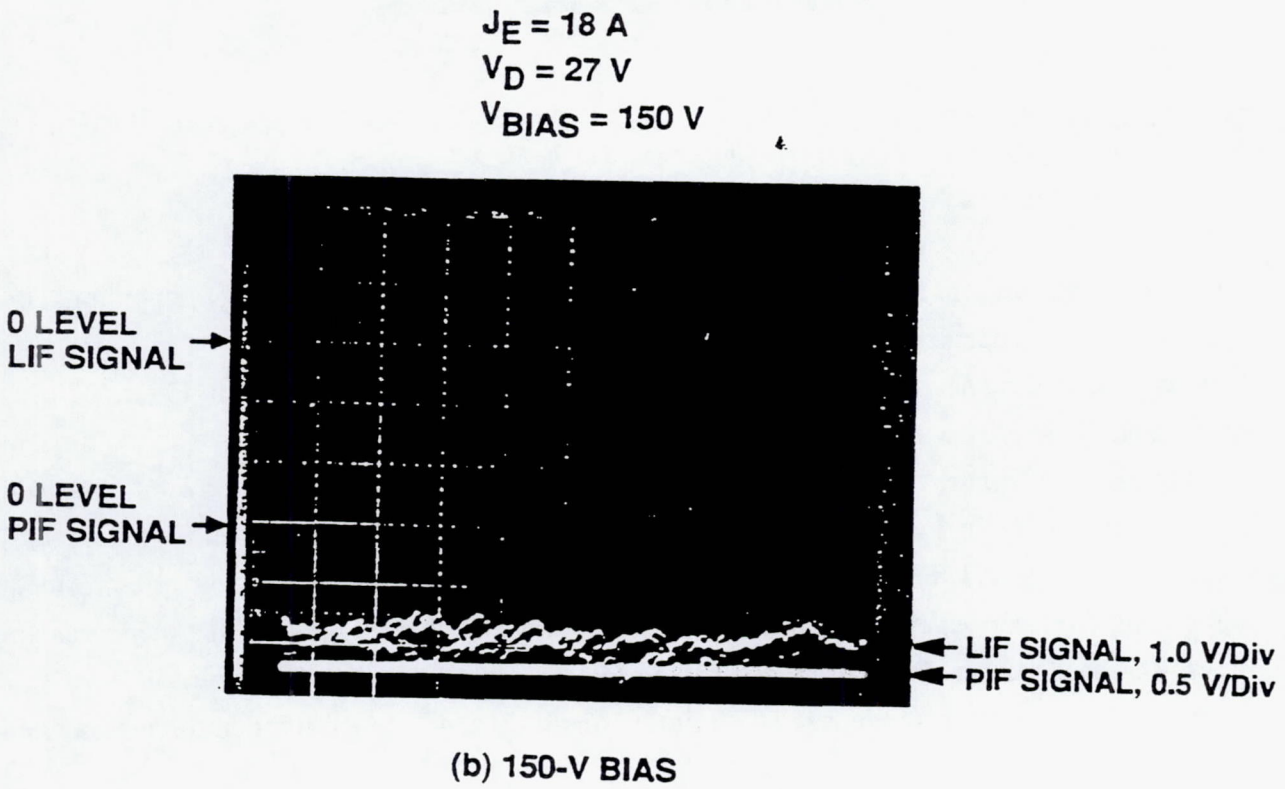

(b) 150-V BIAS

Figure 36. LIF and PIF signals at λ = 390.2 nm. *Standard plasma conditions and with bias voltage applied to the Mo foil.*

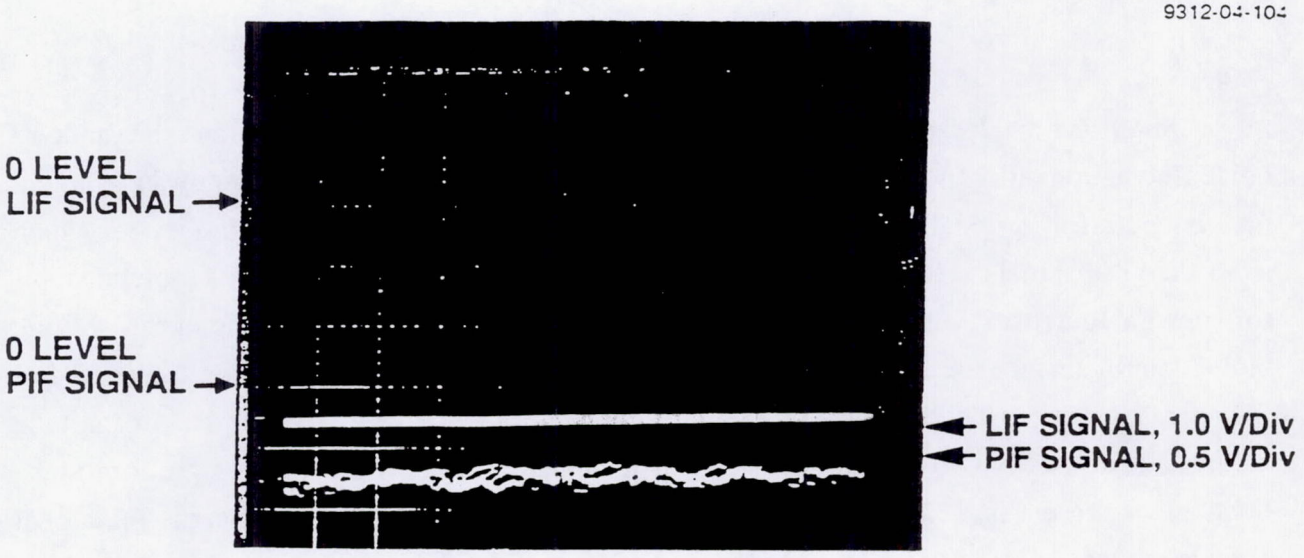

J_E = 20 A
V_D = 29 V
V_{BIAS} = 150 V

Figure 37. LIF and PIF signals at λ = 390.2 nm. *Enhanced-sputtering plasma conditions and with 150-V bias voltage applied to the Mo foil.*

which is probably in the range of 10s of GHz (recall that the laser bandwidth is about 300 GHz), resulting in a fairly noisy LIF signal (even after lock-in detection). The data shown in Figures 35 to 37 were taken with the integration time of the lock-in amplifier set at 3 s. Even at this setting there was a slow (on the order of seconds) drift in the LIF signal, while the dc-coupled output of the photomultiplier remained unchanged. This behavior suggests that drift of the laser frequency is probably the cause of the amplitude drift that we observed. A set of etalons (for UV operation) within the dye-laser cavity were eventually used to reduce its output to a single longitudinal mode with a jitter on the order of 20 MHz. Since this jitter is roughly three orders of magnitude smaller than the width of the molybdenum resonance, a steady LIF output could be achieved.

We explored whether the LIF signal levels detected in this manner have long-term stability and repeatability under conditions that maintained constant discharge-plasma parameters (constant molybdenum sputtering rate). In addition, we explored the sensitivity of the detected LIF signals to changes in molybdenum erosion rates. Using the experimental setup shown in Figure 34, we observed relatively large-amplitude fluctuations (frequency of approximately 10 to 100 Hz) on the apparent LIF signal, which was dependent on the bias voltage applied to the molybdenum foil. We had to use very long (30 to 100 s) integration times on the lock-in amplifier in order to "smooth out" these fluctuations and obtain a stable LIF signal. We attributed the apparent LIF fluctuations to the large PIF signal sensed by the monochromator.

We modified the design of the molybdenum foil to minimize the PIF signal (and the random-noise fluctuations it produces), and to maximize the LIF signal. Figure 38(a) shows the coiled molybdenum foil originally used to demonstrate the LIF wear-diagnostic technique, but which allows the PIF signal to reach the monochromator. Figure 38(b) shows a modified molybdenum-foil design that uses louvers instead of a coil. This improved design also increases the molybdenum surface area, yielding a higher density of sputtered material. The louvered-foil arrangement reduces the PIF signal reaching the monochromator, while increasing the magnitude of the LIF signal. With the louvered-foil arrangement, we verified that the random-noise fluctuations present in the apparent LIF signal were significantly reduced and that the PIF signal was also reduced (by an order of magnitude). We were able to lower the integration time of the lock-in amplifier to 3 s, obtaining stable and repeatable LIF signals.

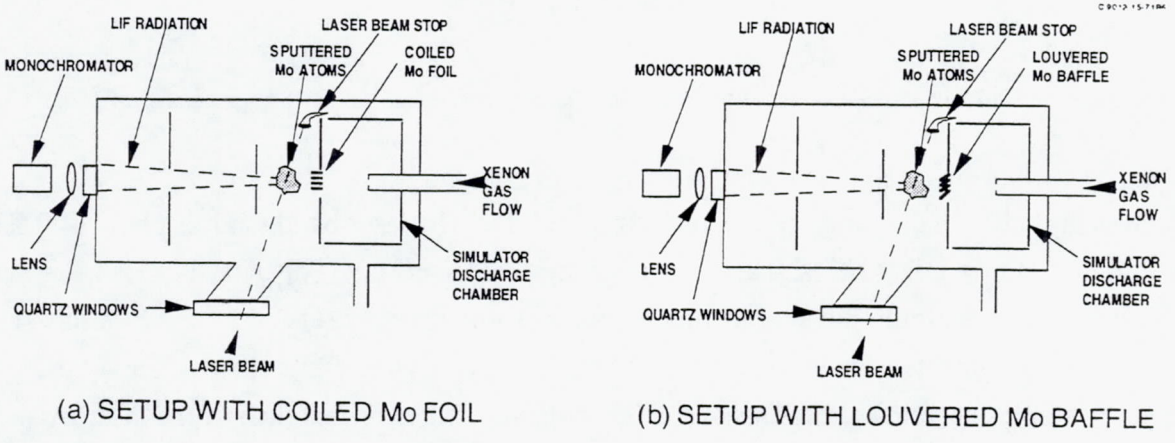

Figure 38. Use of louvered baffle (b) to improve LIF signal strength over the coil (a).

We varied the bias voltage applied to the molybdenum foil and recorded the LIF signal on a strip-chart recorder. Figure 39 shows the temporal behavior of a representative LIF signal, along with various electrical parameters of the discharge-chamber simulator, and the laser-output power. The operating parameters of the discharge-chamber simulator (cathode-emission current, discharge voltage, and cathode flow rate) were maintained constant in order to achieve constant plasma conditions. As shown in Figure 39, the LIF signal is relatively constant over time

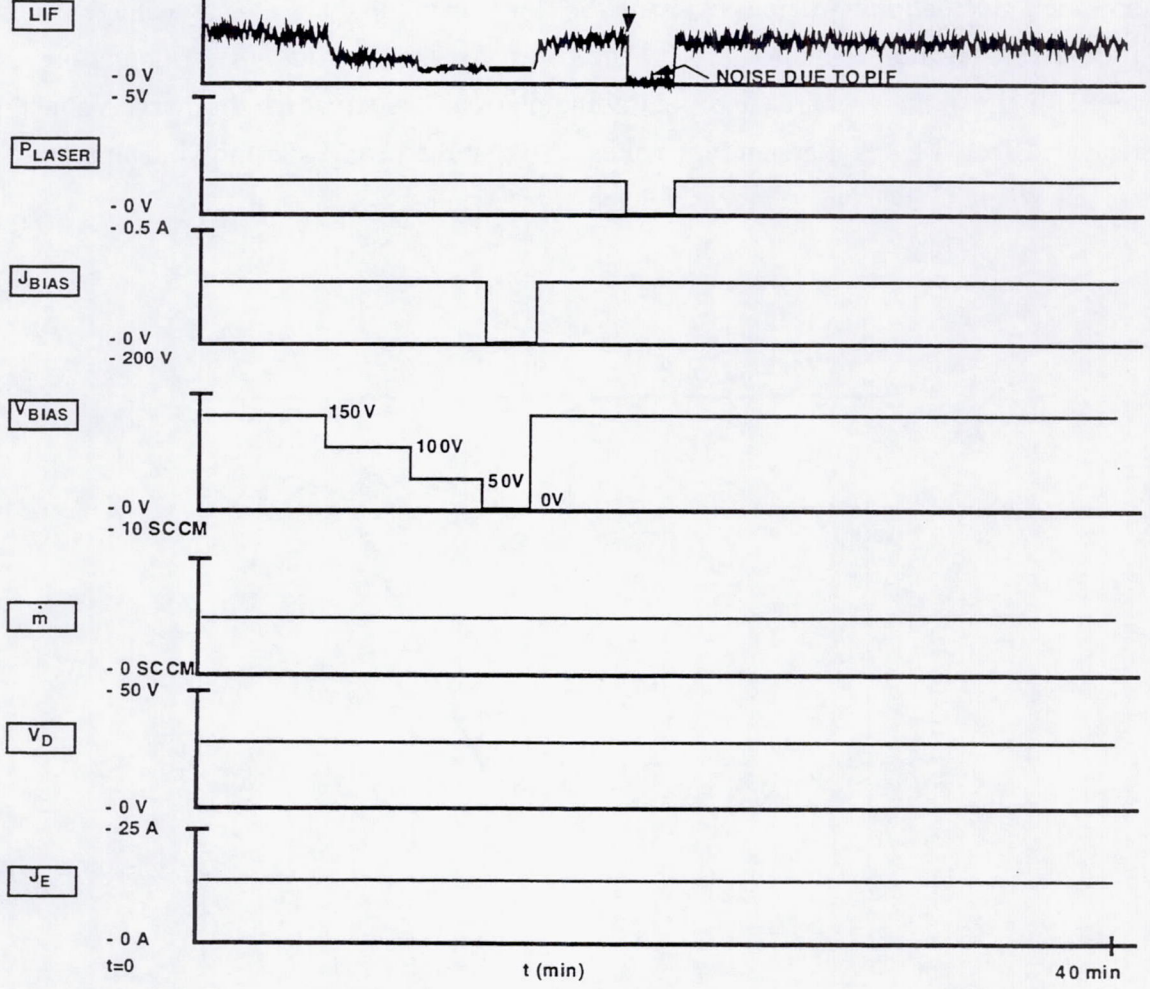

Figure 39. Strip-chart recording of LIF signal, discharge-chamber parameters, and laser-output power.

for fixed bias voltage. As the bias voltage is lowered (to reduce the molybdenum erosion rate), the LIF signal level is reduced as well, indicating that changes in the molybdenum density can indeed be detected (cf., Figure 39 and Figure 40). Decreasing the bias voltage also reduced the random-noise fluctuations, whereas blocking the laser-beam input at full-bias-voltage conditions had little effect on the fluctuations. This indicates that the random-noise fluctuations on the apparent LIF signal are primarily induced by the plasma. Note that the discharge voltage stays constant, unaffected by changes in bias voltage, so that the changes in molybdenum sputtering rate are due solely to the change in bias voltage.

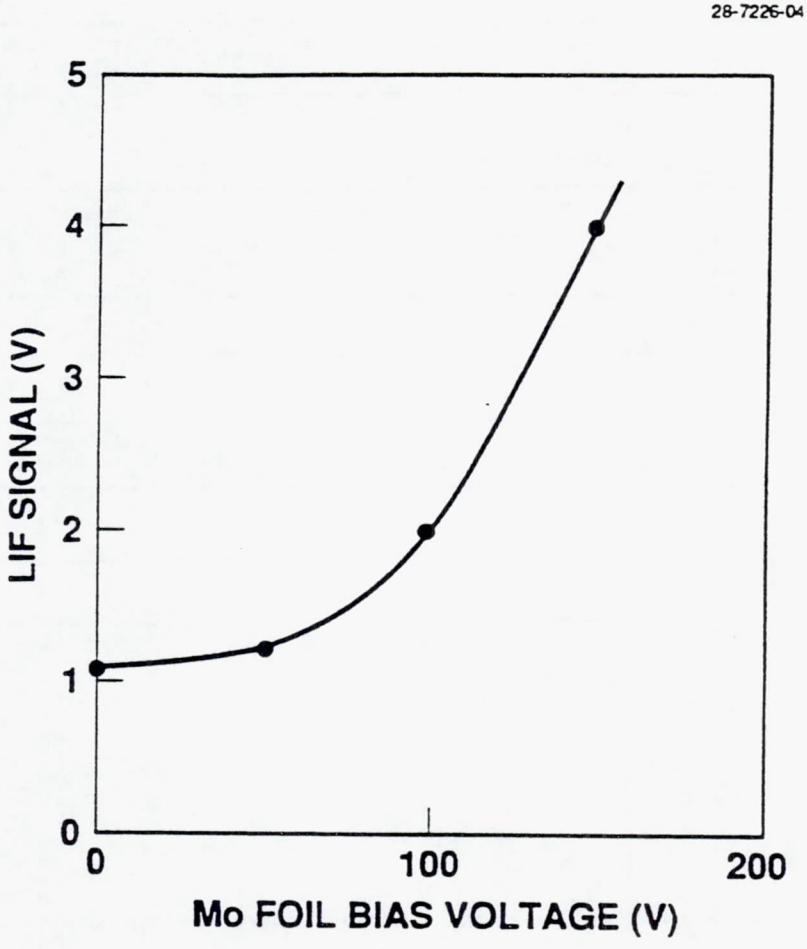

Figure 40. LIF test setup and experimental results.

4.3 THRUSTER MEASUREMENTS

We adapted the laser and monochromator setup shown in Figures 38(a) and 38(b) for demonstrating that LIF could be used to detect molybdenum sputtered from the negative electrode of an operating thruster. Figure 41 shows a schematic diagram of the setup that was used to accomplish this in our 9-ft-diam vacuum chamber. Mirrors were used to direct the laser beam to the top port of the vacuum chamber. The laser beam entered the chamber through a quartz window and traversed the ion beam as indicated in Figure 41. A beam stop located on the vacuum-chamber floor minimized reflection of the laser light within the vacuum chamber. A light-absorbing collimator, which extends from the side port into the vacuum chamber approximately 46 cm, minimized the contribution of reflected laser light to the background LIF signal.

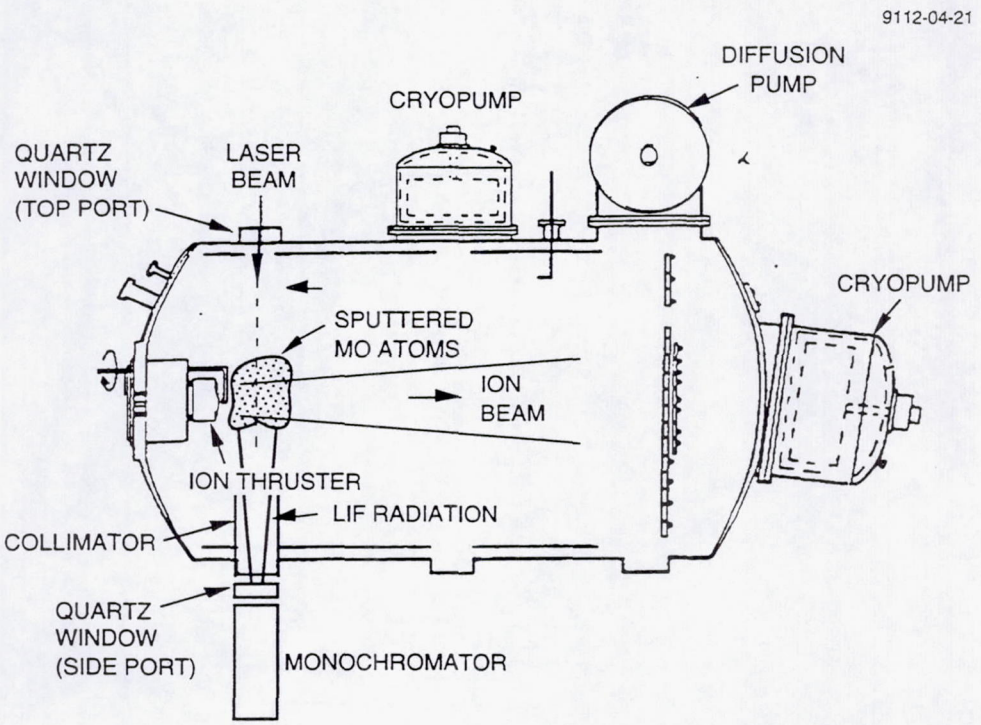

Figure 41. Schematic of "on-line" LIF setup.

LIF radiation produced by the laser beam interacting with sputtered molybdenum in the ion beam was detected using a 3/4-m monochromator, which is positioned at the side port of the 9-ft-diam vacuum chamber (see Figure 42). In this location, the monochromator viewed the ion beam orthogonal to the laser beam, and without any interference caused by radiation from the discharge-chamber plasma.

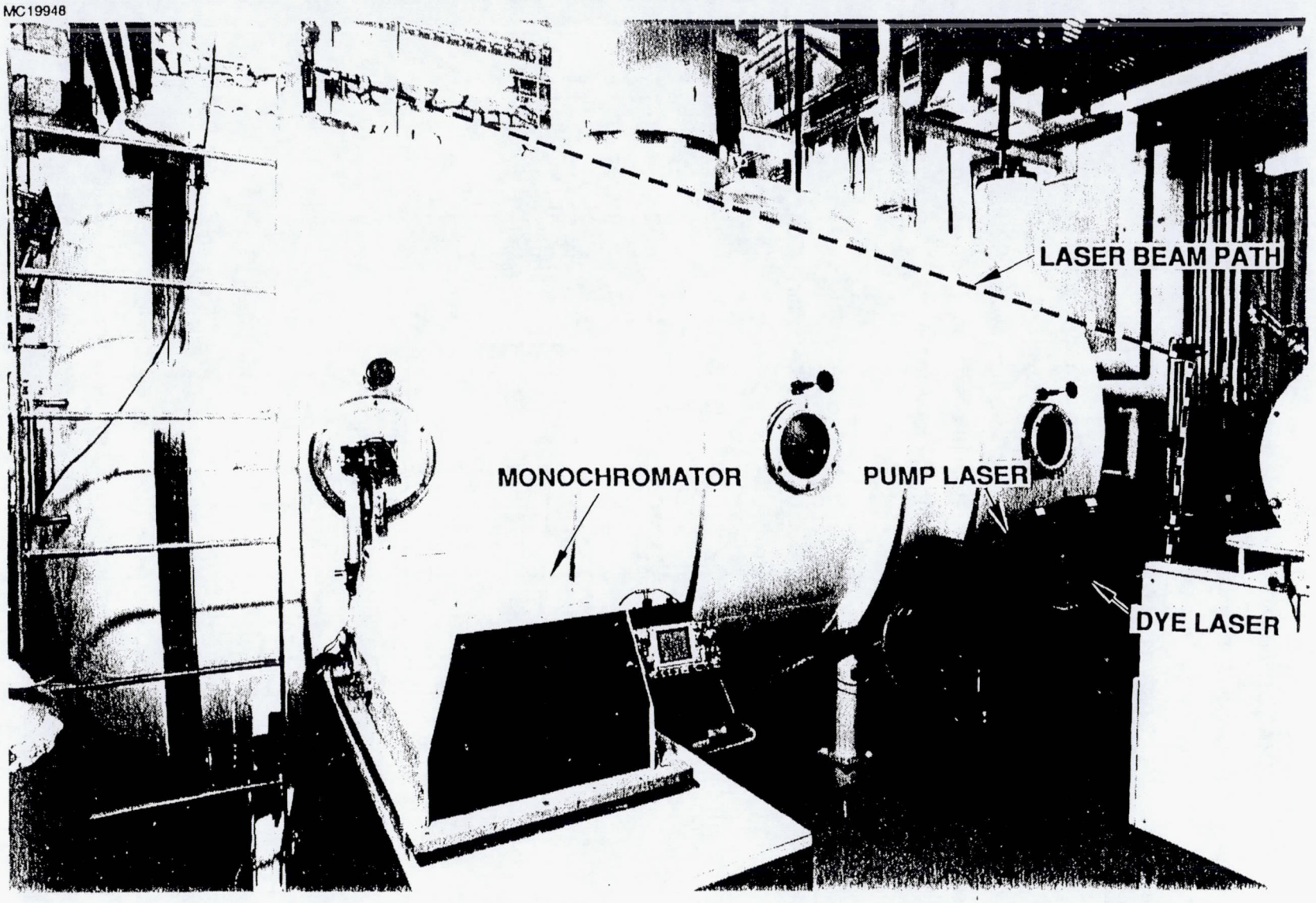

Figure 42. Experimental setup for demonstrating LIF as a diagnostic for measuring accelerator-grid wear.

The output beam of an argon-ion-pumped, standing-wave dye laser was directed through the top port of our 9-ft-diam vacuum chamber using an arrangement of mirrors. The fluorescence signal produced as the light beam passes through molybdenum atoms (which have been sputtered from the accel grid of the thruster under test) was detected by the monochromator. Figure 43 (which was taken from the open end of our 9-ft-diam vacuum chamber) shows the top port and collimator through which the laser beam enters the chamber. A light dump and collimator located in the bottom of the chamber absorbed the laser beam. A collimator that minimizes scattered light from reaching the monochromator is visible in the right of the photo. A movable molybdenum plate served as a reflector to allow laser light, or plasma-induced fluorescence from within the discharge chamber, to reach the monochromator for calibration purposes. The molybdenum plate also served as a strong source of sputtered material, which was used for adjusting both the laser frequency and the monochromator wavelength. The experimental arrangement shown in Figure 43 was found necessary to yield LIF data with good signal-to-noise ratio.

Figure 44 shows LIF-signal measurements (the output of the photomultiplier tube in the monochromator was divided by the measured laser-output power, which drifts slightly) as a function of accelerator-electrode current for two different accelerator voltages. The accel current was increased by introducing xenon into the vacuum chamber from an auxiliary gas source. The LIF signal exhibits the anticipated dependence on accel current (sputtering rate), and the relative increase in the LIF signal with accel voltage is consistent with an increase in sputter yield at higher energy.

Figure 45 shows the LIF signal as a function of accelerator voltage for three different accel currents, with the current variation produced by introducing xenon into the vacuum chamber. The trends are consistent with the dependence of sputtering rate on current density and the dependence of sputter yield on ion energy.

To gain additional physical insight from the data shown in Figure 45, we plotted the variation of sputter yield with accelerator voltage in Figure 46 for one of the curves from Figure 45. The data indicate that the LIF signal and the sputter yield have that same functional dependence on accelerator voltage. The preliminary results of Figures 44, 45, and 46, are believed to adequately demonstrate the validity of LIF as a real-time diagnostic for assessing relative accelerator-grid wear rates in ion thrusters. We believe absolute wear rates could be obtained by calibrating the LIF signal using measured wear rates.

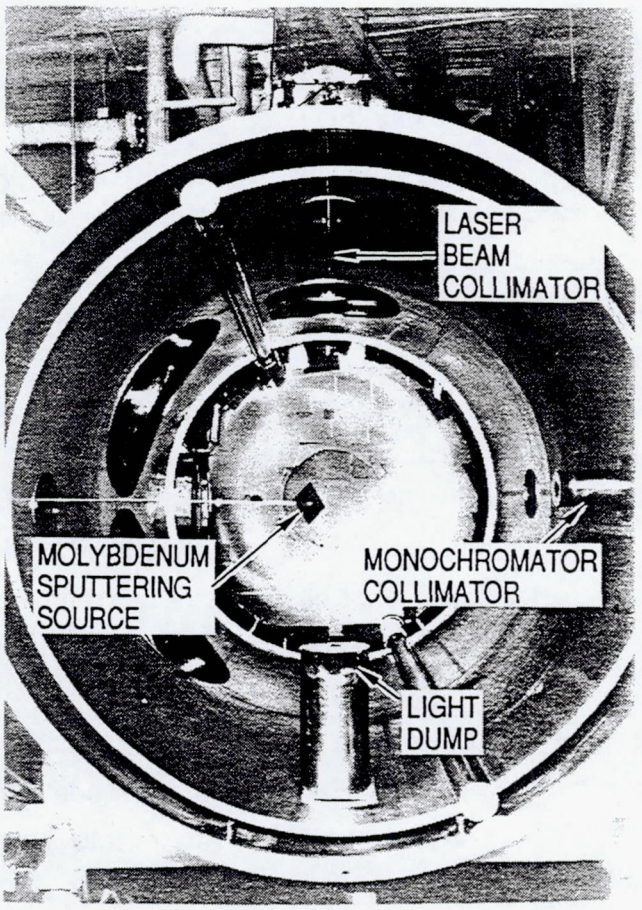

Figure 43. LIF setup in HRL's 9-ft-diam vacuum chamber.

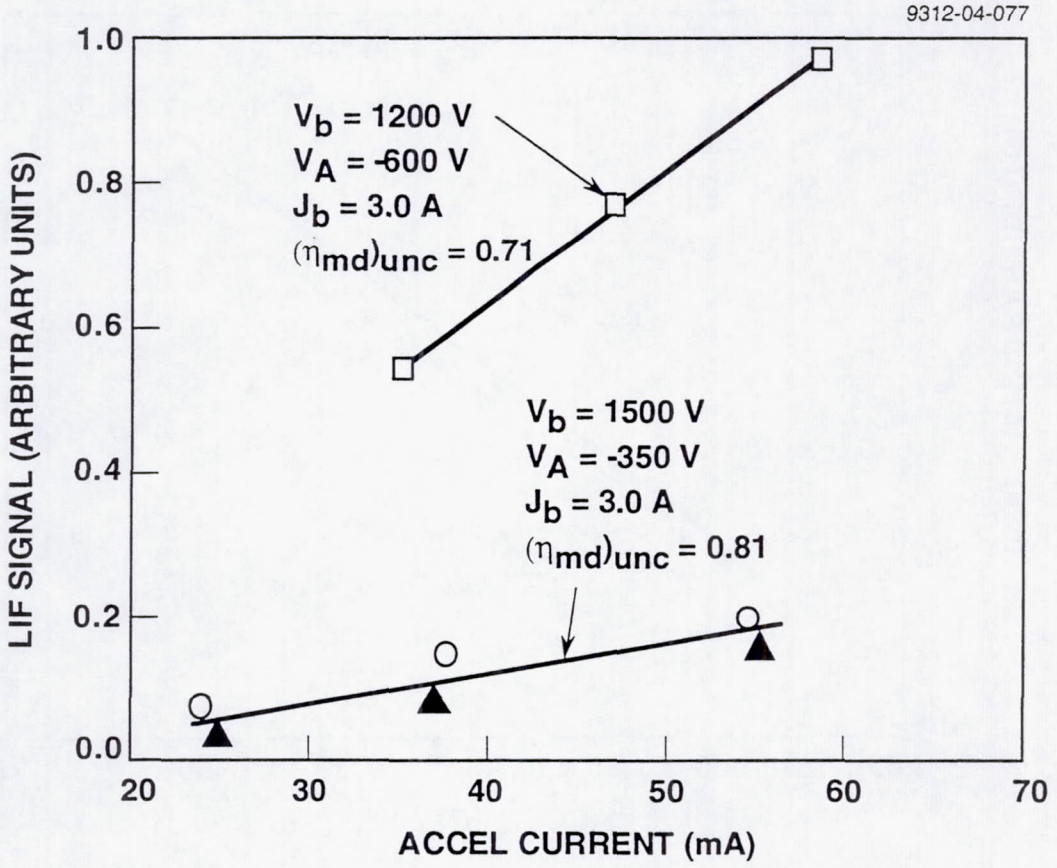

Figure 44. Variation of LIF signal with accelerator current.

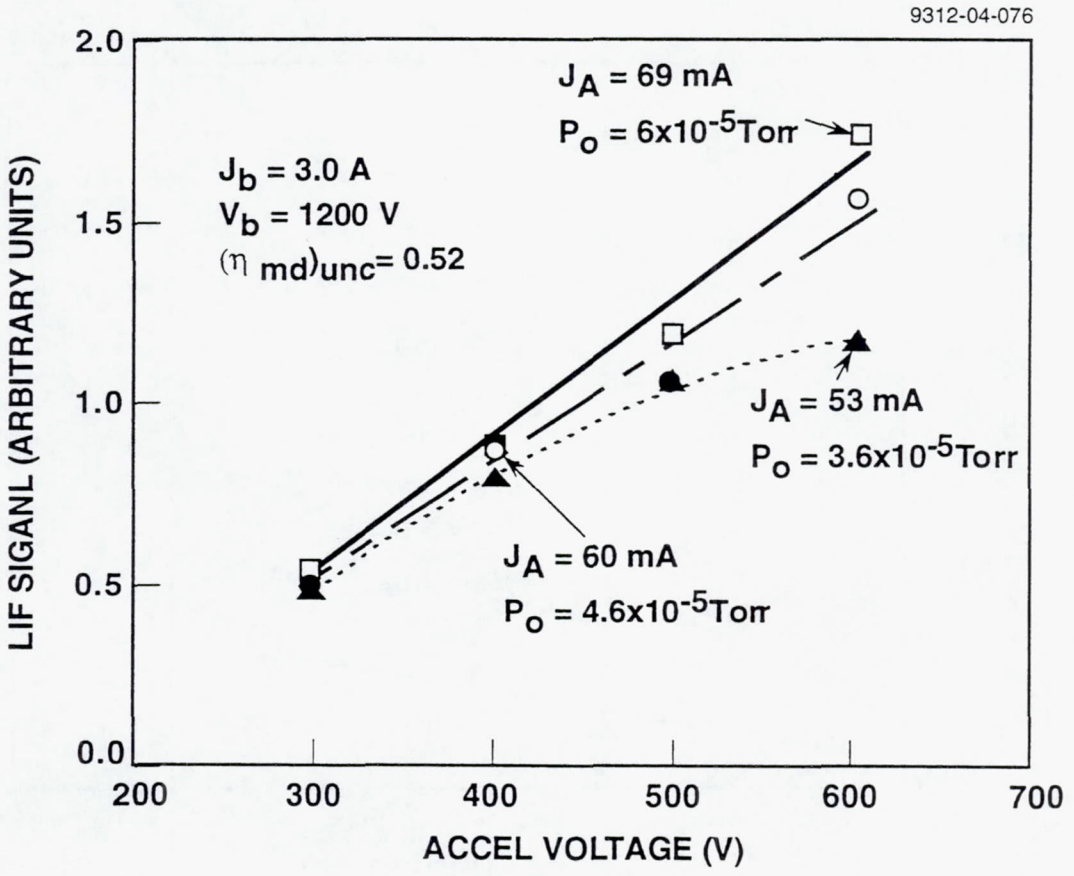

Figure 45. Variation of LIF signal with accelerator voltage.

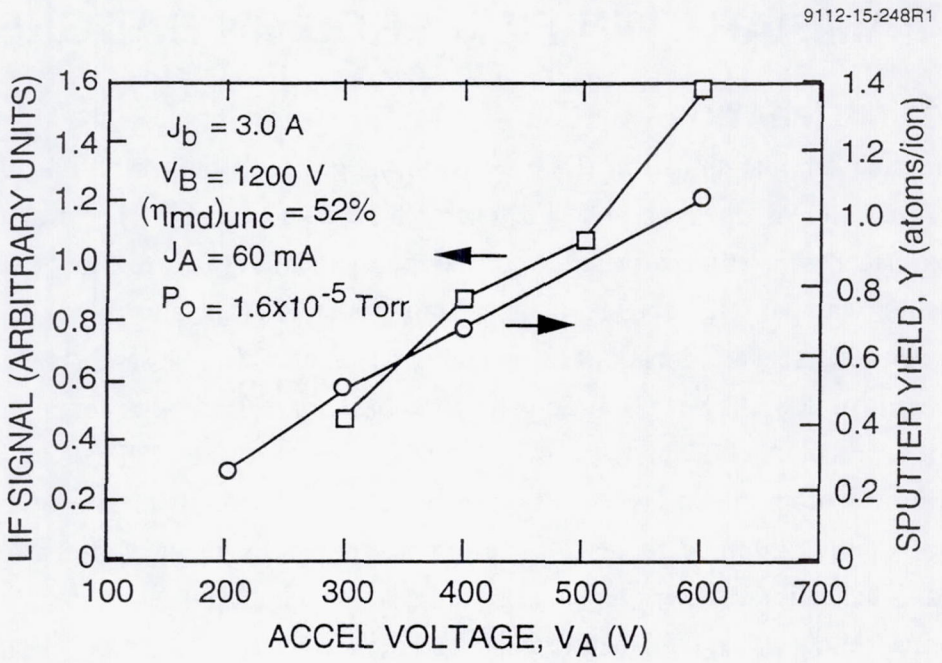

Figure 46. Comparison of LIF signal level and sputter yield behavior as a function of accelerator voltage level.

Section 5
LAMINAR-THIN-FILM EROSION BADGES

5.1 BADGE CALIBRATION

We calibrated laminar-thin-film (LTF) erosion badges with bulk molybdenum, using the calibration setup shown in Figure 47. For each test, a small piece of perforated LTF badge material was placed adjacent to a piece of polished molybdenum (arc-cast, low carbon content). The LTF badge was partially masked using a stainless-steel strip, and the bulk-molybdenum sample was masked in several locations using photoresist material. The samples were exposed to sputtering beams of 300-eV Xe^+, Kr^+, and Ar^+ for a duration sufficient to remove several of the molybdenum layers on the LTF badges. After the beam exposure, the LTF mask was removed to permit the number of sputtered layers to be counted. The photoresist mask was removed from the bulk-molybdenum sample to permit the erosion depth to be measured using a surface profilometer. This calibration was repeated on at least one additional set of samples to establish the level of uncertainty in the LTF measurement technique.

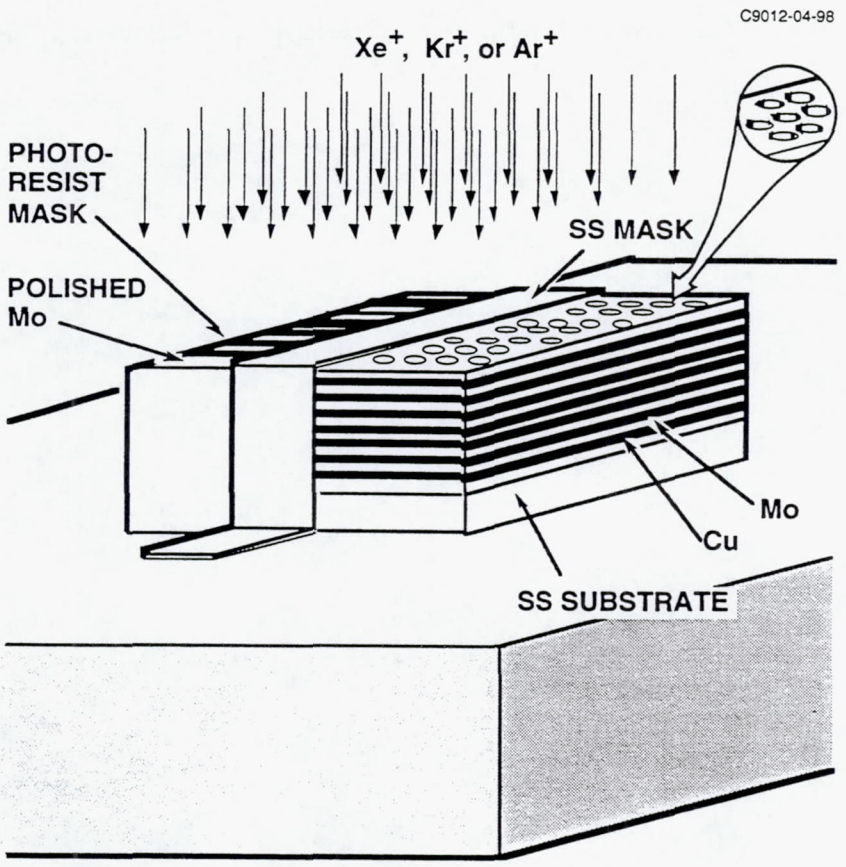

Figure 47. Schematic illustrating technique for calibrating LTF erosion badge with bulk Mo.

After exposing the samples to a monoenergetic flux of the test ions for a specified period of time, the samples were removed for diagnostic analysis. The LTF badges were examined under a microscope to determine the number of molybdenum layers that had been removed through ion sputtering, and this determination was subsequently confirmed by performing a diagnostic etch to reveal the remaining layers. In determining the total erosion depth, the Cu layers were treated as equivalent, partial-thickness layers of the 600-Å-thick molybdenum layers. The fractional layer thickness, k, was calculated as $k = (Y_{Mo}/Y_{Cu})(n_{Cu}/n_{Mo})$, where Y is the sputter yield and n is the number density. For 300-eV Ar^+ and Xe^+, the numerical value of the fractional layer thickness was determined to be $k = 0.45$, based on published sputter yields and material densities. In other words, the copper layers were treated as equivalent molybdenum layers having a reduced thickness of $0.45 \times 600 = 270$ Å.

The bulk-molybdenum erosion rates were determined by chemically removing the photoresist mask and then measuring the surface features with a profilometer. Figure 48 shows a typical measurement result, displaying flat peaks and valleys of relatively uniform height.

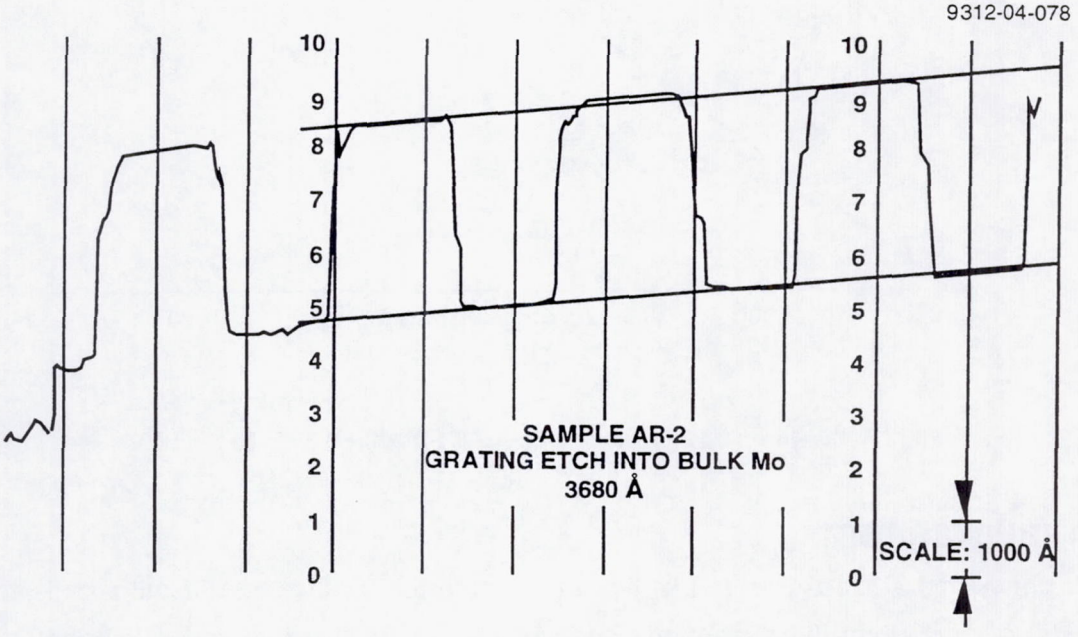

Figure 48. Surface-profilometer measurement of sputter-etch pattern on bulk-Mo calibration sample.

Calibration results are shown in Figure 49, with the bulk-molybdenum results plotted versus the LTF results, and with perfect correlation indicated by the straight line. The uncertainties in the measurement techniques are indicated by the error bars, where we used 250- and 600-Å as the uncertainty in the direct-measurement and layer-counting technique, respectively. Although most of the calibration data fall on, or near, the straight line, some of the results (particularly the data obtained with Xe^+) depart from perfect correlation by more than the indicated error bars.

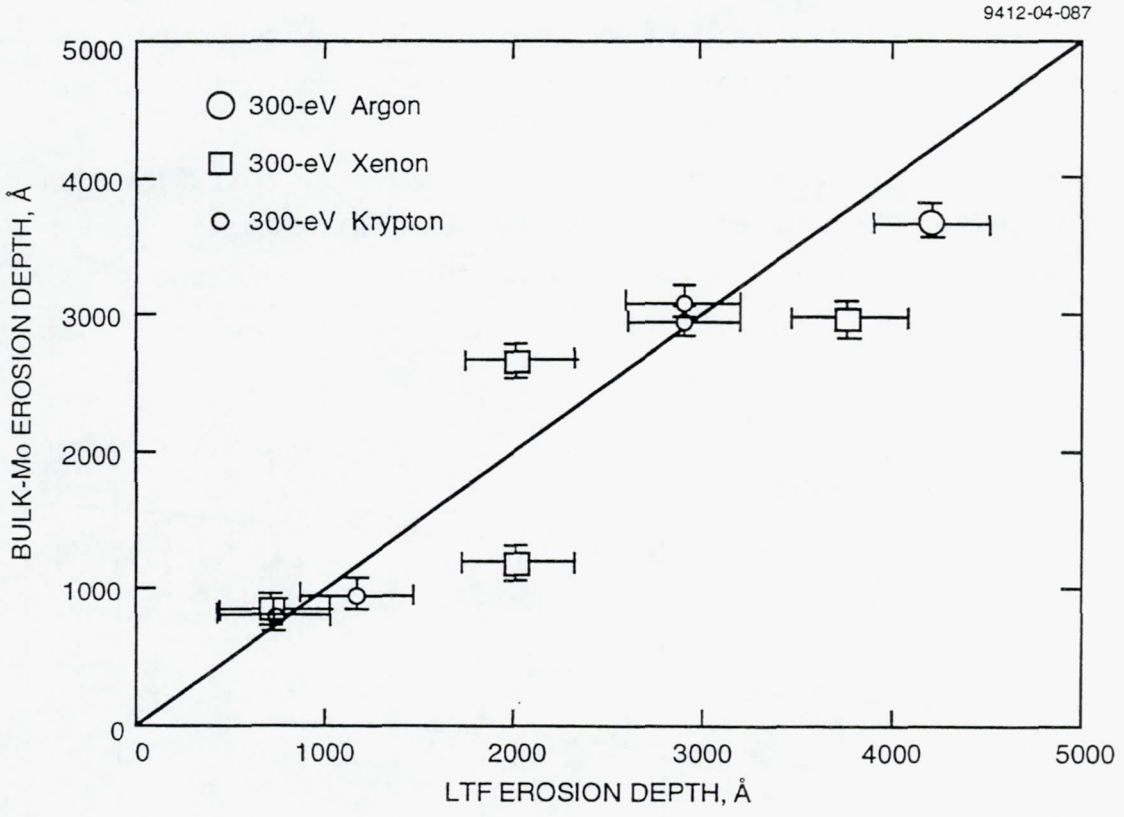

Figure 49. Bulk-Mo vs. LTF erosion-rate results for 300-eV Ar^+, Kr^+, and Xe^+ ions.

5.2 THRUSTER TEST

We conducted a short-term (≈1 h) test to measure the erosion rate of the accel and screen electrodes of our 30-cm-diam lab-model thruster using LTF erosion badges. The intent was to correlate these results with those obtained during the 900-hr test conducted at NASA - LeRC. A six-hour badge test was estimated to be sufficient to provide measurable erosion rates, based on the accel current and voltage measured during the LeRC test.

Erosion badges having dimensions of approximately 13-mm by 13-mm were spot-welded to the downstream surface of the accel electrode and the upstream surface of the screen electrode.

Figures 50 and 51 are photographs showing the locations of the badges on the accel and screen grids, respectively. A total of eight LTF badges were mounted on the accel grid and two LTF badges were mounted on the screen grid.

We operated the 30-cm-diam lab-model thruster at conditions that closely simulate those representative of the LeRC life test. Table 8 compares the critical thruster and facility conditions of our short-term test with those of the LeRC test. The accel current and voltage are the most critical parameters to match in order to simulate the same charge-exchange-ion erosion conditions of the accel electrode. Table 8 indicates that all thruster parameters were duplicated except for the discharge voltage, which was adjusted to achieve the desired accel current at the indicated vacuum-chamber pressure.

Figure 52 shows photographs of the erosion badges after removal from the accel electrode. The badge that was mounted at the 3/4-radius location is not included in the photo because it had not been eroded enough to expose a copper line. The photographs clearly show the copper-line patterns resulting from charge-exchange-ion erosion of the webbing between apertures of the accel electrode. The erosion rates were determined from these patterns by counting the number of copper lines remaining after the exposure.

Figure 53 is a plot of the LTF-badge wear rates obtained from analyzing the photographs at the "triangular-pit" regions where the erosion rates are the highest. For comparison, results of the accel-electrode erosion measured at the completion of LeRC's 900-h life test are also presented. The results presented in Figure 53 indicate that the erosion-badge wear rate has a peaked profile. There is also good agreement between the LTF-badge results and the LeRC life test results, at least for the centerline location.

The peaked behavior of the erosion-badge wear rates is consistent with operation of the thruster at high propellant-utilization efficiency. For the ring-cusp thruster, the ion-production region (and, therefore, the ion-beam profile) becomes increasingly peaked on centerline as the propellant-utilization efficiency is increased. The charge-exchange-ion production rate is directly proportional to the product of ion-beam density and neutral density. Assuming a constant neutral density across the diameter of the ion beam, the charge-exchange-ion erosion profile is expected to have very nearly the same peaked profile as the ion-beam-density profile.

Table 11 compares the operating conditions during the erosion-badge test with those of the 900-h life test. Although the beam current, J_b, accel voltage, V_A, discharge voltage, V_D, and discharge propellant-utilization efficiency, $(\eta_{md})_{unc}$, were matched to the NASA-LeRC life test values, the accel current in the erosion-badge test was about 40% higher than it was in the life test. The duration of the erosion-badge test was 1 hour, which was sufficient to allow erosion patterns to be visible on the badges, but without eroding through all the layers.

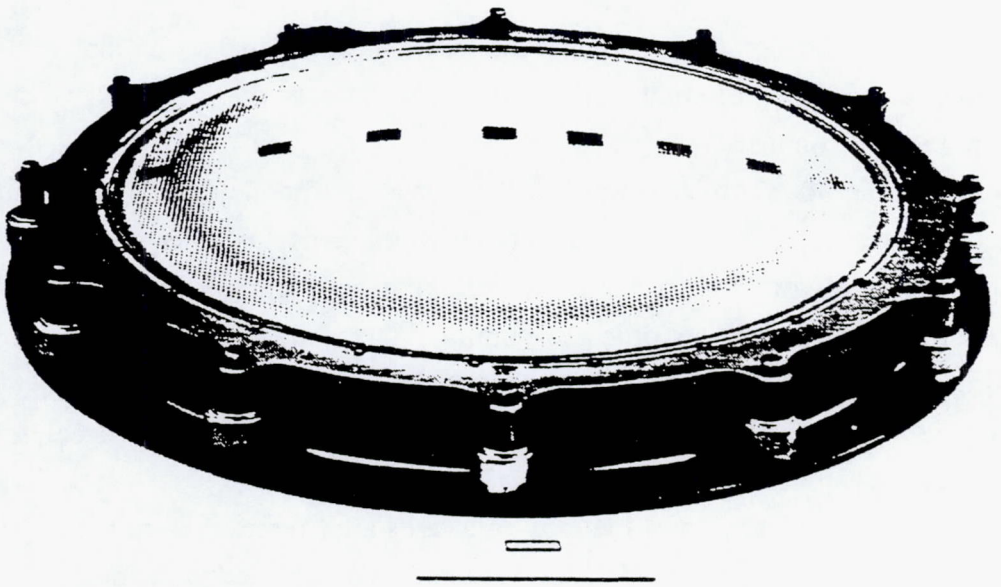

Figure 50. LTF erosion-badge installation on accel grid.

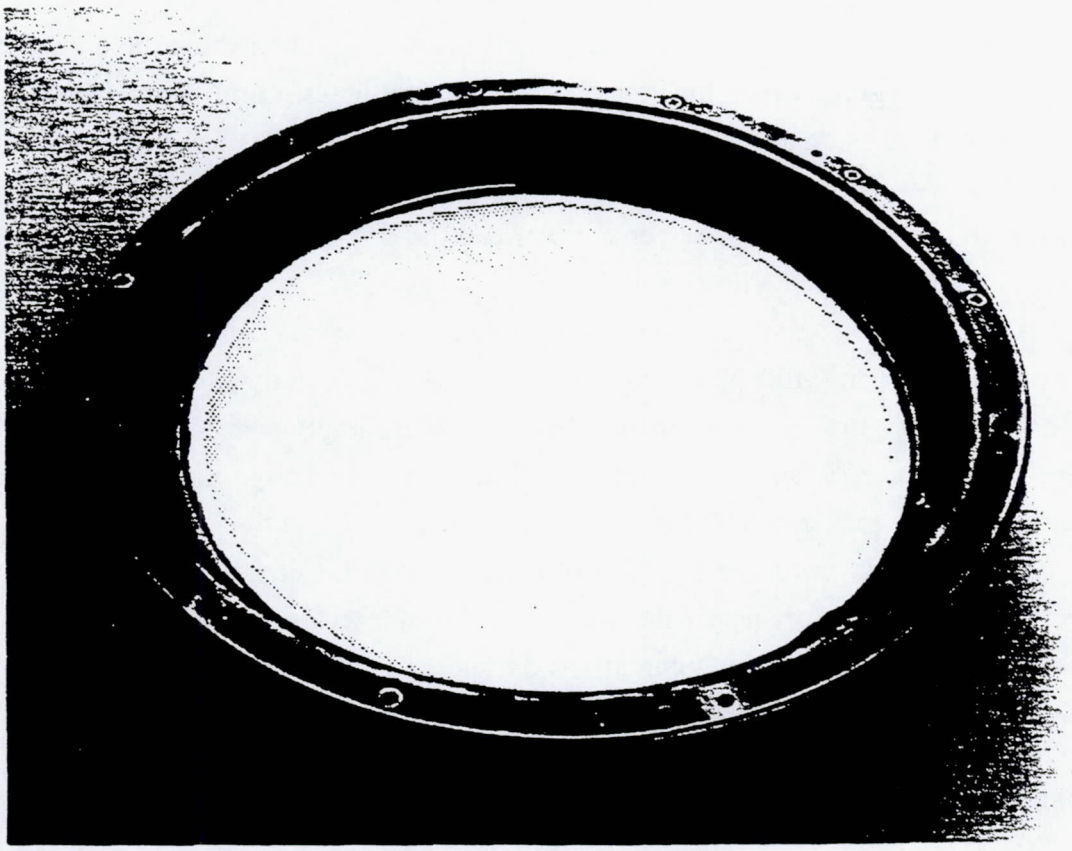

Figure 51. LTF erosion-badge installation on screen grid.

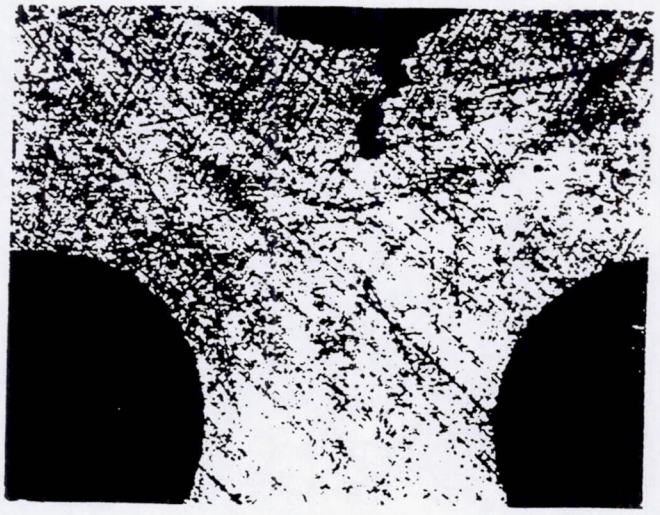

(a)

$\frac{r}{r_B} = 0$

6 Cu LINES VISIBLE

(b)

$\frac{r}{r_B} = 1/4$

3 Cu LINES VISIBLE

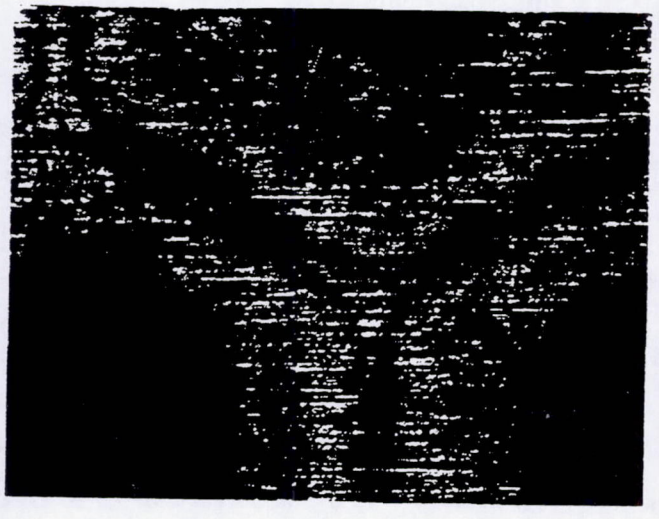

(c)

$\frac{r}{r_B} = 1/2$

1 Cu LINE VISIBLE

Figure 52. Photos of LTF erosion badges.

Table 11. Comparison of Thruster Operating Conditions for Erosion-Badge Test and 900-h Lifetest

Parameter	Erosion Badge Test	900-h NASA Test
V_A (V)	–331	–331
J_A (mA)	25.3	17.4
J_b (A)	3.19	3.19
V_D (V)	27.4	26.9
J_D (A)	22.0	22.0
V_T (V)	1517	1517
V_{nk} (V)	17.8	17.8
J_{nk} (A)	2.0	2.5-3
$[\eta_{md}]_{unc}$ (%)	95.9	95.3
P_T (Torr)	6×10^{-6}	1.3×10^{-5}
Test Duration (h)	1.0	900

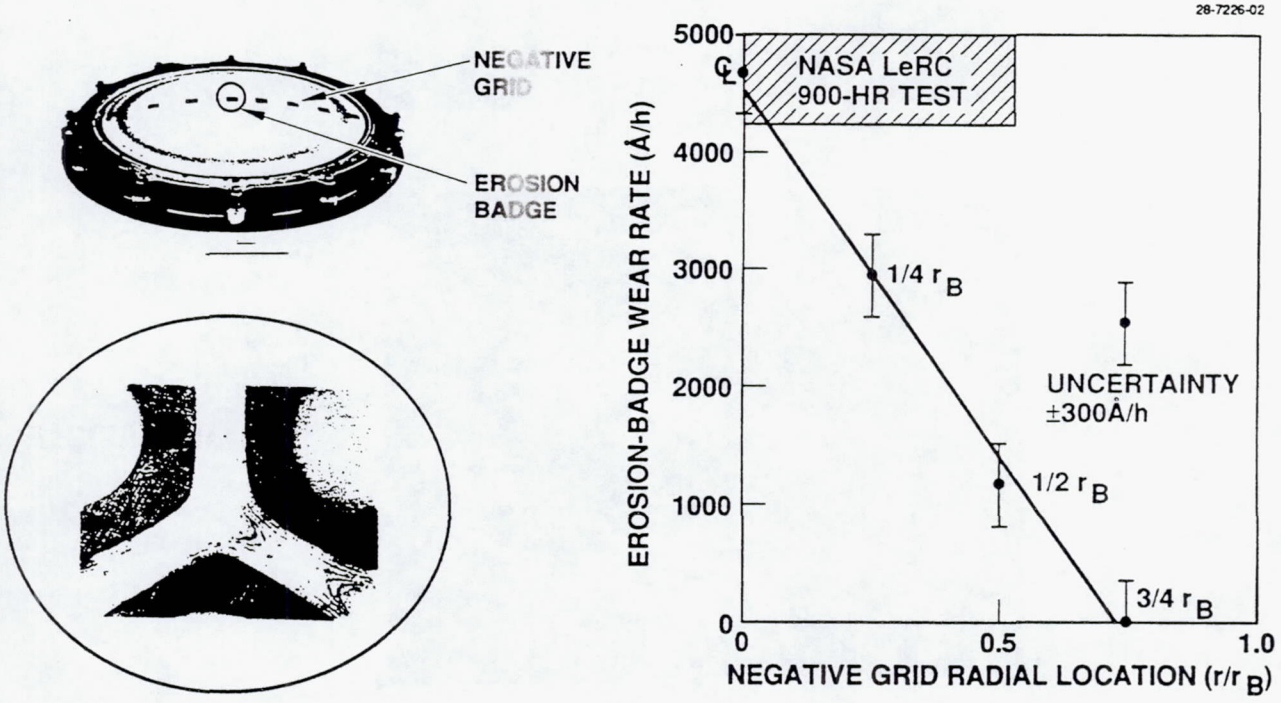

Figure 53. Accel-electrode erosion rates at the "trianglar pit".

Section 6
FACILITY EFFECTS

6.1 PUMPING SPEED MEASUREMENTS

We evaluated the pumping speed of the Hughes vacuum chamber for the inert gases xenon, krypton, and argon. Figure 54 shows chamber pressure measured at the location indicated in Figure 1 (obtained by subtracting the baseline pressure of about 2.5×10^{-7} Torr from the indicated pressure and dividing the result by the ionization-gauge sensitivity for xenon of 2.5) as a function of flow rate expressed in Torr-liters/s. Both the chamber pressure and flow rate were measured using instruments that were calibrated in the Hughes Primary Standards Laboratory against reference values that are traceable to NBS standards. Our flow meters are calibrated on xenon, and our ionization gauge is calibrated on N_2. The highly repeatable data shown in Figure 54 were obtained on separate occasions (four days apart).

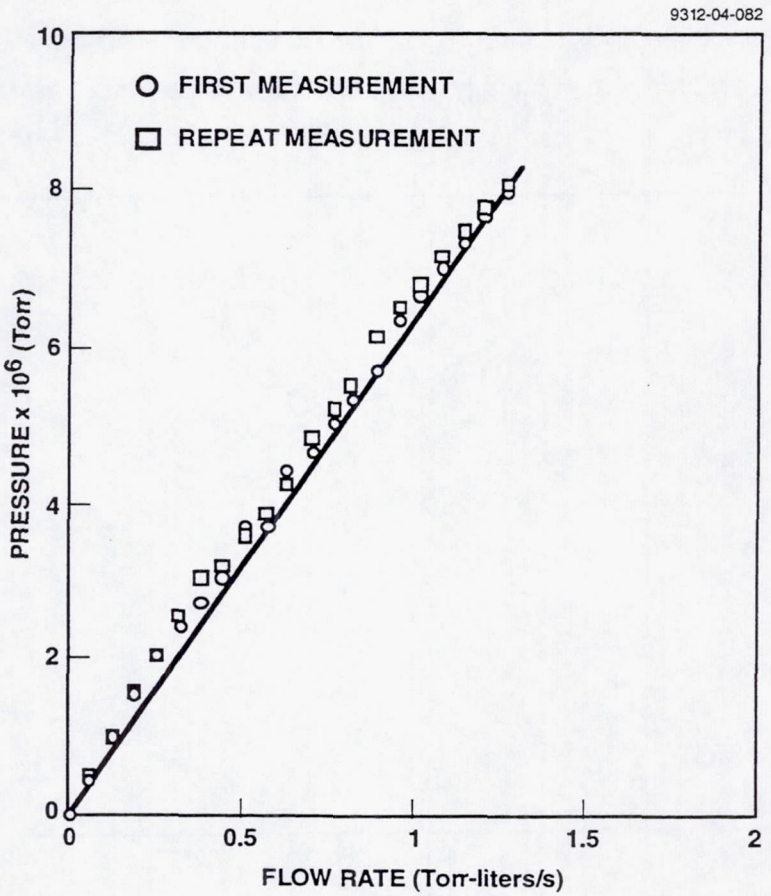

Figure 54. Vacuum-chamber pressure as a function of xenon flow rate, showing repeatability of measurements taken several days apart.

We used the flow-meter constants[9] listed in Table 12 to convert the indicated readings when testing with krypton and argon gases, (i.e., we multiplied the indicated readings by the factor 1.43/1.37 to convert to argon flow rates). The indicated pressures were converted to the appropriate gas pressures by subtracting the baseline pressure (typically 2×10^{-7} to 3×10^{-7} Torr) and dividing the result by the appropriate ionization-gauge sensitivity.[10] The ionization-gauge sensitivities listed in Table 12 were obtained by averaging the values tabulated in the manual for our ionization-gauge controller.[10]

Table 12. Instrument Sensitivities

Gas	Flow Meter Constant	Ion Gauge Sensitivity
Xenon	1.37	2.50
Krypton	1.39	1.77
Argon	1.43	1.12

Figures 55 to 57 present pressure vs. flow rate for the three test gases, showing a high degree of linearity. The pumping speeds obtained from the slope of these curves are listed in Table 13, showing the expected increase in pumping speed realized with the lighter gases.

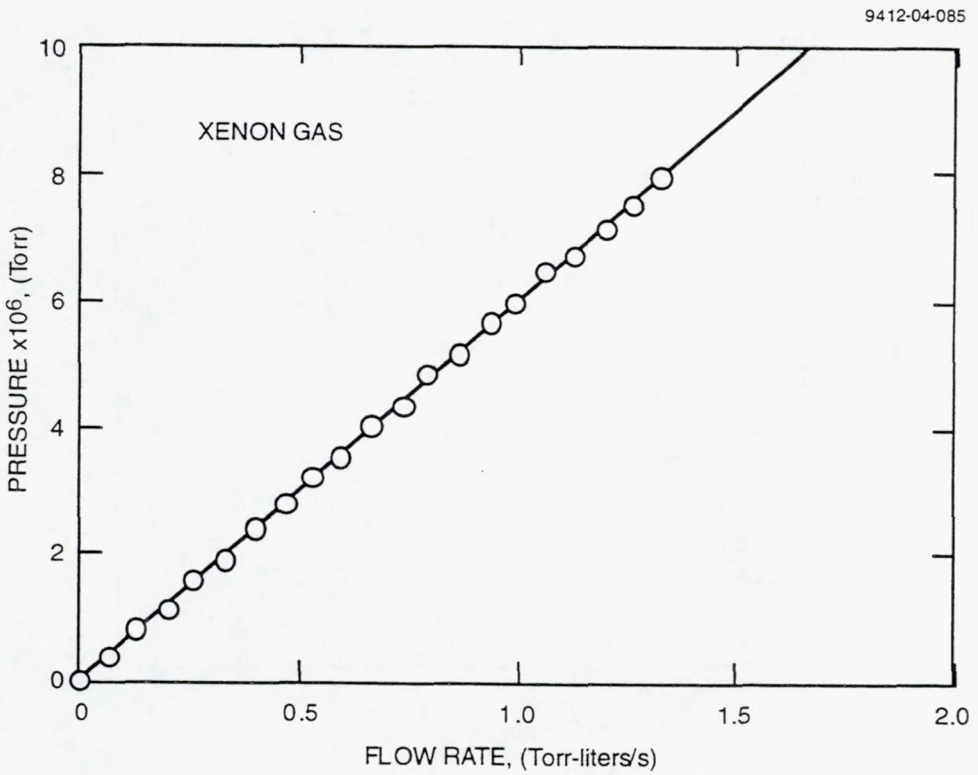

Figure 55. Curve fit of chamber pressure vs. Xe flow rate; reciprocal of the slope establishes pumping speed as 135,000 liters/s.

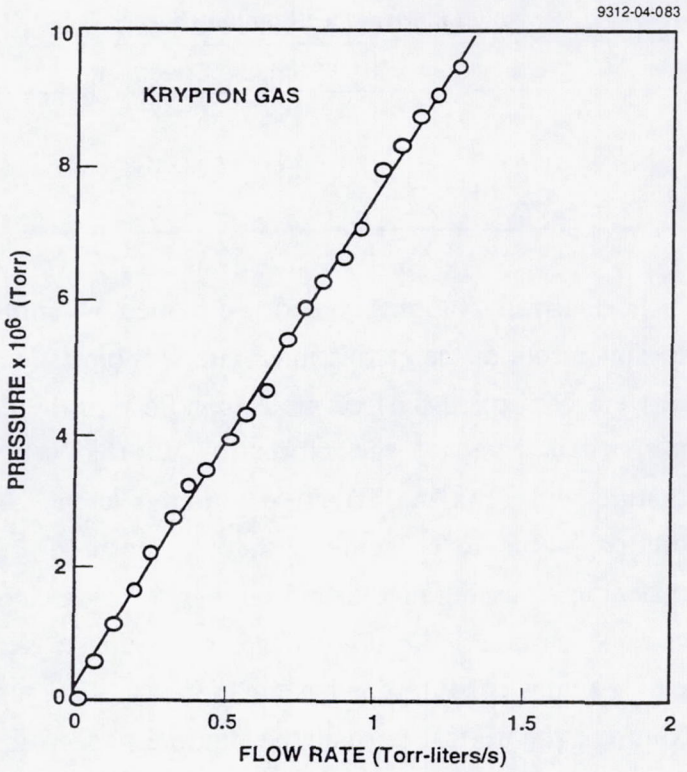

Figure 56. Curve fit of chamber pressure vs. Kr flow rate; reciprocal of the slope establishes pumping at 153,000 liters/s.

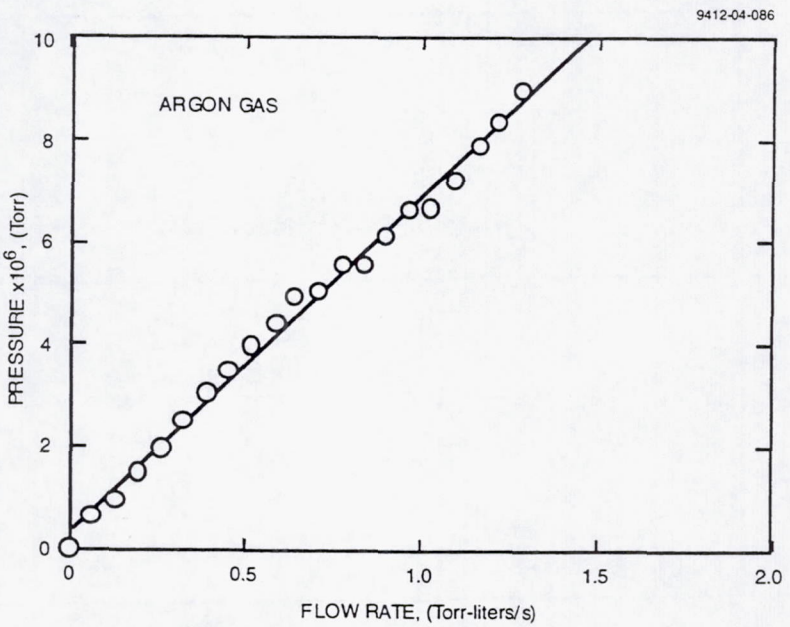

Figure 57. Curve fit of chamber pressure vs. Ar flow rate; reciprocal of the slope establishes pumping speed as 167,000 liters/s.

Table 13. Measured Pumping Speeds

Gas	Pumping Speed (liters/s)
Xenon	135,000
Krypton	153,000
Argon	167,000

Figure 58 shows "normalized pumping speed" (obtained by multiplying the measured pumping speed by the square root of the atomic mass number) plotted versus the mass number. If the pumping speed were controlled by free-molecular flow to the cryotub inlets, then the normalized pumping speed is given by the expression $S = (8kT/\pi)^{1/2}A/4$, where T is the chamber-wall temperature and A is the effective pumping area. In Figure 58, we have normalized the theoretical value to coincide with the measured value for xenon. (The normalization is equivalent to assuming that the effective pumping area of our cryotubs is about 59% of their geometrical open area.) We normalized the results to xenon because it has the lowest vapor pressure of the three gases (argon has the highest). The reason for the departure of krypton and argon from the theoretical normalized pumping speed is not known; since the departure is greatest for argon, one can speculate that it may be due to the vapor-pressure effect. Ion gauge sensitivities for argon, for example, have been reported to vary by as much as 25%, depending on the gauge, and this could also contribute to a large uncertainty in pumping speed.

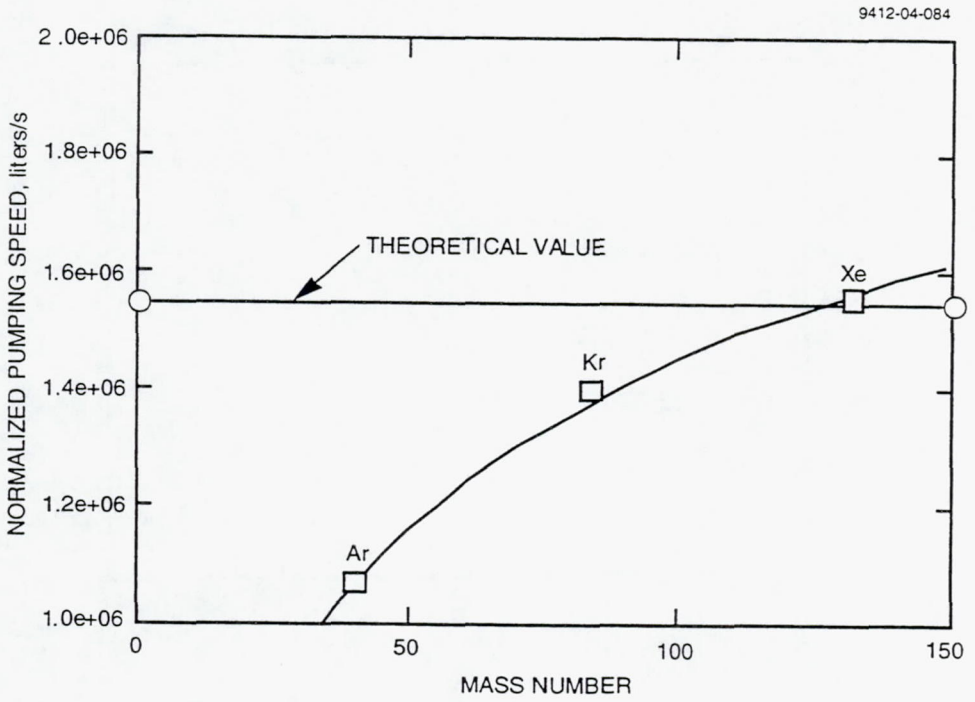

Figure 58. Normalized pumping speed obtained for Xe, Kr, and Ar compared with theoretical value.

6.2 FACILITY-PRESSURE EFFECTS

We evaluated the effect of facility pressure on the accelerator-electrode current of our 30-cm-diam lab-model thruster equipped with ion optics S/N 917 geometry summarized in Table 14. Xenon was introduced into the vacuum chamber through a leak valve, while adjusting the thruster flow rates to maintain the discharge propellant utilization constant. Figure 59 shows the resultant variation in accel current for two different values of discharge voltage.

We explored the effect of facility pressure on accelerator-electrode current, taking advantage of the increased pumping speed (achieved by installing two additional 1.2-m-diam cryotubes) of our 9-ft-diam vacuum chamber to explore a facility-pressure regime that was previously unattainable at Hughes. Figure 60 shows the variation of accel current with vacuum-chamber pressure for the 8-cm thruster S/N 907 operated on xenon. For these tests, the increase in facility pressure was achieved by introducing xenon directly into the vacuum chamber from an auxiliary supply tank.

When the accel current is plotted versus the log of chamber pressure, as in Figure 60, the accel-current behavior changes from one that appears to be relatively independent of chamber pressure (neutral-loss-rate dominated) to one that is strongly dependent on chamber pressure (facility dominated).

Figure 61 compares the variation of accel current with facility pressure for the 30-cm lab-model thruster operated at a beam current of $J_b = 3.2$ A. For both curves of Figure 61, the discharge voltage and the discharge propellant-utilization efficiency are constant. For thruster operation at a beam current of $J_b = 3.2$ A, the accel current appears to be facility dominated, even at the minimum (baseline) facility pressure that we could achieve.

The data presented in Figure 62 were obtained in our 9-ft-diam vacuum chamber with the increased pumping capability that was described earlier. Figure 62 compares the variation in accel current with facility pressure before and after the facility was modified, showing the dramatic reduction in accel current that is realized under the lower pressure conditions of the modified facility. Although the increased pumping speed of our upgraded test facility results in nearly a factor-of-three reduction in accel current, the accel current at the baseline pressure still appears to be facility dominated at this level of beam current.

Table 14. Summary of S/N 917 Grid Parameters.

Parameter	Screen Grid	Accel Grid
Aperture Diameter, mm	1.91	1.14
Thickness, mm	0.25	0.38
Hole Spacing, mm	2.20	2.21
Open Area, %	67.8	24.3
Aperture Geometry	Round	Round

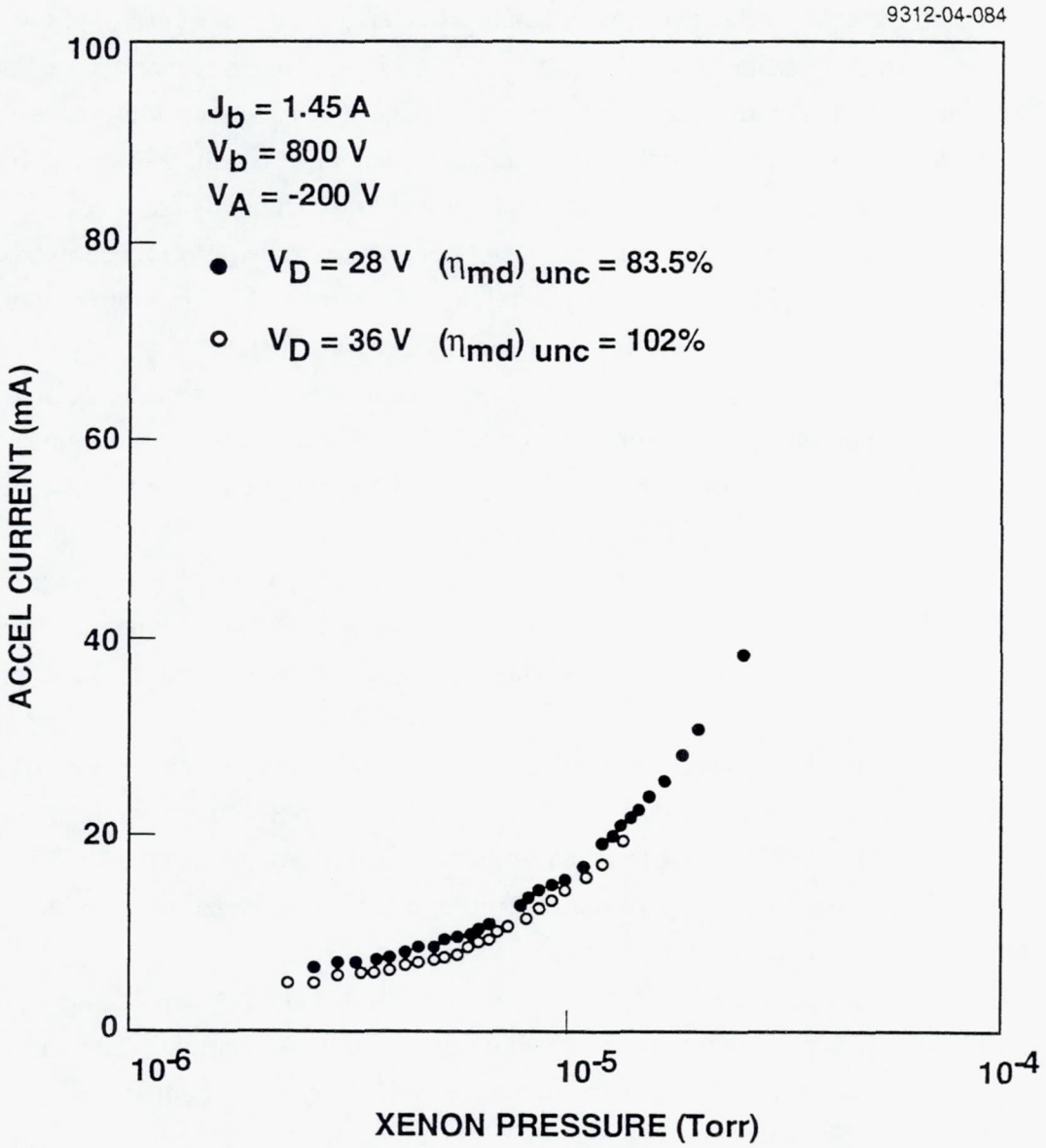

Figure 59. Effect of vacuum-chamber pressure on accelerator-electrode current (Hughes 30-cm-diam lab-model thruster).

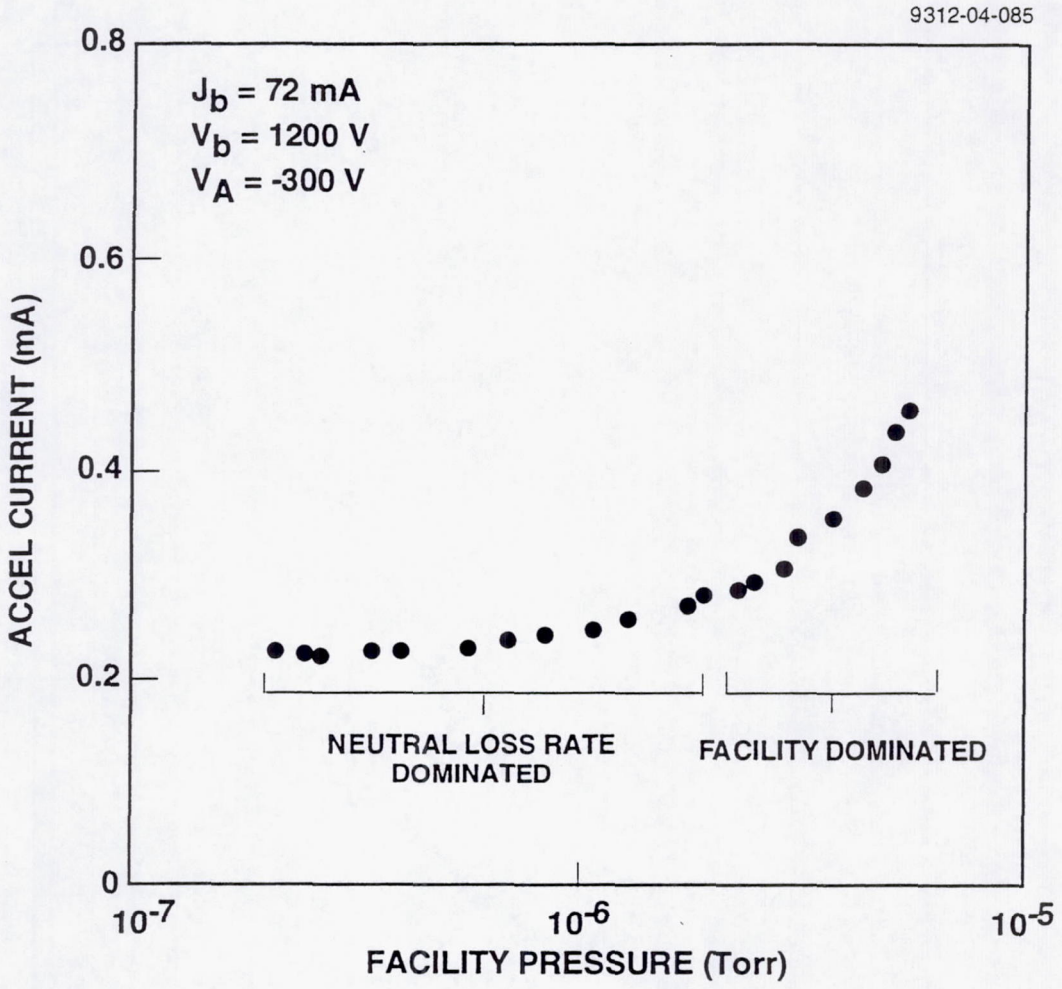

Figure 60. Effect of vacuum-chamber pressure on accel current (8-cm-diam thruster S/N 907).

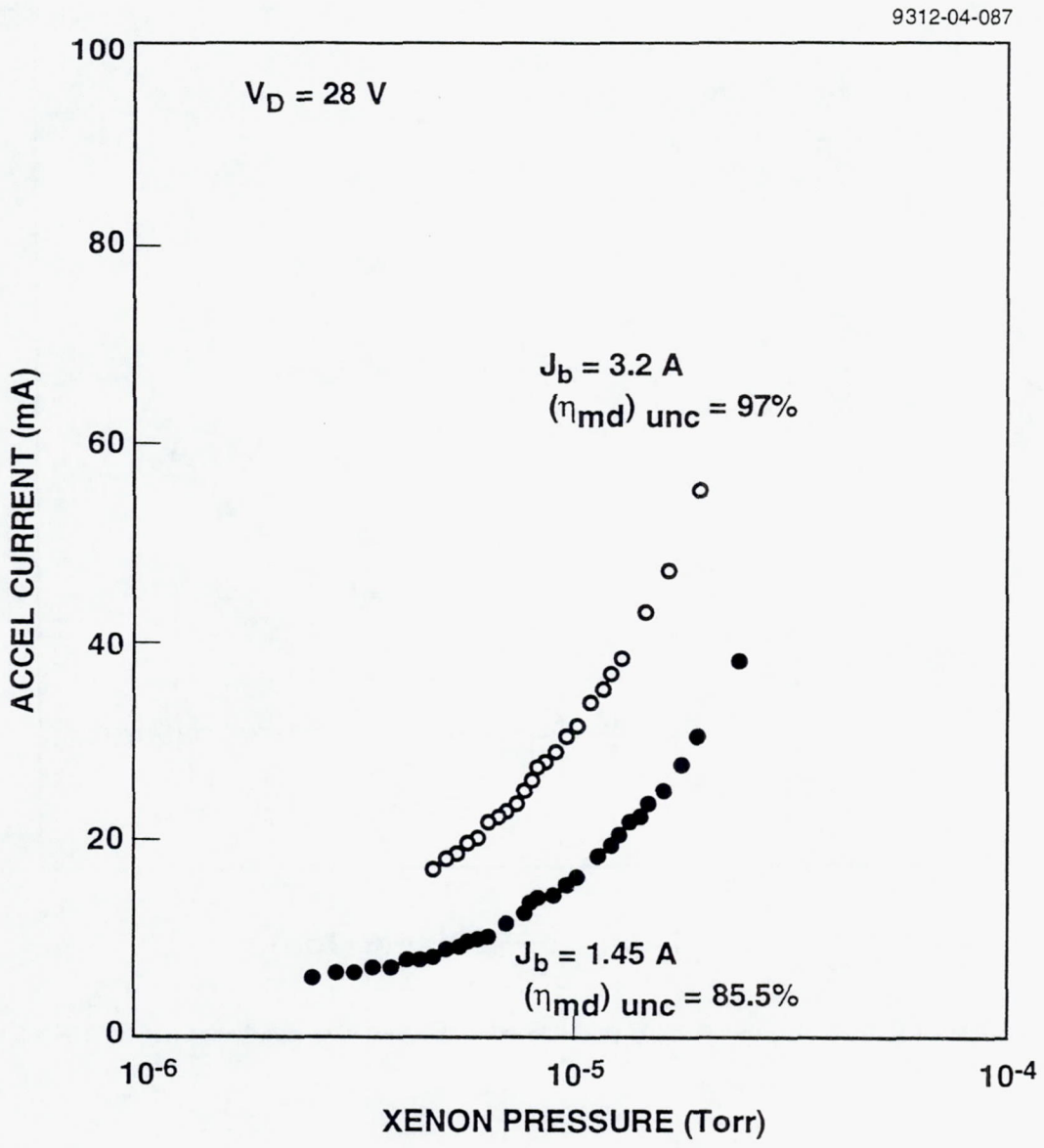

Figure 61. Effect of beam current on accel-current/chamber-pressure relationship. (Hughes 30-cm-diam lab-model thruster)

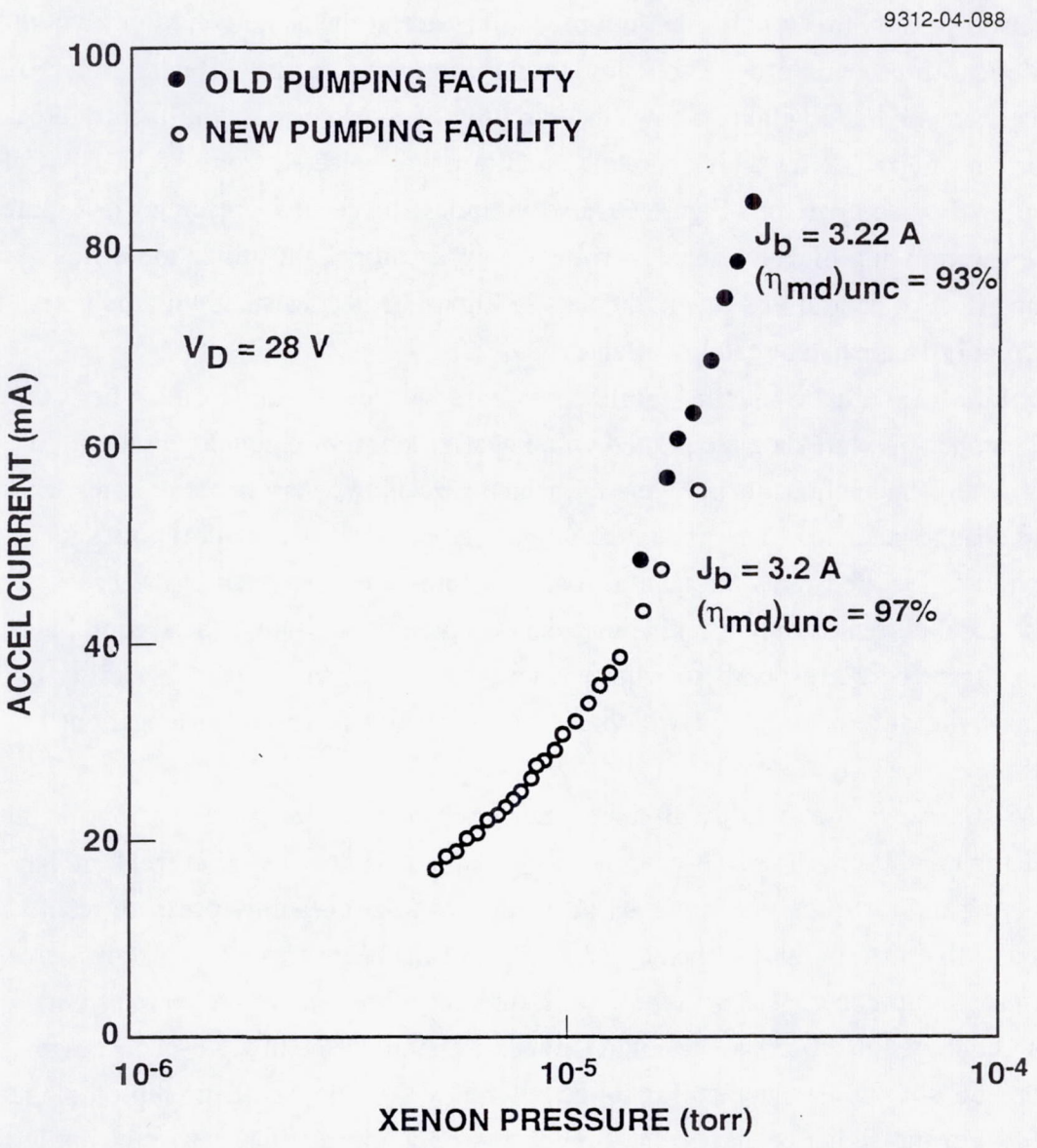

Figure 62. Dramatic redution in accel current achieved through modifications to improve the pumping speed of Hughes 9-ft-diam vacuum chamber.

We also operated the 30-cm-diam lab-model thruster at the same conditions as the NASA-LeRC life-test thruster, in order to obtain data for comparing facility effects in the NASA and Hughes test chambers. Figure 63 shows the variation of accel current with facility pressure at a beam current of $J_b = 3.2$ A. This operating condition was selected from the NASA-LeRC life-test results. For comparison, Figure 69 also includes the results presented in Figure 67 for thruster operation at a higher discharge voltage (higher propellant-utilization efficiency). The lack of an effect of neutral loss rate in the data of Figure 63 is consistent with the notion that the accel current is dominated by facility effects.

Additional insight into the facility-pressure effect is apparent when the accel-current/chamber-pressure data are plotted on a linear graph. For example, replotting the data of Figure 60 in this manner results in Figure 64, which reveals two very linear regimes separated by an abrupt change in slopes. The first linear regime (at low facility pressure) corresponds to what was previously referred to as the neutral-loss-rate-dominated behavior of the accel current, in which the accel current is only weakly dependent on facility pressure. The second linear regime shown in Figure 64 corresponds to what was previously referred to as the facility-dominated behavior of the accel current, in which the accel current is strongly dependent on facility pressure.

Figure 65 shows the same dual-slope linear behavior of the accel current with facility pressure for the 30-cm-diam lab-model thruster operated at a beam current of $J_b = 1.45$ A. Extrapolating the low-pressure segments of the curves to zero facility pressure results in accel currents of 3 to 4 mA, or approximately 0.2 to 0.3% of the beam current. This low percentage is consistent with our experience with the J-series mercury thruster, which operates with an accel-current fraction of about 0.2% at vacuum-chamber pressures in the low 10^{-6} Torr range.

Figure 66 shows the data of Figure 65, along with a linear-linear replot of data from Figure 61. For the higher beam current, the accel current appears linear over the entire range of facility pressure. There is no "break" in the curve, consistent with the notion that the accel current is facility dominated, even at the lowest facility pressure.

Insight into the behavior of the accel current with facility pressure evident in Figures 62 to 64 can be gained by reviewing the various contributions to the total accel current, J_A,

$$J_A = J_{th} + J_f, \tag{2}$$

where J_{th} is the accel current in the absence of facility pressure, and J_f is the accel current due to the facility pressure. The contribution J_{th} is from the neutral loss rate. For constant discharge

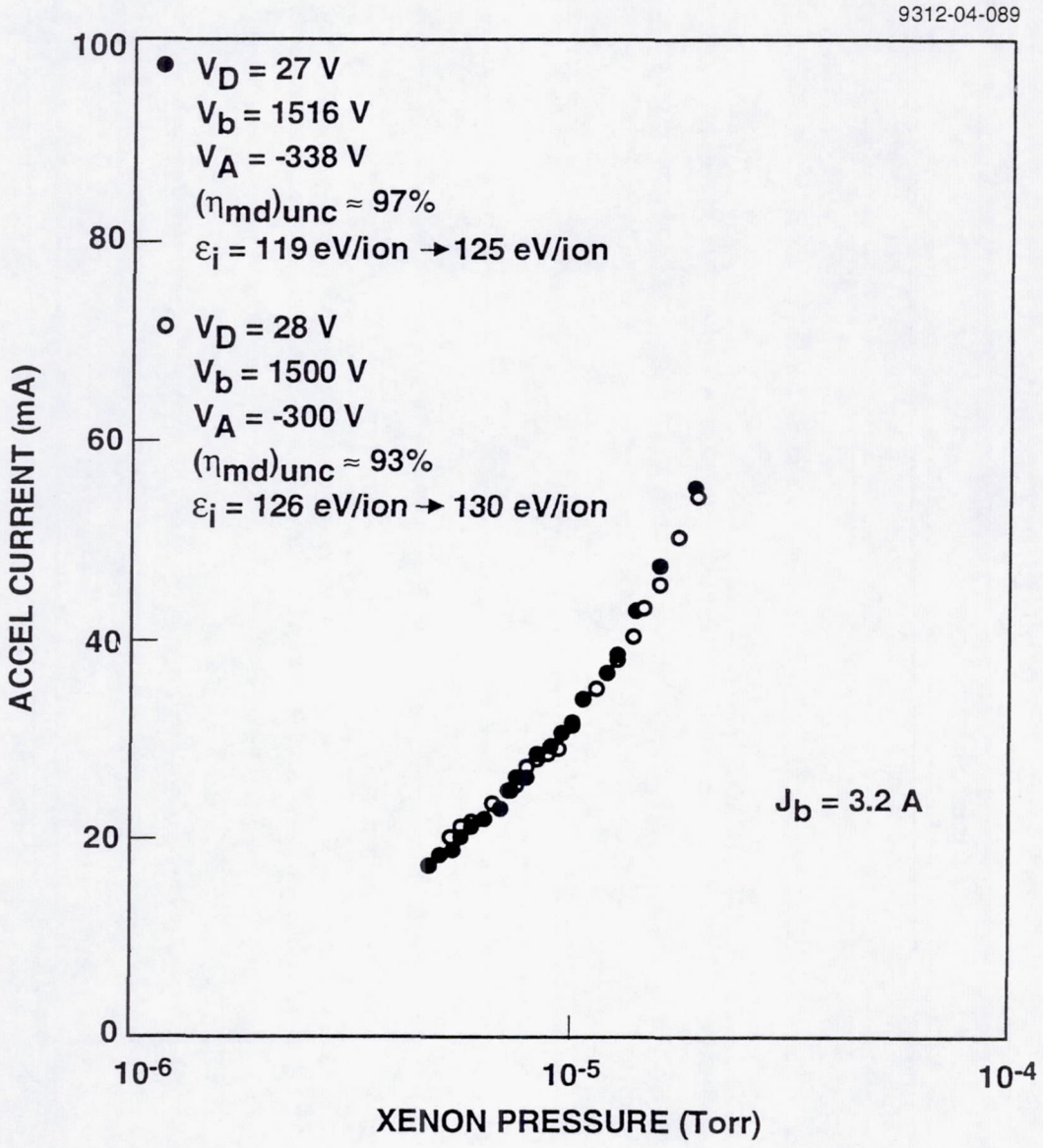

Figure 63. Effect of discharge voltage on accel-current/chamber-pressure relationship.

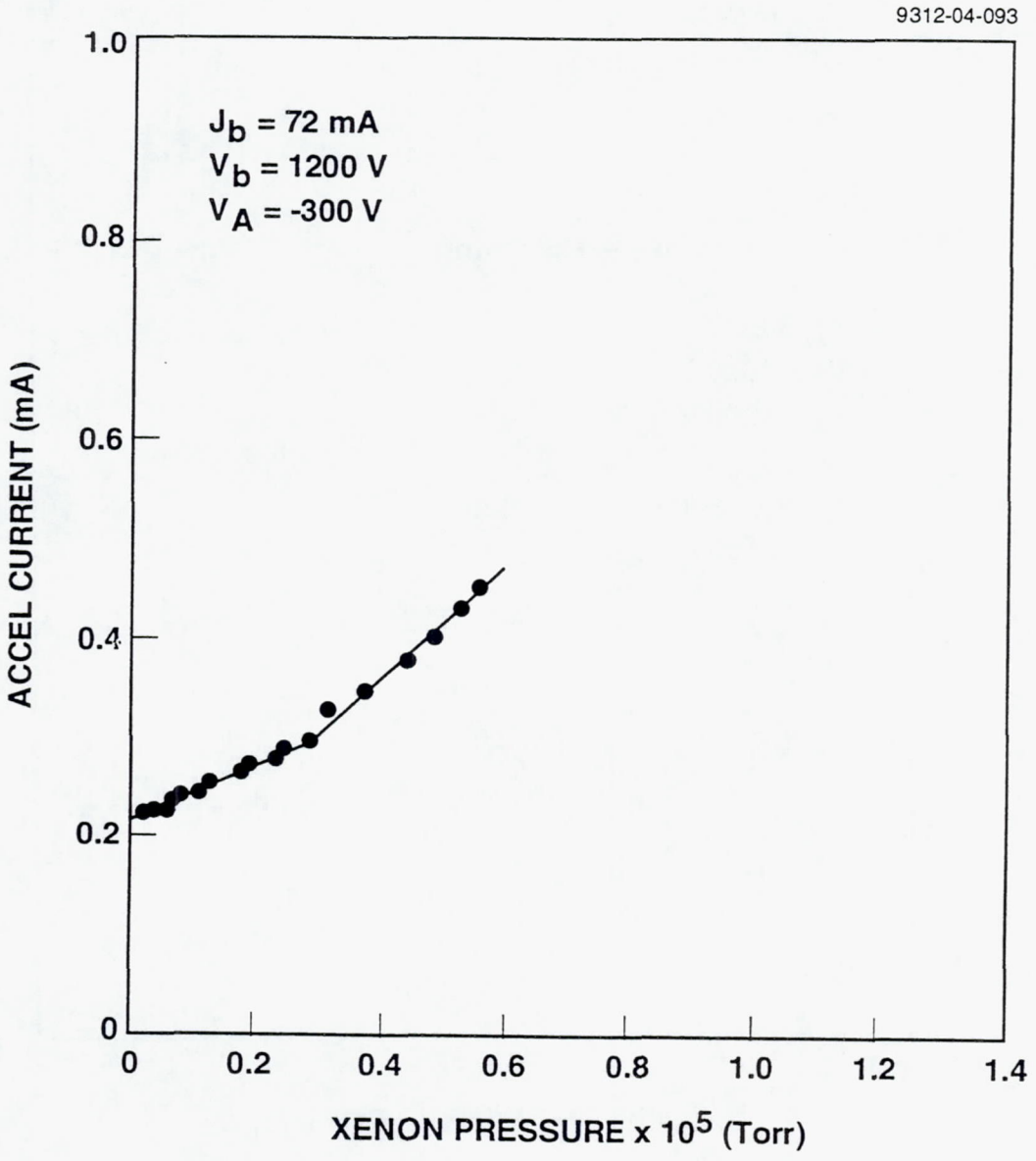

Figure 64. Effect of vacuum-chamber pressure on accel current (8-cm thruster S/N 907).

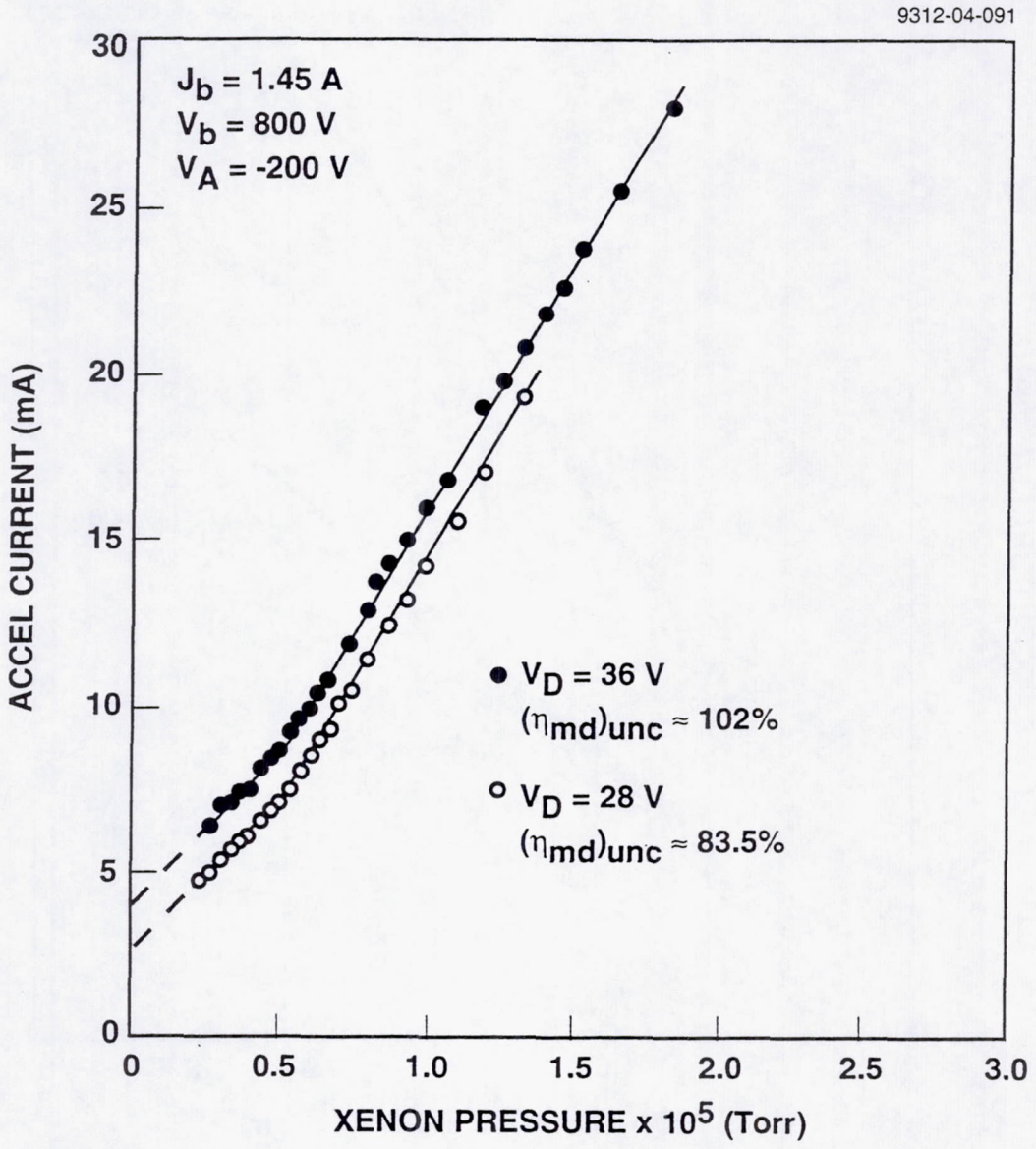

Figure 65. Effect of discharge voltage on accel-current/chamber-pressure relationship.

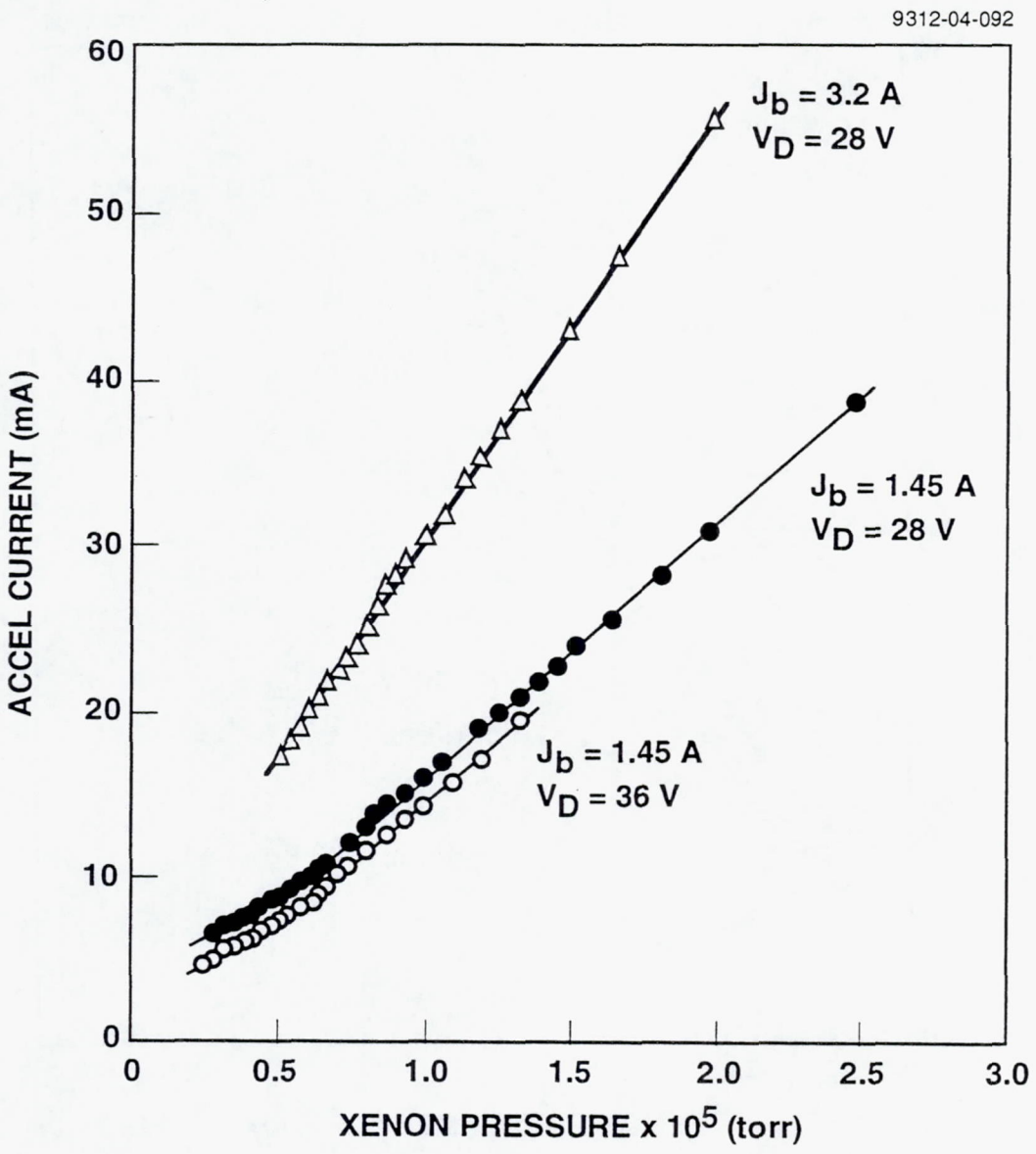

Figure 66. Effect of beam current on accel-current/chamber-pressure relationship.

propellant-utilization efficiency, the neutral loss rate is a constant, and, therefore, J_{th} is also a constant. The facility contribution to the accel current, J_f, is assumed to be independent of J_{th}, and to depend only on the density of gas in the facility, which is directly proportional to the facility pressure, p. Equation (2) can therefore be rewritten as,

$$J_A = A + Bp, \tag{3}$$

where A and B are constants. Equation (3) predicts a linear dependence of accel current on facility pressure. The intercept should be nearly equal to the space-environment accel current that would be realized in the absence of facility pressure.

The results presented in Figures 64 to 66 verify the linear dependence predicted by Equation (3), however they show a dual linear behavior that is not predicted. The accel-current intercept for the low-pressure data shown in Figure 65 is very close to the value expected on the basis of the accel current being approximately 0.2% of the beam current in the absence of a facility effect. This is consistent with what has been recorded for J-series thrusters operating on mercury propellant, where the facility effect is minimal. The encouraging aspect of the characteristics shown in Figure 66 is that the highly linear nature of the results would permit a confident extrapolation of the accel current to the limit of zero facility pressure, as long as the facility pressure is low enough to establish the "break" in the characteristic.

Figure 67 shows the variation of the accel current with chamber pressure for the 8-cm-diam IAPS thruster operated on xenon. We documented the behavior of the beam-plasma potential of the 8-cm-diam thruster for two extreme chamber-pressure conditions (1.4×10^{-7} Torr and 4×10^{-6} Torr). As can be seen from the data presented in Figure 67, the low-pressure value minimizes the facility contribution to the accel current, while the high-pressure value maximizes the facility effect on accel current.

6.3 BEAM-POTENTIAL MEASUREMENTS

We measured the probe floating profile by sweeping a hot-filament probe through the beam in the manner described in the final report[2] for Phase 1. Figure 68 shows a schematic of the filament-probe assembly. To determine the filament current for performing the plasma-potential measurements, we measured the variation of beam potential with filament current with the probe positioned at the beam centerline and outside the beam edge. Figure 69 compares the variation of the beam potential with filament current (filament temperature) when the probe is in and out of the beam. The data indicate that a filament current of 4.3 A is sufficient to achieve operation in the plateau region of the probe characteristic for both locations of the probe. The hot filament probes when located in the neutralized beam should float new plasma potential.

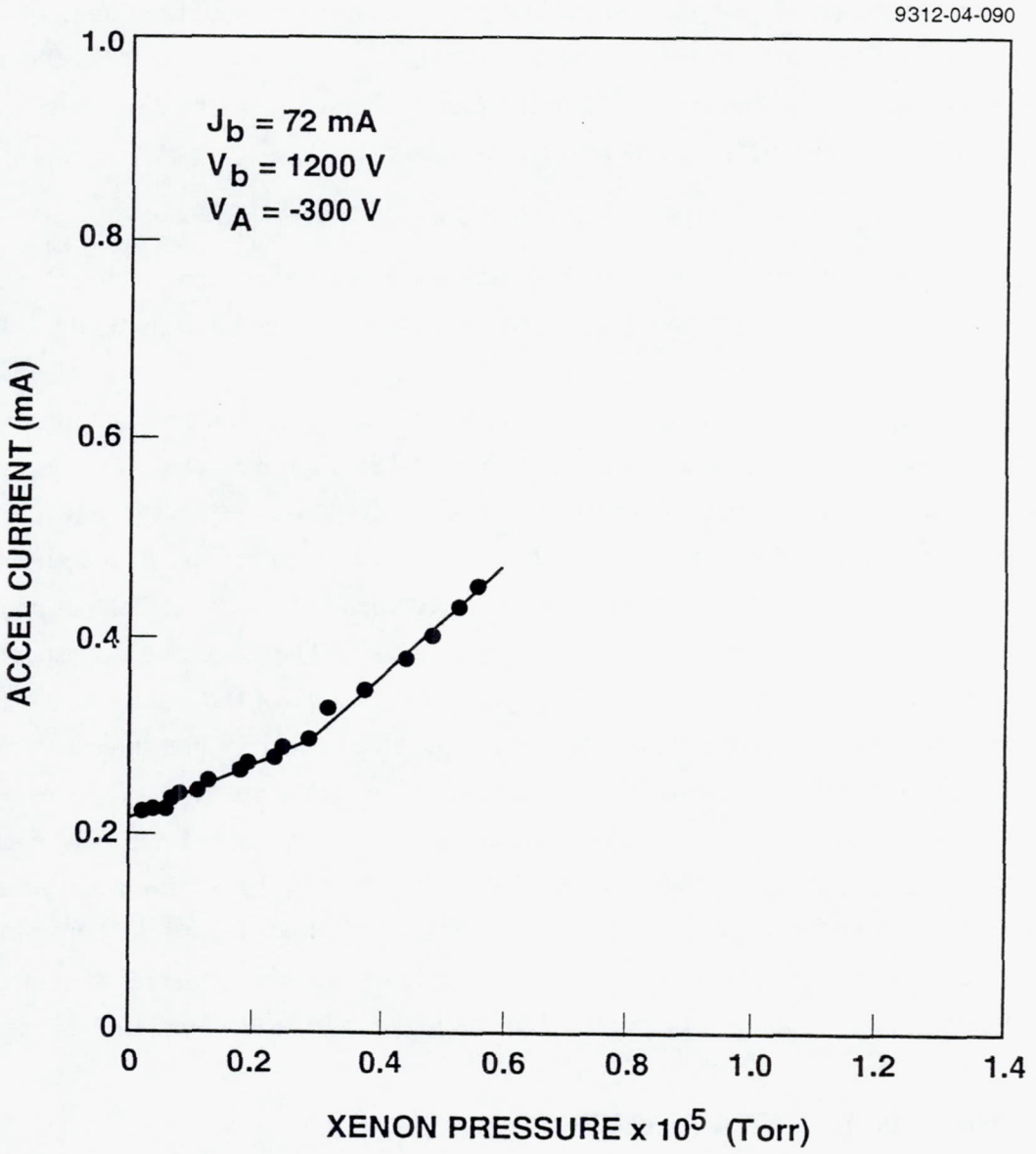

Figure 67. Variation of accel-grid current with vacuum-chamber pressure (8-cm thruster S/N 907).

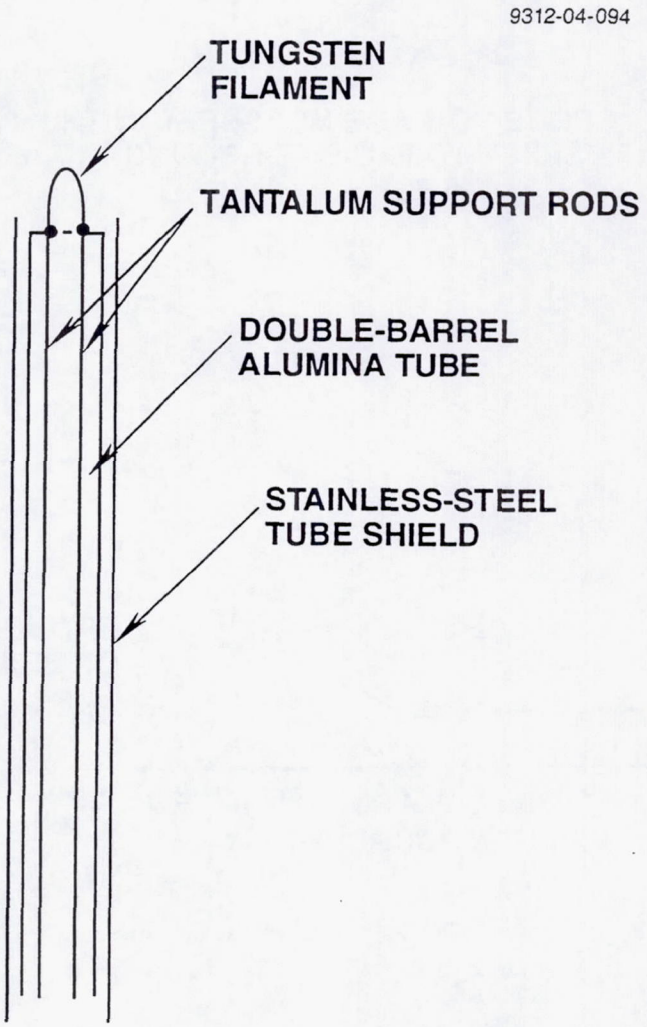

Figure 68. Sketch showing filament-type beam probe.

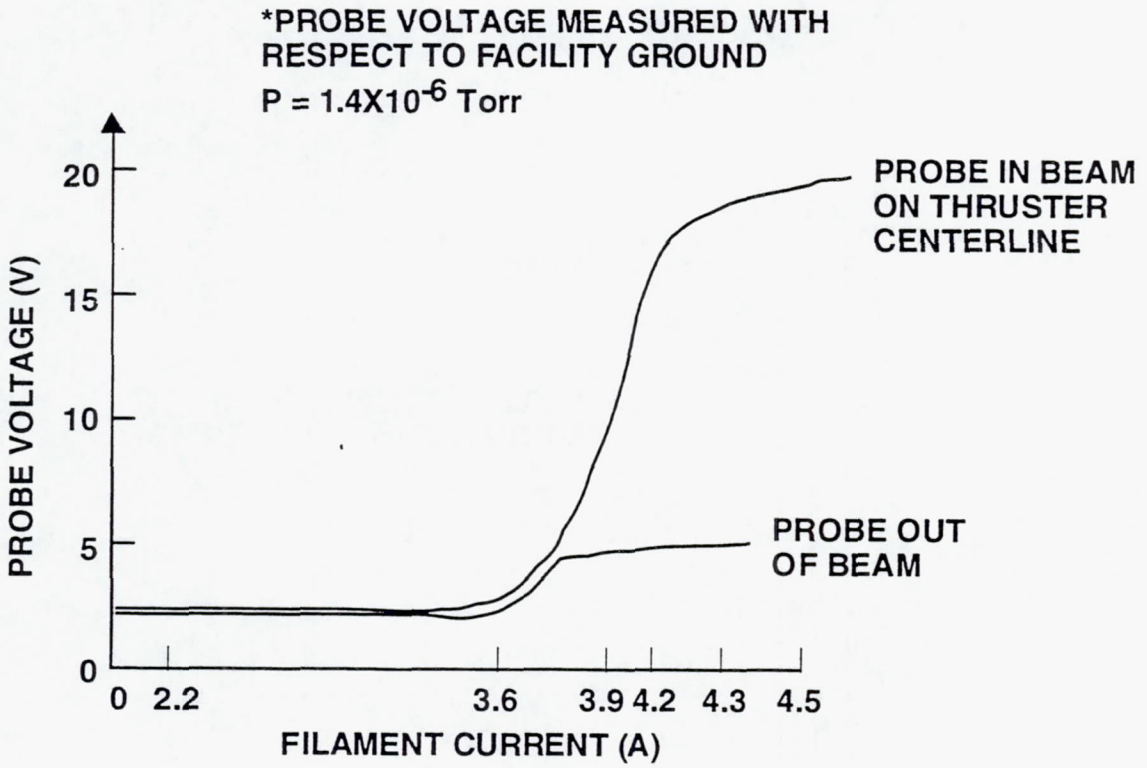

Figure 69. Emissive-probe floating potential.

With a filament current of 4.3 A, the beam-potential profile was measured at extreme values of vacuum-chamber pressure; 1.4×10^{-7} and 4×10^{-6} Torr. Figure 70 shows that as the pressure is increased, the beam potential is reduced and the profile becomes flatter (the offset of the two data scans is due to a zero shift in the x-y recorder). This behavior is the same as that which we documented[2] for the 30-cm-diam lab-model thruster operated at increasing chamber pressures.

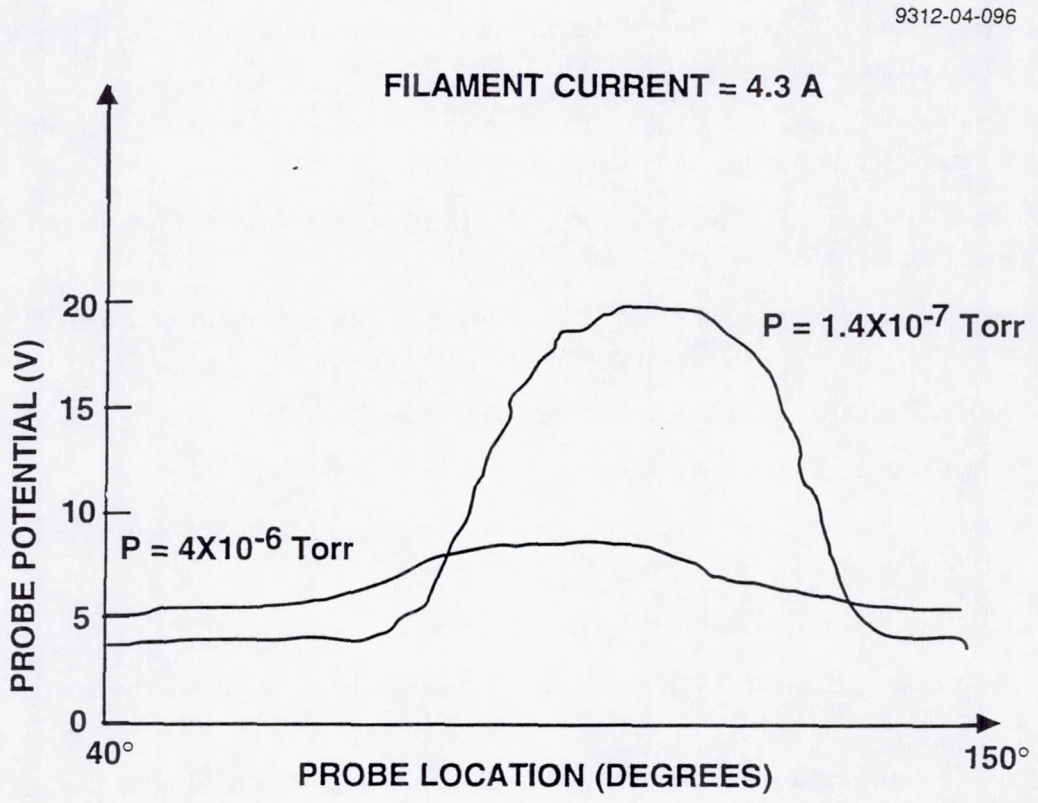

Figure 70. Effect of vacuum-chamber pressure on probe floating potential variation.

Section 7
REFERENCES

1. J.R. Beattie and J.N. Matossian, "Mercury ion thruster technology," Final Report, Hughes Research Laboratories, NASA CR-174974, Mar 1989.

2. J.R. Beattie and J.N. Matossian, "High power ion thruster technology," Final Report, Hughes Research Laboratories, NASA CR-187161, Feb 1992.

3. M.S. Patterson and T.R. Garver-Verbey, 21st International Electric Propulsion Conference, Orlando, Florida, AIAA Paper 90-658, July (1990).

4. B.A. Rock, M.A. Mantenieks, and M.L. Parsons, 18th International Electric Propulsion Conference AIAA Paper 85-2011, Alexandria, VA (1985).

5. J.M. Stone, Radiation and Optics (McGraw-Hill, New York, 1963).

6. A. Yariv, Quantum Electronics, 2nd ed. (Wiley, New York, 1975).

7. M. Kaminsky, Atomic and Ionic Impact Phenomena on Metal Surfaces (Academic, New York, 1965).

8. K.G. Whitney and J. Davis, J. Appl. Phys. 45, 5294 (1974).

9. Teledyne Hastings-Raydist, "Instruction manual for Hastings mass flowmeter," C194D, 1974.

10. Varian Vacuum Products Division, "Manual for Model 880RS digital ionization gauge controller," Appendix B, 1987. (From NASA Technical Note TND-5285).

11. J.M. Monheiser, "Development and Verification of a Model to Predict Impingdment Currents for Ion Thruster," NASA CR-195322, Colorado State University, April 1994.

Appendix A
FLOW METER CALIBRATION

A set of Hughes flow meters used for gas-thruster performance measurements was sent to NASA - LeRC for calibration with similar instruments used there. The Hughes flow meters were installed in a series arrangement in the LeRC common thruster propellant feed system. Figures A-1 thru A-3 present comparison of the main, cathode, and neutralizer flow-meter outputs, in units of sccm true xenon flow. Error bars are used to indicate the uncertainty in the Hughes flow rates, which are quoted as ±3% of full-scale output by our Primary Standards Laboratory. In general, the calibration data are well within the uncertainty in the Hughes data. We consider the calibrations to be in excellent agreement over the full range of main flow rate and over the normal range of cathode and neutralizer flow rates (i.e., ≤ 3 sccm).

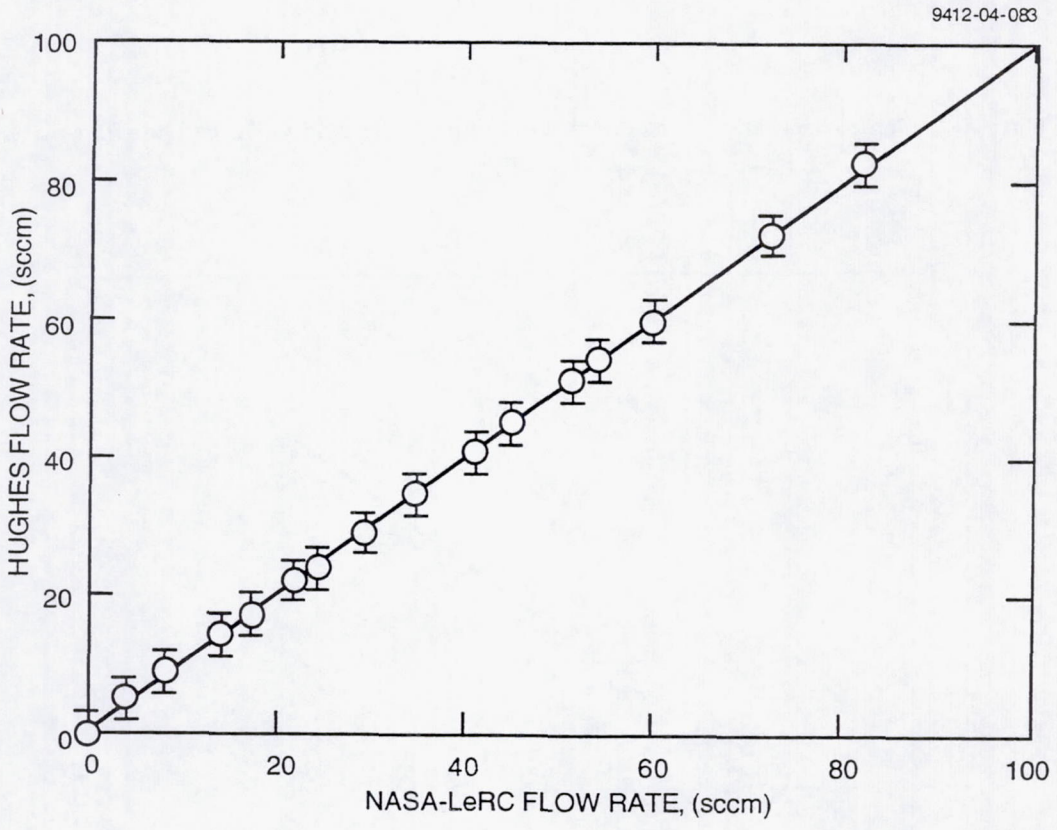

Figure A-1. Comparison of series calibration data for Hughes and LeRC main flow meters.

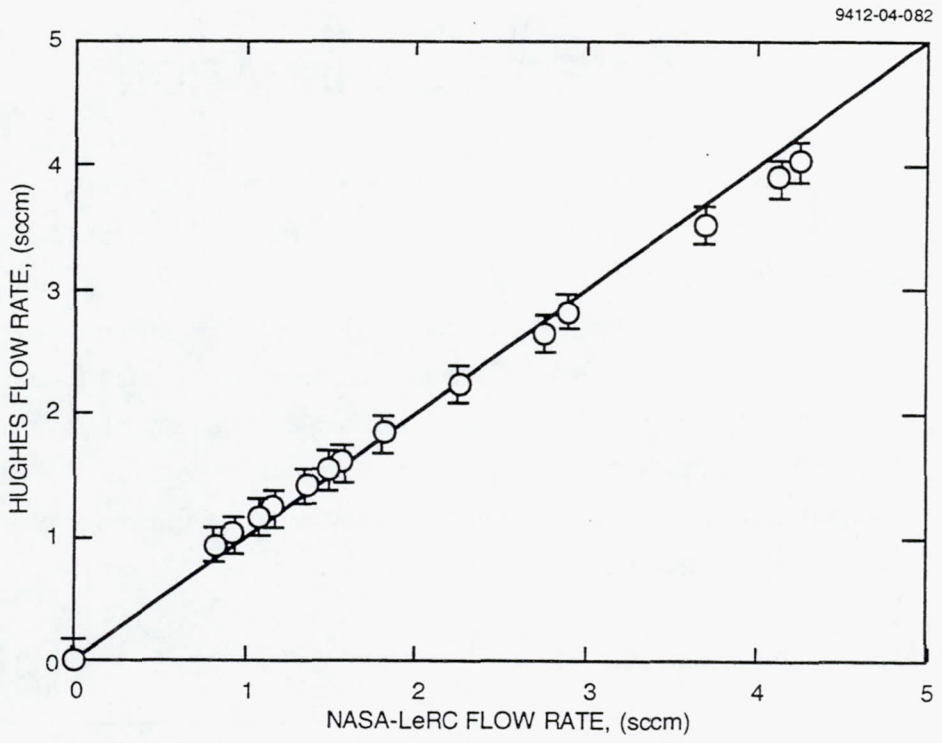

Figure A-2. Comparison of series calibration data for Hughes and LeRC cathode flow meters.

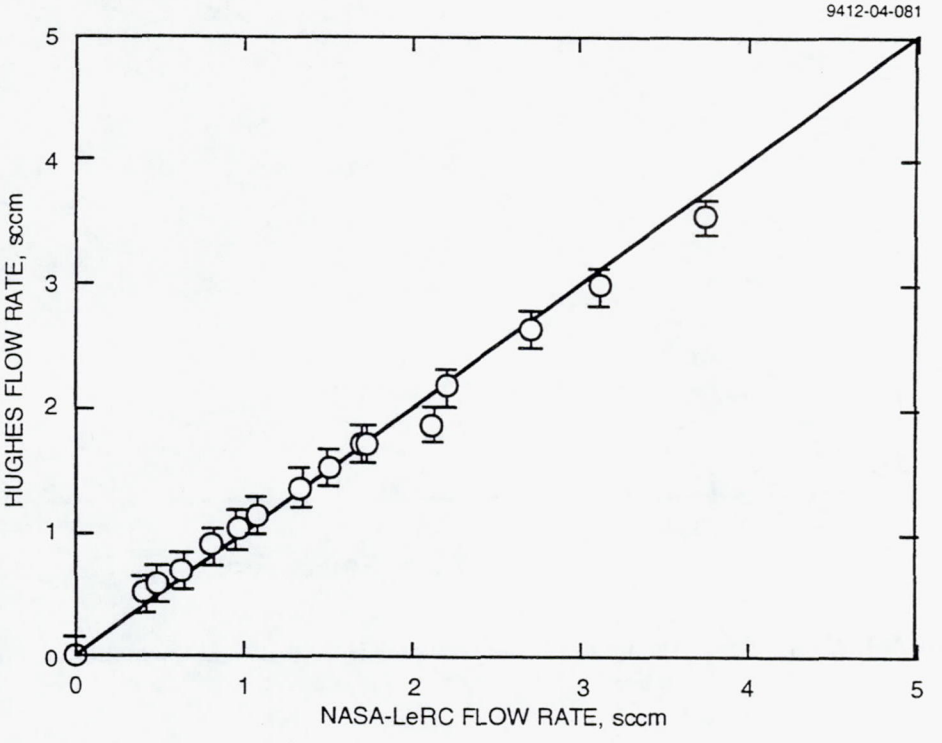

Figure A-3. Comparison of series calibration data for Hughes and LeRC neutralizer flow meters.

Appendix B
ION-OPTICS PERVEANCE DETERMINATION

In the final report[B-1] for Phase 1 of this contract, we described the use of an x-y recorder to obtain fast, reliable data for selecting the ion-optics operating voltage. During Phase 2, we fabricated a sweep circuit that is now permanently installed in our thruster test console for routinely obtaining this type of perveance data. A ramp generator is used to sweep the beam voltage over a selected range, while the accel voltage is maintained constant. Figure B-1 shows the quality of the data that can be obtained with our setup. Three scans are shown to demonstrate the high degree of reproducibility that is realized using the x-y recorder technique.

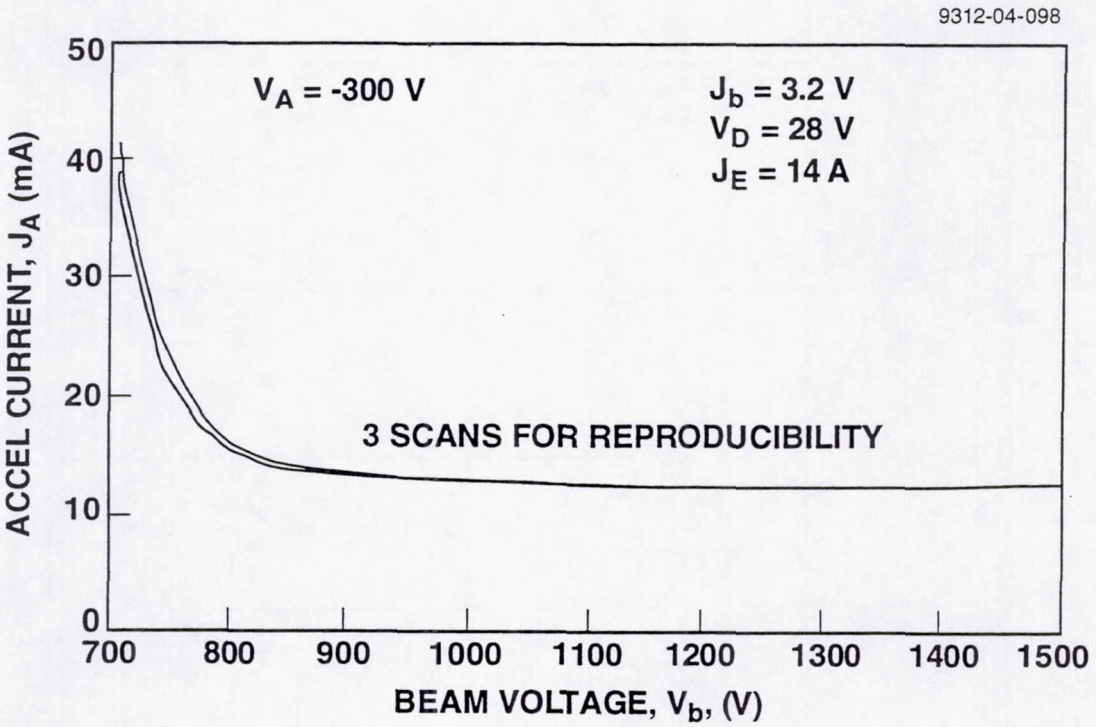

Figure B-1. x-y recorder traces (3 total) of the variation of accel current with beam voltage.

We also explored the use of op-amp circuitry to differentiate characteristics like the ones shown in Figure B-1 as a possible means of identifying an unambiguous "knee" in the curve. However, after examining the first and second derivatives of typical accel-current/beam-voltage characteristics, it appears that the "knee" may be best identified by specifying a tangency condition on the I/V characteristic (a technique suggested by V.K. Rawlin of NASA - LeRC).

For example, Figure B-2 shows tangents drawn to a typical characteristic having slopes of -0.067, -0.1, and -0.133 mA/V (-30, -45, and -60°, respectively for these scales). Although the selection of the "best" slope to define the knee is arbitrary, the results of Table B-1 show that the location of the knee is not too sensitive to the value of the slope used to define it. Therefore, we adopted a value of -0.1 mA/V as the slope of the tangent to be used in defining the knee of the curve. It appears that a conservative specification of the minimum operating voltage can then be achieved by adding 200 V to the knee value.

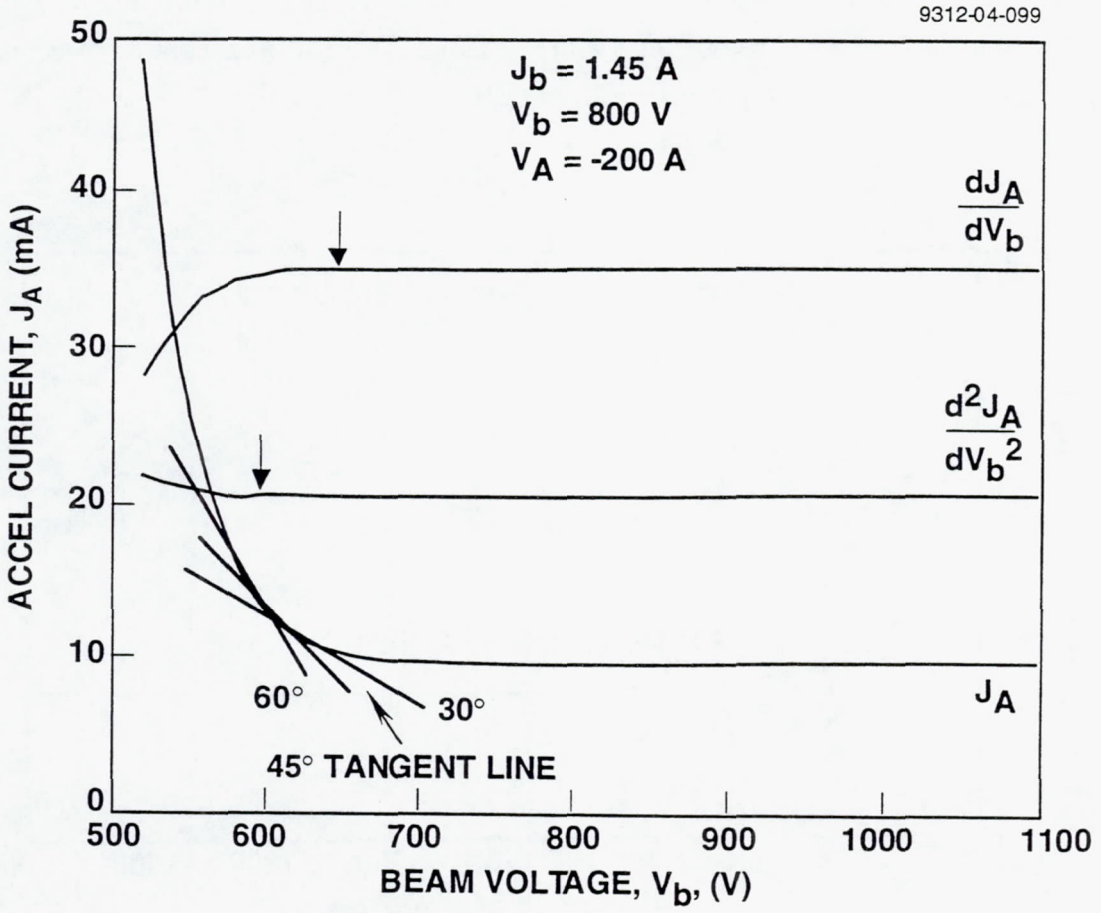

Figure B-2. Tangents used to define "knee" condition.

Table B-1. Beam Voltage Obtained from Knee of Curves in Figure 10.

Slope (mA/V)	Voltage (V)
-0.067	625
-0.100	610
-0.133	595

Appendix C
DOUBLY CHARGED ION FRACTION

Table C-1 is a sample output of **ExB** probe results for a beam current of J_b = 3.22 A. The "input data" show the measured singly and doubly charged ion currents J^+ and J^{++} obtained while viewing each of four radial locations on the ion optics from eight different angles. The "summary of thrust parameters" shows the singly and doubly charged ion-current densities j^+ and j^{++} and the ratio, j^{++}/j^+, obtained by integrating over the angular data[C-1]. Integrating these data over the full beam radius provides the ratio of doubly to singly charged ion current, J^{++}/J^+. The thrust-correction factor, γ, is the product of two thrust-loss parameters; F_t, which account for off-axis beamlet vectoring, and α, which accounts for the presence of doubly charged ions. The integrated beam current $J^+ + J^{++}$, shown in the "summary of thrust parameters" is in excellent agreement with the measured beam current of J_b = 3.22 A.

Table C-1. Sample Input/Output Data from ExB Probe

Input Data								
ϕ_p (deg)	r = 0.75 R		r = 0.50 R		r = 0.25 R		r = 0.00 R	
	J^+(nA)	J^{++} (nA)	J^+ (nA)	J^{++}(nA)	J^+(nA)	J^{++}(nA)	J^+(nA)	J^{++}(nA)
–25.0000	0.0030	0.0000	0.0020	0.0000	0.0000	0.0000	0.0000	0.0000
–20.0000	0.0100	0.0010	0.0060	0.0010	0.0030	0.0010	0.0000	0.0000
–15.0000	0.0700	0.0030	0.0440	0.0040	0.0140	0.0030	0.0030	0.0010
–10.0000	0.1600	0.0080	0.1000	0.0210	0.0650	0.0120	0.0340	0.0060
–5.0000	0.0560	0.0030	0.1480	0.0180	0.2080	0.0430	0.1300	0.0330
0.0000	0.0100	0.0010	0.0260	0.0020	0.1110	0.0220	0.1810	0.0450
5.0000	0.0030	0.0000	0.0040	0.0010	0.0230	0.0030	0.0500	0.0110
10.0000	0.0010	0.0000	0.0020	0.0000	0.0030	0.0010	0.0040	0.0010

Summary of Thrust Parameters				
	r= 0.75 R	r = 0.50 R	r = 0.25 R	r = 0.00 R
j^+ (mA/cm^2)	5.2733	5.2690	5.6859	5.8052
j^{++} (ma/cm^2)	0.3101	0.7036	1.1875	1.3948
(j^{++}/j^+)	0.0588	0.1335	0.2089	0.2403
ϕ(deg)	13.1237	11.6387	8.4060	7.0876
Alpha	F_t	$(J^+) + (J^{++})$	Beta	J^{++} / J^+
0.97221	0.97844	3.19156	0.95256	0.10481

Tables C-2 and C-3 summarize the performance of the Hughes 25- and 30-cm diam XIPS thrusters corresponding to operation at the "knee" of their performance curves. The performance data have been corrected using the results of **ExB**-probe measurements. (The last entry in Table C-2 corresponds to non-steady-state operation of the 25-cm-diam thruster; the remainder of the data in Tables C-2 and C-3 correspond to steady-state operation.)

Table C-2. 25-cm-diam XIPS Thruster Performance

J_b (A)	ε_i (W/A)	P_D (W)	P_b (kW)	P_T (kW)	γ^2	η_e (%)	F (mN)	Isp (s)	η_{md} (%)	η_{mt} (%)	η_t (%)
1.45	120	173	1.6	1.8	.94	86.7	77	3188	85.2	80.7	66
3.22	124	398	4.7	5.3	.91	89.8	195	4224	98.2	93.2	76
4.0	120	477	6.2	6.8	.89	90.3	245	4338	99.5	94.6	76
*5.0	126	606	8.2	9.1	.89	90.5	316	4795	105.8	101.3	82

*Extrapolated from 1.45, 3.22, and 4.0 beam-current data for δ excessive equilibrium temperature at J_b=5 A did not permit ExB measrement.

Table C-3. 30-cm-diam XIPS Thruster Performance

J_b (A)	ε_i (W/A)	P_D (W)	P_b (kW)	P_T (kW)	γ^2	η_e (%)	F (mN)	Isp (s)	η_{md} (%)	η_{mt} (%)	η_t (%)
1.45	121	125	1.2	1.4	.97	83	66	2330	78	69	55
3.22	120	386	3.5	4.0	.90	87	158	3226	93	88	69
3.22	120	387	4.7	5.1	.91	91	193	4200	97	94	77
4.0	120	480	5.0	5.6	.89	88	208	3676	98	94	74
5.0	125	626	9.0	9.8	.89	92	330	5025	104	102	83
*5.6	140	785	10.0	11.1	.87	90	364	5160	108	106	83

*No ExB data were measured because of overheating of ExB probe at the high form level. The d is extrapolated for plasma currents.

Figure C-1 shows the variation of integrated doubly to singly charged ion-current ratio J^+/J^{++} with discharge propellant-utilization efficiency. As anticipated, there is an increase in the doubly charged ion fraction with discharge propellant-utilization efficiency. At 90% efficiency, approximately 9% of the beam current is doubly charged. Figure C-2 shows the centerline value of the doubly to singly charged ion-current density ratio j^{++}/j^+ for the 30-cm-diam thruster. At a discharge-propellant-utilization of 90%, the doubly charged current fraction on centerline is about 25%.

J_b = 1.45 A 25-cm

Input Data								
ϕ_p (deg)	r = 0.75 R		r = 0.50 R		r = 0.25 R		r = 0.00 R	
	J^+(nA)	J^{++} (nA)	J^+ (nA)	J^{++}(nA)	J^+(nA)	J^{++}(nA)	J^+(nA)	J^{++}(nA)
–20.0000	0.0300	0.0000	0.0100	0.0000	0.0100	0.0000	0.0100	0.0000
–15.0000	0.0200	0.0100	0.0200	0.0000	0.0100	0.0000	0.0100	0.0000
–10.0000	0.0300	0.0150	0.2100	0.0200	0.0400	0.0000	0.0150	0.0000
–5.0000	0.3100	0.0150	0.3800	0.0350	0.2600	0.0300	0.0800	0.0100
0.0000	0.2100	0.0100	0.3500	0.0300	0.4000	0.0450	0.3000	0.0300
5.0000	0.0300	0.0000	0.2000	0.0150	0.3400	0.0300	0.4100	0.0450
10.0000	0.0150	0.0000	0.0200	0.0000	0.1700	0.0150	0.3200	0.0350

Summary of Thrust Parameters				
	r= 0.75 R	r = 0.50 R	r = 0.25 R	r = 0.00 R
j^+ (mA/cm^2)	2.4074	2.3630	2.3490	3.6813
j^{++} (ma/cm^2)	0.1120	0.1918	0.2309	0.2941
(j^{++}/j^+)	0.0465	0.0812	0.0983	0.0799
ϕ(deg)	10.8694	7.2152	7.4412	14.6030

Alpha	F_t	(J^+) + (J^{++}) Amps	Beta	J^{++} / J^+
0.98254	0.98595	1.19768	0.97019	0.06340

J_b = 3.22 A 25-cm

Input Data								
ϕ_p (deg)	r = 0.75 R		r = 0.50 R		r = 0.25 R		r = 0.00 R	
	J^+(nA)	J^{++} (nA)	J^+ (nA)	J^{++}(nA)	J^+(nA)	J^{++}(nA)	J^+(nA)	J^{++}(nA)
–20.0000	0.0000	0.0000	0.0000	0.0000	0.0000	0.0000	0.0000	0.0000
–15.0000	0.0400	0.0050	0.0150	0.0000	0.0000	0.0000	0.0000	0.0000
–10.0000	0.0700	0.0150	0.0650	0.0100	0.0150	0.0000	0.0050	0.0000
–5.0000	0.0600	0.0050	0.1200	0.0200	0.0700	0.0200	0.0350	0.0100
0.0000	0.0250	0.0000	0.0600	0.0100	0.1150	0.0300	0.1000	0.0300
5.0000	0.0050	0.0000	0.0400	0.0000	0.0800	0.0200	0.1200	0.0300
10.0000	0.0050	0.0000	0.0400	0.0000	0.0800	0.0200	0.1200	0.0300
15.0000	0.0000	0.0000	0.0000	0.0000	0.0300	0.0100	0.0650	0.0200

Summary of Thrust Parameters				
	r= 0.75 R	r = 0.50 R	r = 0.25 R	r = 0.00 R
j^+ (mA/cm^2)	4.7947	9.2098	10.0144	10.3419
j^{++} (ma/cm^2)	0.2776	0.5244	2.6413	3.1029
(j^{++}/j^+)	0.0579	0.0569	0.2637	0.3000
ϕ(deg)	9.8952	9.0810	9.8584	8.5191

Alpha	F_t	(J^+) + (J^{++}) Amps	Beta	J^{++} / J^+
0.96902	0.98595	3.53249	0.94712	0.11827

J_b = 4.0 A 25-cm

Input Data								
ϕ_p (deg)	r = 0.75 R		r = 0.50 R		r = 0.25 R		r = 0.00 R	
	J^+(nA)	J^{++} (nA)	J^+ (nA)	J^{++}(nA)	J^+(nA)	J^{++}(nA)	J^+(nA)	J^{++}(nA)
–20.0000	0.0050	0.0000	0.0020	0.0000	0.0000	0.0000	0.0000	0.0000
–15.0000	0.0400	0.0050	0.0150	0.0020	0.0000	0.0000	0.0000	0.0000
–10.0000	0.0800	0.0100	0.0800	0.0150	0.0220	0.0050	0.0050	0.0000
–5.0000	0.1000	0.0100	0.1400	0.0300	0.0600	0.0200	0.0200	0.0050
0.0000	0.0500	0.0050	0.1000	0.0200	0.1500	0.0500	0.0800	0.0300
5.0000	0.0100	0.0000	0.0600	0.0100	0.1200	0.0400	0.1600	0.0600
10.0000	0.0000	0.0000	0.0150	0.0000	0.0500	0.0200	0.1200	0.0400

Summary of Thrust Parameters				
	r= 0.75 R	r = 0.50 R	r = 0.25 R	r = 0.00 R
j^+ (mA/cm^2)	5.7565	8.7030	7.4761	7.9468
j^{++} (ma/cm^2)	0.5960	1.4718	2.5646	2.2742
(j^{++}/j^+)	0.1035	0.1691	0.3430	0.2862
ϕ(deg)	10.6784	7.5573	7.7786	8.2015

Alpha	F_t	(J^+) + (J^{++}) Amps	Beta	J^{++} / J^+
0.95671	0.98690	3.69919	0.92609	0.17345

J_b = 1.45A 30-cm

Input Data								
ϕ_p (deg)	r = 0.75 R		r = 0.50 R		r = 0.25 R		r = 0.00 R	
	J^+(nA)	J^{++} (nA)	J^+ (nA)	J^{++}(nA)	J^+(nA)	J^{++}(nA)	J^+(nA)	J^{++}(nA)
–20.0000	0.0120	0.0000	0.0000	0.0000	0.0000	0.0000	0.0000	0.0000
–15.0000	0.1150	0.0000	0.0820	0.0030	0.0080	0.0000	0.0000	0.0000
–10.0000	0.3330	0.0150	0.4330	0.0180	0.0830	0.0070	0.0370	0.0000
–5.0000	0.1170	0.0010	0.4060	0.0110	0.6390	0.0200	0.2680	0.0210
0.0000	0.0150	0.0000	0.0550	0.0000	0.4000	0.0130	0.7380	0.0380
5.0000	0.0000	0.0000	0.0020	0.0000	0.0520	0.0000	0.1460	0.0020
10.0000	0.0000	0.0000	0.0000	0.0000	0.0020	0.0000	0.0290	0.0000

Summary of Thrust Parameters				
	r= 0.75 R	r = 0.50 R	r = 0.25 R	r = 0.00 R
j^+ (mA/cm^2)	0.7269	1.2799	1.4110	1.4202
j^{++} (ma/cm^2)	0.0002	0.0383	0.0497	0.0687
(j^{++}/j^+)	0.0003	0.0299	0.0352	0.0483
ϕ(deg)	9.8739	8.7740	4.9447	5.8880

Alpha	F_t	(J^+) + (J^{++}) Amps	Beta	J^{++} / J^+
0.99481	0.98923	0.53419	0.99114	0.01804

J_b = 3.22A 30-cm
V_b = 3.5 kW

Input Data								
ϕ_p (deg)	r = 0.75 R		r = 0.50 R		r = 0.25 R		r = 0.00 R	
	J^+(nA)	J^{++} (nA)	J^+ (nA)	J^{++}(nA)	J^+(nA)	J^{++}(nA)	J^+(nA)	J^{++}(nA)
-20.0000	0.0150	0.0000	0.0000	0.0000	0.0000	0.0000	0.0000	0.0000
-15.0000	0.1000	0.0100	0.0500	0.0100	0.0200	0.0100	0.0100	0.0000
-10.0000	0.1500	0.0100	0.1800	0.0200	0.0700	0.0200	0.0400	0.0100
-5.0000	0.0550	0.0050	0.1400	0.0150	0.2100	0.0450	0.1400	0.0400
0.0000	0.0150	0.0000	0.0400	0.0000	0.1200	0.0250	0.2000	0.0500
5.0000	0.0000	0.0000	0.0000	0.0000	0.0300	0.0100	0.0700	0.0200
10.0000	0.0000	0.0000	0.0000	0.0000	0.0000	0.0000	0.0000	0.0000

Summary of Thrust Parameters				
	r= 0.75 R	r = 0.50 R	r = 0.25 R	r = 0.00 R
j^+ (mA/cm^2)	5.7282	6.1425	7.5574	7.5202
j^{++} (ma/cm^2)	0.4479	0.6706	2.2572	1.7939
(j^{++}/j^+)	0.0782	0.1092	0.2987	0.2385
ϕ(deg)	11.0589	8.3818	9.0331	7.7935

Alpha	F_t	(J^+) + (J^{++}) Amps	Beta	J^{++} / J^+
0.96459	0.98461	3.78820	0.93956	0.13751

J_b = 3.22A 30-cm
P_b = 4.7 kW

Input Data								
ϕ_p (deg)	r = 0.75 R		r = 0.50 R		r = 0.25 R		r = 0.00 R	
	J^+(nA)	J^{++} (nA)	J^+ (nA)	J^{++}(nA)	J^+(nA)	J^{++}(nA)	J^+(nA)	J^{++}(nA)
-20.0000	0.0200	0.0000	0.0100	0.0000	0.0050	0.0000	0.0000	0.0000
-15.0000	0.0900	0.0100	0.0600	0.0100	0.0150	0.0000	0.0100	0.0000
-10.0000	0.1000	0.0100	0.1700	0.0300	0.0700	0.0200	0.0350	0.0100
-5.0000	0.0500	0.0000	0.1300	0.0200	0.2100	0.0650	0.1400	0.0450
0.0000	0.0100	0.0000	0.0300	0.0000	0.1200	0.0300	0.2300	0.0750
5.0000	0.0000	0.0000	0.0100	0.0000	0.0400	0.0100	0.0800	0.0200
10.0000	0.0000	0.0000	0.0000	0.0000	0.0100	0.0000	0.0200	0.0000

Summary of Thrust Parameters				
	r= 0.75 R	r = 0.50 R	r = 0.25 R	r = 0.00 R
j^+ (mA/cm^2)	4.9397	6.9753	8.4008	7.7274
j^{++} (ma/cm^2)	0.3069	0.7901	1.8123	1.9953
(j^{++}/j^+)	0.0621	0.1133	0.2157	0.2582
ϕ(deg)	12.0287	8.8134	8.4409	7.6397

Alpha	F_t	(J^+) + (J^{++}) Amps	Beta	J^{++} / J^+
0.96953	0.98363	3.63068	0.93956	0.11609

J_b = 4 A 30-cm

Input Data								
ϕ_p (deg)	r = 0.75 R		r = 0.50 R		r = 0.25 R		r = 0.00 R	
	J^+(nA)	J^{++} (nA)	J^+ (nA)	J^{++}(nA)	J^+(nA)	J^{++}(nA)	J^+(nA)	J^{++}(nA)
-20.0000	0.0150	0.0000	0.0100	0.0000	0.0100	0.0000	0.0000	0.0000
-15.0000	0.0800	0.0100	0.0500	0.0150	0.0250	0.0100	0.0000	0.0000
-10.0000	0.1900	0.0200	0.1900	0.0300	0.0800	0.0200	0.0400	0.0150
-5.0000	0.0600	0.0100	0.1500	0.0200	0.2300	0.0600	0.1400	0.0500
0.0000	0.0200	0.0000	0.0400	0.0100	0.1300	0.0300	0.2000	0.0700
5.0000	0.0100	0.0000	0.0100	0.0000	0.0400	0.0100	0.0700	0.0300
10.0000	0.0000	0.0000	0.0000	0.0000	0.0100	0.0000	0.0300	0.0100

Summary of Thrust Parameters				
	r= 0.75 R	r = 0.50 R	r = 0.25 R	r = 0.00 R
j^+ (mA/cm^2)	5.8558	7.2448	9.7576	6.6902
j^{++} (ma/cm^2)	0.5607	1.3340	2.5097	2.5755
(j^{++}/j^+)	0.0958	0.1841	0.2572	0.3850
ϕ(deg)	9.1080	8.4121	9.7763	6.3228

Alpha	F_t	(J^+) + (J^{++}) Amps	Beta	J^{++} / J^+
0.95978	0.98722	4.31250	0.93134	0.15917

J_b = 5 A 30-cm

Input Data								
ϕ_p (deg)	r = 0.75 R		r = 0.50 R		r = 0.25 R		r = 0.00 R	
	J^+(nA)	J^{++} (nA)	J^+ (nA)	J^{++}(nA)	J^+(nA)	J^{++}(nA)	J^+(nA)	J^{++}(nA)
-20.0000	0.0200	0.0000	0.0100	0.0000	0.0000	0.0000	0.0000	0.0000
-15.0000	0.1100	0.0100	0.0700	0.0150	0.0200	0.0100	0.0150	0.0100
-10.0000	0.1900	0.0200	0.2800	0.0550	0.0900	0.0300	0.0400	0.0150
-5.0000	0.0600	0.0100	0.2000	0.0350	0.3200	0.1300	0.1800	0.0800
0.0000	0.0200	0.0000	0.0500	0.0100	0.1800	0.0600	0.3100	0.1600
5.0000	0.0000	0.0000	0.0150	0.0000	0.0350	0.0100	0.0900	0.0300
10.0000	0.0000	0.0000	0.0000	0.0000	0.0100	0.0000	0.0200	0.0000

Summary of Thrust Parameters				
	r= 0.75 R	r = 0.50 R	r = 0.25 R	r = 0.00 R
j^+ (mA/cm^2)	6.5542	10.2004	10.0754	9.7242
j^{++} (ma/cm^2)	0.5645	1.6836	3.7818	4.4770
(j^{++}/j^+)	0.0861	0.1650	0.3753	0.4604
ϕ(deg)	10.6708	8.0840	8.7721	8.4473

Alpha	F_t	(J^+) + (J^{++}) Amps	Beta	J^{++} / J^+
0.95570	0.98613	5.06932	0.92437	0.17822

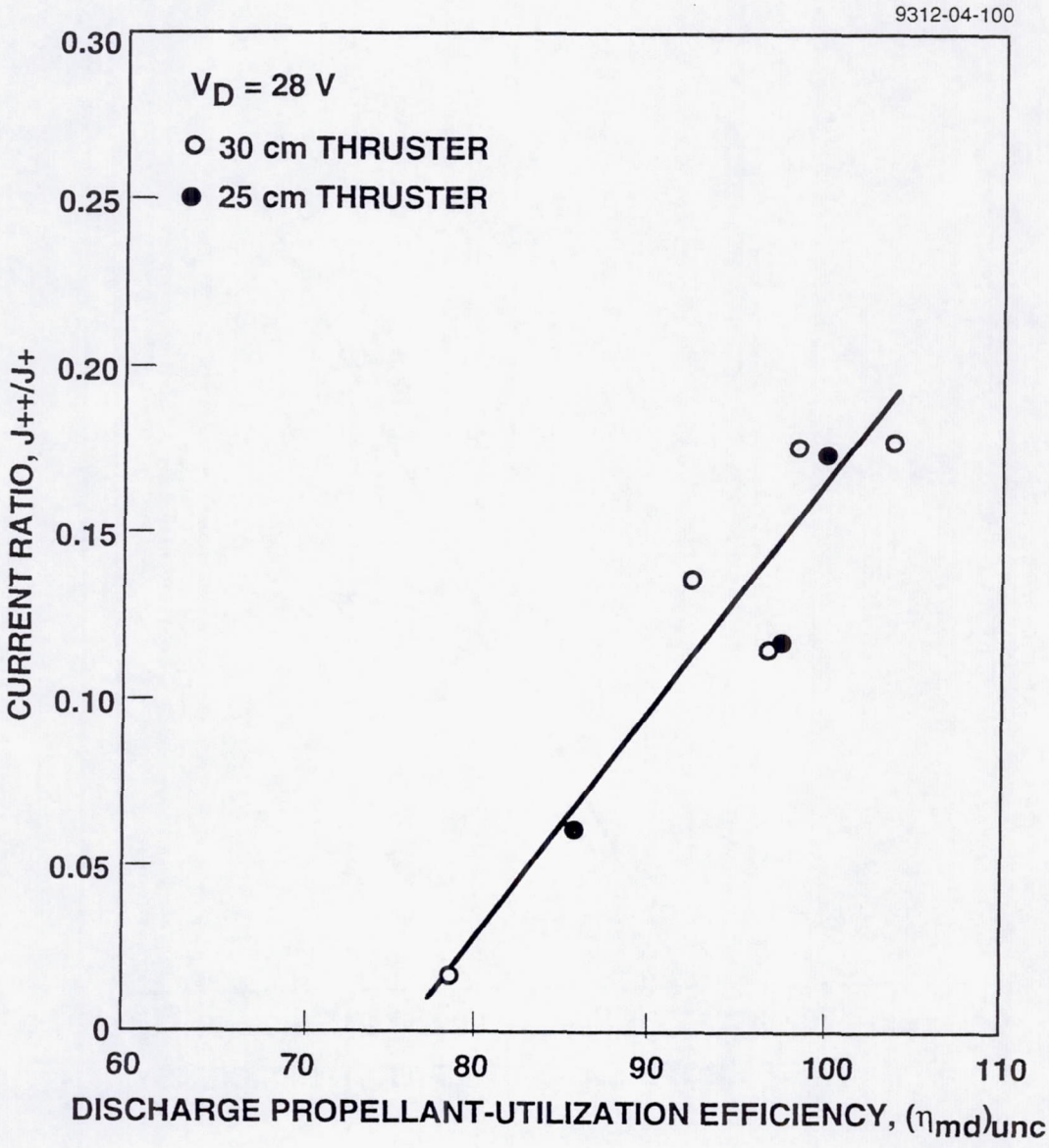

Figure C-1. Variation of doubly to singly charged ion-current ratio with measured discharge propellant-utilization efficiency.

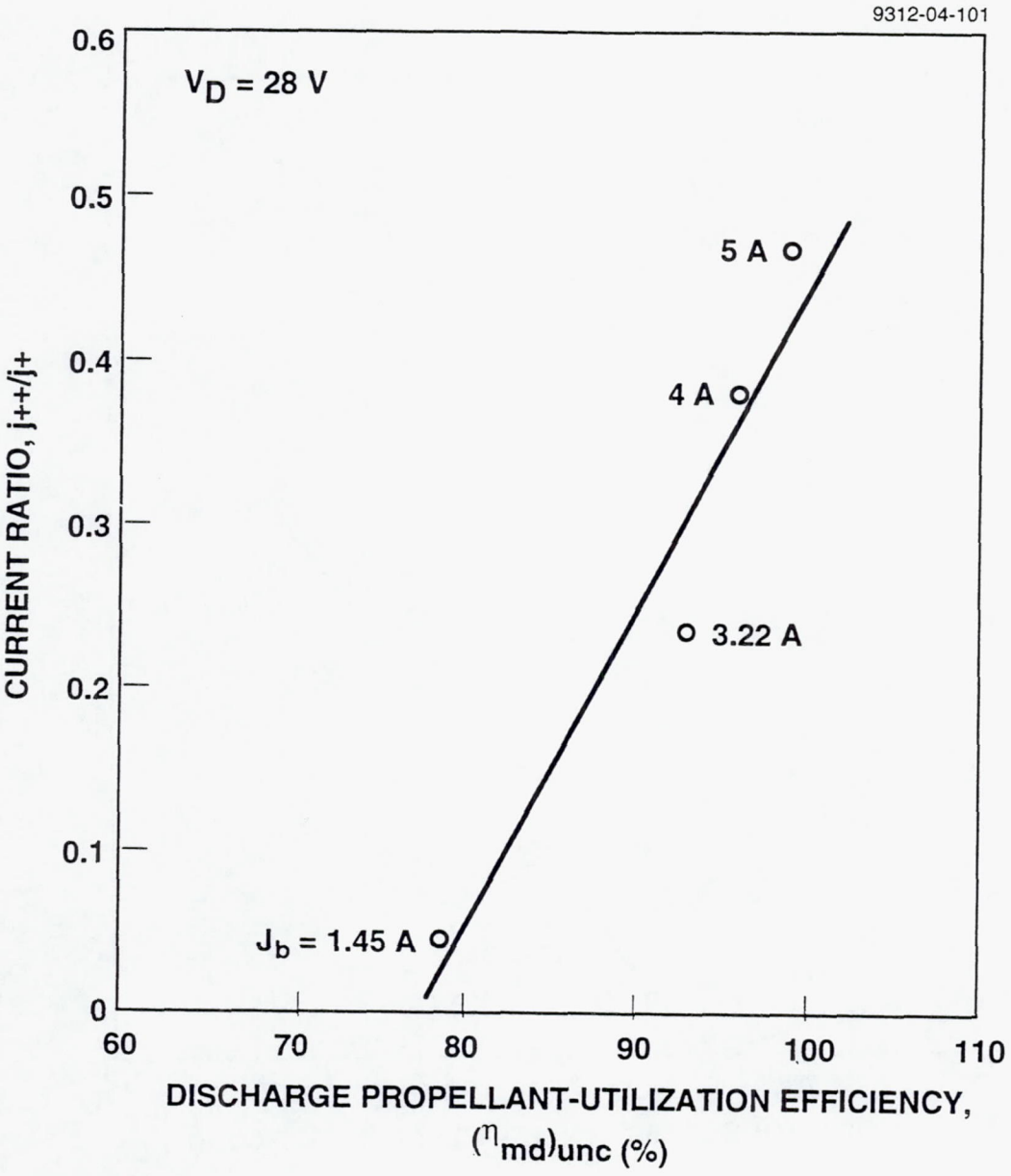

Figure C-2. Variation of doubly to singly charged ion-current density ratio with measured discharge propellant-utilization efficiency.

Appendix D
APPENDICES REFERENCES

B-1 J.R. Beattie and J.N. Matosian, *"High Power Ion Thruster Technology,"* Final Report, Hughes Research Laboratories, NASA CR-187161, Feb. 1992.

C-1 J.R. Beattie, *"Extended Performance Technology Study: 30-cm Thruster,"* Final Report, Hughes Research Laboratoies, NASA CR-168259, June 1983.

NASA
National Aeronautics and Space Administration

Report Documentation Page

1. Report No.	2. Government Accession No.	3. Recipient's Catalog No.
NASA CR-195477		

4. Title and Subtitle	5. Report Date
High-Power Ion Thruster Technology	June 1996
	6. Performing Organization Code

7. Author(s)	8. Performing Organization Report No.
J.R. Beattie and J.N. Matossian	E-9693
	10. Work Unit No.

9. Performing Organization Name and Address	11. Contract or Grant No.
Hughes Research Laboratories 3011 Malibu Canyon Road Malibu, CA 90265	NAS3-25553
	13. Type of Report and Period Covered
12. Sponsoring Agency Name and Address	Final 10/20/89 – 10/20/92
Lewis Research Center 21000 Brookpark Road Cleveland, OH 44135	14. Sponsoring Agency Code

15. Supplementary Notes

Project Manager: James S. Sovey
NASA Lewis Research Center, Cleveland, OH 44135 (216) 977-7454

16. Abstract

Performance data are presented for the NASA/Hughes 30-cm-diam "common" thruster operated over the power range from 600 W to 4.6 kW. At the 4.6-kW power level, the thruster produces 172 mN of thrust at a specific impulse of just under 4000 s. Xenon pressure and temperature measurements are presented for a 6.4-mm-diam hollow cathode operated at emission currents ranging from 5 to 30 A and flow rates of 4 sccm and 8 sccm. Highly reproducible results show that the cathode temperature is a linear function of emission current, ranging from ≈1000°C to 1150°C over this same current range. Laser-induced fluorescence (LIF) measurements obtained from a 30-cm-diam thruster are presented, suggesting that LIF could be a valuable diagnostic for real-time assessment of accelerator-grid erosion. Calibration results of laminar-thin-film (LTF) erosion badges with bulk molybdenum are presented for 300-eV xenon, krypton, and argon sputtering ions. Facility-pressure effects on the charge-exchange ion current collected by 8-cm-diam and 30-cm-diam thrusters operated on xenon propellant are presented to show that accel current is nearly independent of facility pressure at low pressures, but increases rapidly under high-background-pressure conditions.

17. Key Words [Suggested by Author(s)]	18. Distribution Statement
Electric Propulsion Ion Propulsion Plasma Applications	

19. Security Classif. (of this report)	20. Security Classif. (of this page)	21. No. of pages	22. Price
Unclassified	Unclassified	108	

NASA FORM 1626 OCT 86